Metal-Assisted Electrochemical Nanoimprinting:

Delivering Resolution and Throughput via Engineered Stamps

by

Aliaksandr Sharstniou

A Dissertation Presented in Partial Fulfillment
of the Requirements for the Degree
Doctor of Philosophy

Approved November 2022 by the
Graduate Supervisory Committee:

Bruno Azeredo, Chair
Candace Chan
Konrad Rykaczewski
William Petuskey
Xiangfan Chen

ARIZONA STATE UNIVERSITY

December 2022

ABSTRACT

Recent advancements in the field of light wavefront engineering rely on complex 3D metasurfaces composed of sub-wavelength structures which, for the near infrared range, are challenging to manufacture using contemporary scalable micro- and nanomachining solutions. To address this demand, a novel parallel micromachining method, called metal-assisted electrochemical nanoimprinting (Mac-Imprint) was developed. Mac-Imprint relies on the catalysis of silicon wet etching by a gold-coated stamp enabled by mass-transport of the reactants to achieve high pattern transfer fidelity. This was realized by (i) using nanoporous catalysts to promote etching solution diffusion and (ii) semiconductor substrate pre-patterning with millimeter-scale pillars to provide etching solution storage. However, both of these approaches obstruct scaling of the process in terms of (i) surface roughness and resolution, and (ii) areal footprint of the fabricated structures. To address the first limitation, this dissertation explores fundamental mechanisms underlying the resolution limit of Mac-Imprint and correlates it to the Debye length (~0.9 nm). By synthesizing nanoporous catalytic stamps with pore size less than 10 nm, the sidewall roughness of Mac-Imprinted patterns is reduced to levels comparable to plasma-based micromachining. This improvement allows for the implementation of Mac-Imprint to fabricate Si rib waveguides with limited levels of light scattering on its sidewall. To address the second limitation, this dissertation focuses on the management of the etching solution storage by developing engineered stamps composed of highly porous polymers coated in gold. In a plate-to-plate configuration, such stamps allow for the uniform patterning of chip-scale Si substrates with hierarchical 3D antireflective and

antifouling patterns. The development of a Mac-Imprint system capable of conformal patterning onto non-flat substrates becomes possible due to the flexible and stretchable nature of gold-coated porous polymer stamps. Understanding of their mechanical behavior during conformal contact allows for the first implementation of Mac-Imprint to directly micromachine 3D hierarchical patterns onto plano-convex Si lenses, paving the way towards scalable fabrication of multifunctional 3D metasurfaces for applications in advanced optics.

ACKNOWLEDGMENTS

I am grateful to my advisor, Professor Bruno Azeredo for providing me with the opportunity to join his research group in 2017. It was a great privilege to have his constant support and guidance during all these years. He is an example of how far the “extra step” could lead in both professional and in personal lives and I could not have wished for a better mentor.

I would also like to thank current members and alumni of Prof. Azeredo’s research group for countless hours of discussions, which helped me to view things from different perspective and become a better researcher.

I want to acknowledge and the use of facilities with the LeRoy Eyring Center for Solid State Science at Arizona State University and John M. Cowley High Resolution Electron Microscopy, as well as all staff members at who contributed to this work.

I also want to thank my friends, both in the United States and in Belarus, for their emotional support.

I was very lucky to have my best friend, Dr. Stanislau Niauzorau, next to me along this way. We started our friendship and research journey together more than 10 years ago and since then have both grown personally and professionally. Over this time, he became my brother and I am very grateful for it.

I would like to express the gratitude to my parents who helped me during this journey, despite being physically thousands of kilometers away. I am lucky to have their support in all my endeavors throughout the whole life and I wouldn’t be here without them.

Lastly, I don't have enough words to thank my wife, Aksana. She was constantly with me through the ups and down of these years. Thanks to her I was able to feel the joy of the accomplishments and stay excited even when things were not working out. Her inner strength and continuous curiosity are the qualities that inspired me to stay motivated and focused in pursuit of the PhD degree.

TABLE OF CONTENTS

Page

LIST OF TABLES ... ix

LIST OF FIGURES ... x

CHAPTER

1 INTRODUCTION ... 1

1.1 Motivation ... 4

1.1.1 Understanding Resolution Limit of Mac-Imprint Towards Fabrication of Optoelectronic Devices ... 4

1.1.2 Advanced Mac-Imprint Stamps for Etching Solution Management Towards Full-Wafer Planar and Curvilinear Substrate Patterning ... 5

1.2 Scope of Research and Dissertation Outline ... 7

2 BACKGROUND AND LITERATURE REVIEW ... 10

2.1 Fundamentals of Metal-Assisted Chemical Etching ... 11

2.2. Mass-Transport Mechanisms During Metal-Assisted Chemical Etching 14

2.3. Controlled Catalyst Motion During Metal-Assisted Chemical Etching Towards 3d Patterning of Silicon ... 16

2.4 Fabrication of the Functional Optical Devices Using Metal-Assisted Chemical Etching ... 19

2.5 Direct Electrochemical Micromachining of Silicon ... 21

2.6 Mass-Transport Investigation in Mac-Imprint of Porous Si ... 22

2.7 Mac-Imprint of Monocrystalline Si ... 25

CHAPTER Page

2.7.1 Mac-Imprint with Solid Catalysts 25

2.7.2 Mac-Imprint with Porous Catalysts 27

2.8 Improvements to the Mac-Imprint System 32

3 ROUGHNESS SUPPRESSION IN ELECTROCHEMICAL NANOIMPRINTING OF SI FOR APPLICATIONS IN SILICON PHOTONICS 36

3.1 Introduction 37

3.2 Results and Discussion 41

3.2.1 Limiting Diffusional Pathways 41

3.2.2 Roughness Reduction and Its Fundamental Limits 50

3.2.3 Nanoscopic Defect Analysis 57

3.3 Conclusion 61

3.4 Methods 63

3.4.1 Substrate Preparation 63

3.4.2 Stamp Preparation 63

3.4.3 Mac-Imprint Setup and Conditions 67

3.4.4 Morphological, Structural and Functional Characterization 69

3.4.5 Scanning Electron Microscope Image Analysis 70

3.4.6 Statistical Analysis 72

4 ELECTROCHEMICAL NANOIMPRINTING OF SILICON LENSES: TOWARDS BIO-INSPIRED INFRARED META-OPTICS 75

4.1 Introduction 75

4.2 Results and Discussion 78

4.2.1 Proof of Concept. Plate-to-Plate Mac-Imprint 78

4.2.2 Development of the Conformal Mac-Imprint 86

4.2.3 Conformal Mac-Imprint of Plano-Convex Si Lens 90

4.3 Conclusion 91

4.4. Methods 93

4.4.1 Substrate Preparation 93

4.4.2 Stamp Preparation 93

4.4.3 Mac-Imprint Conditions and Setup 94

4.4.4 Numerical Modeling 96

4.4.5 Morphological, Structural and Functional Characterization 97

5 DISSERTATION CONCLUSION AND FUTURE DIRECTIONS 99

REFERENCES 102

APPENDIX

A ROUGHNESS REDUCTION IN ELECTROCHEMICAL NANOIMPRINTING OF SI WITH NANOPOROUS CATALYSTS 114

B MANAGEMENT OF THE ETCHING SOLUTION STORAGE REQUIREMENT IN THE LARGE-AREA MAC-IMPRINT USING POROUS POLYMER STAMPS 123

C OBTAINED RIGHTS AND PERMISSIONS 127

CHAPTER Page

D ORIGINAL VERSION OF PREVIOUSLY PUBLISHED ARTICLE ENTITLED "ROUGHNESS SUPPRESSION IN ELECTROCHEMICAL NANOIMPRINTING OF SI FOR APPLICATIONS IN SILICON PHOTONICS" 140

E RIGHTS AND PERMISSIONS FOR PREVIOUSLY PUBLISHED ARTICLE ENTITLED "ROUGHNESS SUPPRESSION IN ELECTROCHEMICAL NANOIMPRINTING OF SI FOR APPLICATIONS IN SILICON PHOTONICS" 182

LIST OF TABLES

Table Page

1. Calculated Ionic Concentrations of the Major Ionic Species 116

2. Summary of the Data Reported in Liu Et Al. and Calculated Overetching.....116

LIST OF FIGURES

Figure Page

1. Examples of Functional 3d Structures. A – SEM Image of the Facet of the Quantum Cascade Laser Demonstrating Micromachined Linear Grating with Variable Grove Depth, Width and Period (Highlighted in the Schematics on the Right). B – the Measured 2d Far-field Intensity of the Device Highlights Beam Divergence Angles of ~12° and ~16° in Vertical and Lateral Directions, Respectively. C – Bird's View SEM Image of the 3d Si Waveguide Bend Fabricated by Gray-scale E-beam Lithography with Inset in the Top Right Corner Demonstrating It's Optimized Refractive Index Profile. D – AFM Scan of Fabricated Bend. E – SEM Images of Polymeric Replica of the Compound Moth Eye Structure Demonstrating It's Hierarchical Nature. F – Demonstration of It's Broadband Antireflection in the Visible Range. G – Comparison of the Water Droplet Contact Angle on the Smooth Polymer Sphere (Left) and Moth Eye Replica with the Same Radius of Curvature (Right) Highlighting It's Hydrophobicity. Schematics of the Flat Lens with Multi-scale and Multi-level Periodic Structures and It's Anticipated Focal Length for the Different Wavelength of Light. I – Bird's View SEM Images of Fabricated Structure. J – It's 3d Profile. 2
2. A – Etch Rates as a Function of ρ. Open Circles: Penetration Rate of Ag Particles. Filled Squares: Etch Depth after NaOH Treatment. B – Bird's Eye SEM Images of Si Surface Etched at Different ρ Values. 13

Figure Page

3. A-C – Model of the Reactants Diffusion Through Thin Au Film; B – Bird's Eye SEM Image of the Si Etched with 20 nm Thick, 1.1 µm Wide Au Film; C - Bird's Eye SEM Image of the Si Etched with 10 nm Thick, 2 µm Wide Au Film. D-E - Model of the Reactants Diffusion Through Thin Porous Layer; E – Cross-sectional SEM Image of the Si 40 nm Thick, 390 nm Wide Au Film; F – Cross-sectional SEM Image of the Si Etched with 40 nm Thick, 710 nm Wide Au Film. 15
4. 3d Catalyst Motion During MACE. A–E – Schematics of Pinned Catalyst with Denoted Rotation Angle. F–G– Top-down SEM Images of Pinned Catalyst Motion During Si Etching for 4 Minutes. K – Schematics and SEM Images of the Free-standing FIB Pre-defined Catalyst. L – Schematics of the Catalyst Motion During MACE. M and N – SEM Images of the Motion of the Catalyst with Side Length of 350 nm and 700 nm, Respectively. 17
5. Analysis of the Attraction Forces Between Catalyst and Si in MACE. A – Schematics of the Experiment Setup in Which Gold Catalyst Is Pinned and It's Deformation upon Etching Is Measured Using AFM. B – AFM Measurement of Catalyst Beam Deformation upon Etching. C – Calculated Pressure (σ) Distribution Throughout Catalyst/Si Contact Interface. D – Dependence of the σ and Etch Depth (s) on the Concentration of the Hydrogen Peroxide. E – Etch Rate (v) as a Function of the Hydrogen Peroxide Concentration. 18

Figure Page

6. X-ray Zone Plate Fabrication Using MACE. A – Cross-sectional SEM Image of the Si Substrate Etched Without Vertical Directionality Control Structures. B – Cross-sectional SEM Image of the Si Substrate Etched with Vertical Directionality Control Structures (i.e. 10 µm Wide Catalyst Stripes on the Sides of the Pattern). C – Top-down SEM Image of the X-ray Zone Plate with Non-liner Pattern. D – Schematics of the Mace in Vapor Phase. E-G – SEM Images of the X-ray Zone Plates. 20
7. The Results of the First Attempt for Direct Patterning of Si Using Catalytic Structures. A and B – Top-down Low Magnification SEM Images of Stamp with Groove Structure and Etched Si, Respectively. C and D – Cross-sectional High Magnification SEM Images of Groove Structure and Etched Si, Respectively. E – Bird's Eye SEM of Si Substrate Etched with Pt Mesh with Porous Sponge as a Backing Material. F – Cross-sectional SEM Image of Individual Groove Highlighting Rough Surface. 21
8. A – the Results of Mac-Imprint onto Monocrystalline Si (Left Column) and Porous Si (Right Column). B – AFM Scans of Sinusoidal Mac-Imprint Stamp (Top) and Imprinted Porous Si Surface (Middle) at the Complimentary Locations and Their Difference (Bottom). C – Schematic of the Mass-transport Processes During Porous Si Imprinting. D – Porous Si Etch Rate as a Function of Porous Layer Thickness. E – Volume of Porous Si Removed as a Function of Pillar Heights. 23

Figure Page

9. Results of Monocrystalline Si Mac-Imprint with Solid Catalysts. A and B – Top-down SEM Images of Stamp and Imprinted Si, Respectively. C and D – AFM Line Scans of Stamp and Si, Respectively. E and F – Top-down SEM Images of Stamp and Imprinted Si, Respectively. G and H – AFM Area Scans of Stamp and Si, Respectively. High-magnification SEM Image Highlight Formation of Porous Si. I – Schematics of the Mac-Imprint Stamp Design. J and K – Top-down SEM Images of Stamp and Imprinted Si, Respectively. Scale Bars Are 200 nm. L – Results of Simultaneous Mac-Imprint of Various Patterns: Lines (L-2), Dots (L-3) and Rectangles (L-4). Scale Bars for L and L-1 Are 25 µm. Scale Bars for L-2 – L-4 Are 600 nm. 26

10. Results of the Monocrystalline Si Mac-Imprint with Nanoporous Au Stamps. A – Schematics of the Mac-Imprint Setup. B and C – Top-down SEM Images of Nanoporous Au Pyramidal Pattern. D –bird's View SEM Images of the Imprinted Si Surface. 28

11. Results of the Monocrystalline Si Mac-Imprint with Nanoporous Au Stamps. A – Schematics of the Mac-Imprint Setup. B and C – Top-down SEM Images of Coarse and Fine Nanoporous Au Electrodes, Respectively. D and E – Top-down SEM Images of the Inverted Pyramids Imprinted with Coarse and Fine Electrodes, Respectively. F and G – Top-down SEM Images of the Grooves Imprinted with Coarse and Fine Electrodes, Respectively. 30

Figure Page

12. Results of the Monocrystalline Si Mac-Imprint with Nanoporous Au Stamps. A – Top-down Optical Images of Pillar Arrays Mac-Imprinted with Stamps with Different PVF, Denoted in the Top Right Corner. B – Comparison Between AFM Scans of Stamp and Si Imprinted with PVF = 68% Stamp. C – Top-down SEM Images of the Porous Au with Different Pore Volume Fractions (Top Row) and Corresponding Imprinted Si Surface (Bottom Row). D – Influence of the Catalyst Surface Area on the Amount of the Etched Si. 31

13. Modulation of the Contact Uniformity During Mac-Imprint. A – Design of the Mac-Imprint System with Double Cushion for the Compensation of Misalignments. B-D – Schematics and Imprint Results of Unmodified System (B), Single Cushion System (C) and Double-cushion System (D). E – Photograph of the Mac-Imprint Stamp and Imprinted GaAs Substrate Highlighting the Macroscopic Contact Uniformity. F – Optical Image of the Imprinted Microlens Array. G – Depth Profile of the Microlenses Imprinted in the Four Corners of the Stamp. 33

Figure Page

14. Mac-Imprint System Improvements. A – Schematics of Classical Mac-Imprint System. B – Potentials on the Catalyst (Blue) and GaAs (Red) Interface. C – SEM Image of the Imprinted Surface. D – Cross-sectional Height Profiles of the Imprinted Hole (Blue) and Stamp's Pillar (Red). E – Schematics of Spatially-separated Mac-Imprint System. F – Potentials on the Catalyst (Blue) and GaAs (Red) Interface. G – SEM Image of the Imprinted Surface. H – Cross-sectional Height Profiles of the Holes Imprinted with Spatially-separated (Blue) and Classical (Red) Mac-Imprint. I – Schematics of Spatially-separated Photo-enhanced Mac-Imprint System. J – Potentials on the Catalyst (Blue) and GaAs (Red) Interface. K – SEM Image of the Imprinted Surface. L – Cross-sectional Height Profile of the Imprinted Hole. 34
15. A – Schematics of the Catalytic Stamp and Patterned SOI Wafer Interaction During Mac-Imprint; B and C – Top-down SEM Images of Catalytic Stamp and Si Rib Waveguide Patterns Respectively. The Coordinate Systems Indicate the Parallel (X), Perpendicular (Y) and Vertical (Z) Directions Relative to the Principal Axis of the Waveguide. Arrows Highlight the Solution Diffusion Pathways: Red - Through the Embedded Channels Towards the Center of the SOI Pillar, and White – Through the Catalyst In-between Embedded Channels and Waveguide Patterns............... 39

Figure Page

16. A and B – Schematic Cross-section and Top-down SEM Images Respectively of Waveguide Arrays Imprinting with Solid Au Catalyst. Inset in B Highlights the Beginning of Porous Silicon Formation Region. C and D – Schematic Cross-section and Top-down SEM Images Respectively of the Waveguide Arrays Imprinting with Porous Au Catalyst. Solid Yellow Arrows Indicate the Length of the Region with Distinguishable Waveguide Pattern (EEPD). 42
17. Analysis of the EEPD Limitation. A – Schematics of the Mac-Imprint onto the Blank SOI Chip. B – Photograph of the Mac-Imprinted SOI Chip. C – Optical Image of the Edge of Imprinted Area Highlighting the EEPD. 44
18. Adjustment of the Etching Solution to Compensate for the Increasing Catalyst Surface Area. A – SEM Image of the Waveguide Imprinted with Porous Catalyst at ρ = 98.0 %. B – SEM Image of the Waveguide Imprinted with Porous Catalyst at ρ = 99.5 %. 45
19. A and B – Schematics of Charge- and Mass-transport Processes. C and D – High-magnification Top-down SEM Images of the Individual Waveguides. Holes Are Added to Illustrate the Charge Carrier Distribution Around Catalyst/Si Interface. White Arrows Point to the Visible Pores. A, C and B, D Correspond to Mac-Imprint with Solid and Porous Catalysts, Respectively. 47

Figure Page

20. Depth Analysis of Imprinted Waveguide with Uniform Depth Showing (A) Large Area AFM Scan of a Single Waveguide from the Edge (Left) to the Center (Right) of the SOI Pillar, and (B) Waveguide's Depth Profile (Black Squares) and 3 Point Moving Average (Red Squares) with Inset Highlighting One of the Waveguide's Cross-section and Depth Measurement (Label D). The Bottom Sub-20 nm Roughness of the Waveguide Surroundings Induced by the Catalyst Cannot Be Detected Due to the Low Resolution of the Large-area AFM Scan Shown in (A). Data Represents Depth Extracted Through Fitting of Step-height Function with Error Bar Representing Fitting Error. 49

Figure Page

21. Theoretical Model for Band Bending During Anodic Electrochemical Machining of Si Proposed by Sugita Et Al. Dashed Lines at Metal-Solution Interface Represent Isopotentials Within the Electrical Double Layer (Debye Length) and Solid Lines Represent Isopotentials Bending Around the Triple Junction. B and C – Schematics of the Overetching for the Negative and Positive Si Features, Respectively (Not to Scale). D – Plot of Silicon Hole Versus Catalyst Diameter Using Imported Data from Liu Et Al. Three Lines with a Unity Slope Are Plotted with Different Offsets: Zero (Black - Reference), Best Fit of Experimental Data (Blue, φ1) and Two times the Debye Length (Red, φ2). φ1 on the Bar Plot Is Reported as Average ± Standard Deviation Based on 9 Reported Measurements. The Upper Inset Contains Top-down SEM Images of the Metal Catalyst and the Resulting Hole in Silicon. 51
22. Top-down SEM Images of the Catalytic Stamps with Different Average Pore Diameters (A-D) and Imprinted Waveguide Surroundings (E-H). The Boxes in the Top Right Corner of the SEM Images Contain the Average Pore (A-D) and Protrusion (E-H) Diameters. Dependence of Si Protrusion Size on the Catalyst Pore Size (I). Inset on I Illustrate How the Feature Size (Either Pore or Protrusion) Was Calculated. Dependence of Nearest Neighbor Distance on the Catalyst Pore Size and Si Protrusion Size (J, Red and Black, Respectively). Inset on J Illustrate How the Nearest Neighbor Distance Was Calculated. Data Is Reported as Average ± Standard Deviation. Red Dashed Lines on I and J Indicate the Resolution Limit (i.e. Double the Debye Length). 53

Figure Page

23. Top-down SEM Images and Edge Profiles (Framed with Red Dashed Lines) of the Waveguides, Imprinted with Porous Catalysts with Average Pore Sizes 42-10 nm Respectively. E – Waveguide Line Edge Roughness as a Function of Catalyst Pores Size. Data Is Reported as Average ± Standard Deviation. Dashed Lines Indicate Twice the Debye Length (Red) and Solid Au Stamp Sidewall LER (Black). 56

24. A and B – Top-down SEM and Optical Images of a Single Imprinted Waveguide Respectively. C and D – Maps of Raman Signal Peak Position and Full Width at Half-maximum Respectively, Taken at Locations Marked on B. E and F – Average Values for Raman Peak Position and Full Width at Half-maximum, Respectively, of the Waveguide at Location Marked on B. Data Is Reported as Average ± Standard Deviation. Red Dashed Lines on E and F Highlight the Raman Peak Position and Full Width at Half Maximum of the Blank SOI Wafer. 58

25. A – Top-down Optical Image of the Individual SOI Pillar Prior to Waveguide Testing. B – Top-down Infrared Image of the Individual SOI Pillar During Waveguide Testing. Dashed Lines on a and B Highlight the Tested Waveguide. C – Side-view of Waveguide Mode Simulation. D – Cross-sectional Schematics of the Waveguide, Used for the Simulation. E – Side-view of Simulated Waveguide Mode, Corrected by PSF of 0.42 Numerical Aperture Objective. F – Side-view Infrared Image of the Output Waveguide Facet. 60

Figure Page

26. PDMS Replica Molding Procedure. 64
27. Waveguide Pattern Transfer onto the SU-8 Layer Using Soft Nanoimprint Lithography. 65
28. Schematics of the Thin-film Catalyst Deposition by Magnetron Sputtering and Photographs of the Process. 66
29. Mac-Imprint System. A - Photograph of the Mac-Imprint System in the Disengaged State. B – Photograph of the Stamp-to-Substrate Alignment Step with Omnidirectional UV Curing. 68
30. Analysis of the np-Au Pore Sizes Using Aquami (A-D) and ImageJ (E-F). A and E – Original Top-down SEM Images. B and F – Threshold Operation. C and G – Outlines of Individual Pores. Note, Lines Within the Outlines on C Represent Weighted Centers of the Pores with Colors Representing Distance to It's Edges. D and H – Distribution of the Pore Diameters.. 71
31. LER Analysis. A – Original Top-down SEM Image with Highlighted Portion of the Waveguide for the Python Algorithm. B – Cropped Portion of the Waveguide Imported into the Python Algorithm. C – Extracted Line Edge Profile. 73
32. Nearest Neighbor Distance Analysis with Original Top down SEM Image (A), Threshold Mask (B) and Distances Between Centers of Five Nearest Neighbors (C, Red Arrows). 74

Figure Page

33. Conformal Electrochemical Nanoimprinting of Si Lens. (A) Compound Moth Eye Structure with SEM Images Highlighting Hierarchical Structure of It's Ommatidia. (B) Antifouling Shark Skin with SEM Images Highlighting Ridges on It's Scales. (C) Concept of Broadband Omnidirectional Antireflective Surface Monolithycally Integrated onto the Plano-convex Lens. (D) Optical Image of the Uniformly Patterned Plano-convex Si Lens Demonstrating Strong Light Diffraction from the Imprinted Surface. The Lens Is Placed next to the Picture of Vitruvian Man on the Back of 1 Euro Coin for Size Comparison. SEM Image Demonstrates a Unit Cell of Imprinted Sharklet Pattern. 76

34. Development of the Mac-Imprint Stamps. A – First Generation Stamps in Which the Reactant Diffusion Pathways Were Embedded into the Porous Catalytic Layer of the Stamp and Etching Solution Storage Was Embedded into the Substrate. B – Proposed next Generation of the Stamps in Which Both Reactant Diffusion Pathways and Etching Solution Storage Would Be Embedded into the Stamp. .. 79

35. Proof of Concept. A – Schematics of Mac-Imprint with Second Generation of the Stamps. B – Photograph of Imprinted Si Chip. C – SEM Images of the Si Surface, Imprinted with Random Protrusions. D – SEM Image of the Second Generation of the Stamps. E – Water Contact Angle with Bare Si Chip. F – Water Contact Angle with Imprinted Si Chip. G – Hemispherical Reflectance of Imprinted Si Chip Relative to Bare Si. 81

Figure Page

36. Mac-Imprint of Hierarchical Patterns. A – Schematics of Mac-Imprint with the Third Generation of the Stamps. B – Photograph of Imprinted Si Chip. C – SEM Images of the Si Surface, Imprinted with Sharklet Patterns. D – SEM Image of the Third Generation of the Stamps. E – Water Contact Angle with Bare Si Chip. F – Water Contact Angle with Imprinted Si Chip. G – Hemispherical Reflectance of Imprinted Si Chip Relative to Bare Si. 83

37. Analysis of the Surface Topology of Porous PVDF Plate-to-Plate Stamps. A – Optical Image of the Commercial PVDF Stamp. Red Square Highlights Portion of the Stamp Used for the Large Area Optical Profilometry. B – Photograph of the Imprinted Si Chip. C – Large-area Optical Profilometry. D – Small-area Optical Profilometry. E – Optical Image of the TIPS PVDF Stamp. Red Square Highlights Portion of the Stamp Used for the Large Area Optical Profilometry. F – Photograph of the Imprinted Si Chip. G – Large-area Optical Profilometry. H – Small-area Optical Profilometry. 85

Figure Page

38. Test of the Conformal Mac-Imprint Configuration. A – Schematics of the Conformal Mac-Imprint of Flat Si Chip and Photographs of Flexible and Stretchable Stamp (Left) and Imprinted Si Chip (Right). B – Schematics of the Plate-to-Plate Mac-Imprint of Flat Si Chip and Photographs of Rigid Stamp (Left) and Si Chip Imprinted with Tip-and-Tilt Misalignment (Right). C – Schematics of the Catalyst Stretchability Test. D – Photograph of the Test Setup. E – Electrical Conductance of the Membrane as a Function of Catalyst Thickness and Applied Air Pressure. F – Schematics of the Membrane Permeability Test Setup. G – Schematics of the Ionic Movement Through Partially Clogged Membrane (Left) and Completely Clogged Membrane (Right). H – Current Density as a Function of Catalyst Thickness. I – Schematics of the Membrane Deflection Test. J – Photograph of the Test Setup. K – Membrane Deflection in It's Center as a Function of Applied Air Pressure. L – Schematics of the Conformal Mac-Imprint with Flat Si Chip. M – Photograph of the Conformal Mac-Imprint with Flat Si Chip. N – Variation of the Imprinted Pattern Period as a Function of the Radial Distance from the Center of the Contact Point and Applied Air Pressure. 87

Figure Page

39. Conformal Mac-Imprint onto Plano-convex Si Lens. A – Schematics of the Conformal Contact to the Curvilinear Object. B – Photograph of the Mac-Imprinted Lens. C and D – Optical Profilometry of the Imprinted Lens. E and F – Raman Peak Position and Full Width at Half-maximum, Respectively. G – Hemispherical Reflectance of Imprinted Si Lens Relative to Bare Si. 91

40. Conformal Mac-Imprint Set-up. A – Schematics of the Electrochemical Cell for Conformal Mac-Imprint. B – Demonstration of Conformal Mac-Imprint Process in Dry Conditions. 96

41. Screenshot of the Half Symmetric Two-dimensional Simulation Geometry. A – Full-view of the Simulation Geometry Capturing PTFE Top Part, Compressed O-ring, Composite Stamp (Not Marked) and Metal Base. B – Zoom in into the Composite Stamp Highlighting It's Two-layer Structure Composed of PVDF (Top) and PI (Bottom). 97

42. AFM Profiles of Mac-Imprint Stamp (A) and Imprinted Silicon (B) Taken in Complementary Locations. C – Line Profiles of Stamp Heights (Blue) and Silicon Etch Depth (Black). Red Lines Represent Three-point Moving Average. Vertical Black Dashed Lines Highlight Distinguishable Features Appearing on Both Stamp and Imprinted Si. 118

Figure Page

43. Relation Between Minimum Line Width Resolution and Line Edge Roughness. Solid Black Lines Represent the Edge of Imprinted Line (LEP). Dotted Red Lines Represent the Average Line Edge Profile (LEP_{aver}). Dotted Black Lines Represent 6 Sigma Interval for the LEP Deviation from LEP_{aver}. 119
44. Top-down (A, C) and Cross-sectional (B, D) SEM Images of the Catalyst Films with Average Pore Diameters of 42 (A, B) and 10 (C, D) nm. 119
45. A – Simulated Waveguide Mode with W = 750 nm, H = 43 nm. B – Point Spread Function (PSF) for a NA = 0.42 Objective Operating at 1310 nm. C – Convolution Between A and B Indicating the Expected IR Image. D – Measured IR Image as Averaged over 1290 to 1330 nm... 120
46. Buried Oxide Layer Undercut During Mac-Imprint. A – Schematic of the Undercut. B-D – Top down SEM Images of the Edge of the Pillars, Processed Within 65, 70 and 75 Sec, Respectively. 121
47. Estimated Etching Solution Storage. A – Inside the Unit Cell of the Pre-patterned Si Wafer. B – Inside the Porous Polymer. 125
48. Top-down SEM Images of Commercial PVDF Membranes Coated with the Different Thickness Catalyst. A – 80 nm. B – 320 nm, C – 3000 nm. 125
49. Total Hemispherical Reflectance of Si Chips, Mac-Imprinted with Commercial PVDF Membranes. 126
50. Analysis of the Pattern Distortions During Conformal Mac-Imprint. 126

CHAPTER 1

INTRODUCTION

Three-dimensional (3D) hierarchical structures allow to tailor surface properties of the materials and achieve unique applications in metasurface-based plasmonics *(1, 2)*, optoelectronics *(3, 4)*, bio-inspired conventional *(5)* and planar *(6–8)* optics and more. For example, a linear grating with variable grove depth, width and period directly machined on the sidewall of terahertz quantum cascade lasers (Figure 1A) using focused ion beam (FIB) milling has significantly reduced the divergence of laser's beam (Figure 1B)*(1)*. Si waveguides with non-rectangular cross-sectional profile fabricated via gray-scale electron beam (e-beam) lithography (Figure 1, C and D) have demonstrated reduction of the inter-mode coupling in the multimode waveguide bends *(3)*. The hierarchical structure of the compound moth eye (Figure 1E) has inspired fabrication of plano-convex polymer lenses with superior antireflection properties in the broadband wavelength range (Figure 1F) and hydrophobicity for self-cleaning applications (Figure 1G) *(5)*. Flat lenses with multi-level microstructures fabricated by the grayscale lithography have demonstrated broadband light focusing with correction for chromatic aberration (Figure 1H-J) *(6)*.

Up to date such devices were fabricated on a lab scale with little effort being put towards their integration into the large-volume industrial production. The reason behind it lies in the complexity of the processes involved in the manufacturing of such devices that often compromise between three-dimensionality and scalability of the fabricated patterns.

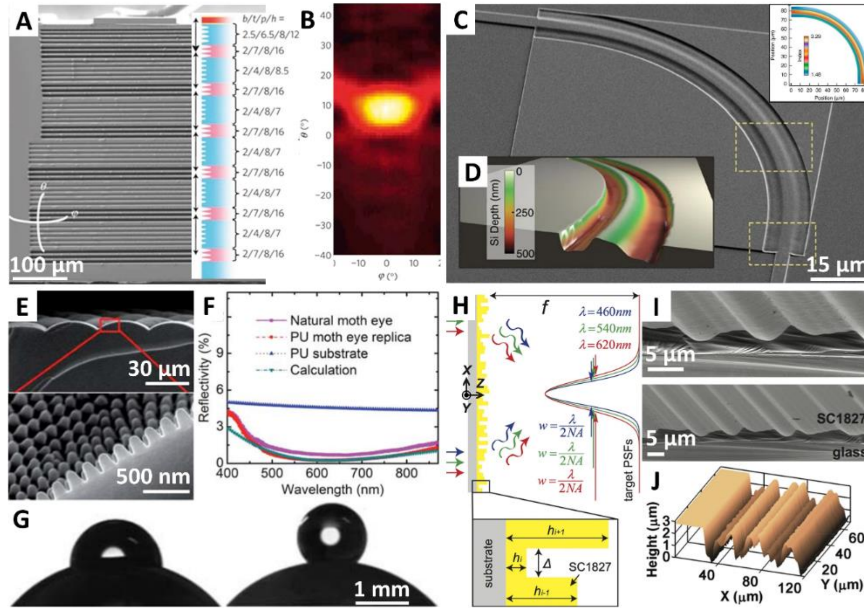

Figure 1. Examples of functional 3D structures. A –SEM image of the facet of the quantum cascade laser demonstrating micromachined linear grating with variable grove depth, width and period (highlighted in the schematics on the right). B – The measured 2D far-field intensity of the device highlights beam divergence angles of ~12° and ~16° in vertical and lateral directions, respectively. Reproduced with the permission from *(1)*. C – Bird's view SEM image of the 3D Si waveguide bend fabricated by gray-scale e-beam lithography with inset in the top right corner demonstrating it's optimized refractive index profile. D – AFM scan of fabricated bend. Reproduced with the permission from *(3)*. E – SEM images of polymeric replica of the compound moth eye structure demonstrating it's hierarchical nature. F – Demonstration of it's broadband antireflection in the visible range. G – Comparison of the water droplet contact angle on the smooth polymer sphere (left) and moth eye replica with the same radius of curvature (right) highlighting it's hydrophobicity. Reproduce with the permission from *(5)*. Schematics of the flat lens with multi-scale and multi-level periodic structures and it's anticipated focal length for the different wavelength of light. I – Bird's view SEM images of fabricated structure. J – It's 3D profile. Reproduced with the permission from *(6)*.

For instance, direct-write micromachining (i.e., FIB milling, e-beam lithography) can fabricate patterns with superior 3D control on the wide range of substrates (i.e., polymers,

semiconductors, metals), but is plagued by the slow-throughput. On the other hand, parallel micromachining methods such as various types of ultraviolet (UV) photolithography (i.e., extreme, deep) can scalably fabricate 2D patterns on the surface of polymer films with sub-10 nm in-plane resolution *(9)*, which are subsequently used as a sacrificial masks for pattering of various substrates using plasma-based reactive ion etching (RIE). The latter, however, (i) struggles to provide simultaneous and independent control over lateral feature size and etch depth due to the aspect ratio dependent etch rates *(10, 11)* which is exacerbated on the non-planar surfaces *(12, 13)* and (ii) induces sidewall roughness of the etched structures also known as scalloping effect *(14, 15)*. This is particularly detrimental for the photonic structures where optically smooth surfaces are critical to minimize light scattering losses *(16, 17)*. The only process that can scalably fabricate various 3D patterns with sub-10 nm resolution is nanoimprint lithography (NIL) which utilizes stamps to plastically reflow polymer substrates upon mechanical contact between former and latter *(18, 19)*.

Its electrochemical version, called Metal-Assisted Electrochemical Nanoimprinting (Mac-Imprint) extends the process onto inorganic semiconductors (i.e., Si, GaAs) *(20, 21)*. In Mac-Imprint, the pattern transfer from the stamp to the substrate relies on the metal-assisted chemical etching of semiconductors (MACE) *(22)*, which is localized at the points of contact with catalytic metal-coated stamp in the presence of etching solution. This process is advantageous over other semiconductor micromachining techniques because it allows to by-pass the need of RIE. Moreover, Mac-Imprint (i) operates below elastic limits of stamp and substrate materials and (ii) retrieves catalytic metal upon the imprint, both of

which improve the stamp's reusability *(20)*. Despite its advantages, one of the major limitations of Mac-Imprint is mass-transport dependency of the process which has been studied under the literature on MACE. This prevents scaling of the technique in terms of (i) minimal achievable pattern roughness and resolution and (ii) maximum patternable area. Up-to-date, few studies have been conducted to understand and address both of the abovementioned limitations which prevents Mac-Imprint from becoming an industrial micromachining processes. These problems have motivated two major directions of the dissertation.

1.1 Motivation

First, this work is motivated by the pursue of understanding fundamental mechanisms behind resolution limit of Mac-Imprint which directly affects its ability to fabricate functional optical devices for silicon photonics, co-packaged optics and optical interconnects. Second, this work is motivated by the management of macroscopic etching solution storage during Mac-Imprint that is paramount for extending it to chip- and wafer scale applications. The subsections below elaborate on the specific problems behind these two topics.

1.1.1 Understanding Resolution Limit of Mac-Imprint Towards Fabrication of Optoelectronic Devices

Since the development of Mac-Imprint, research efforts have been focused on the fabrication of various 3D microscopic patterns with high pattern transfer fidelity. Owning to the wet nature of the process, it was established that the latter requires free exchange of

the reactants and byproducts throughout the microscopic metal catalyst/semiconductor contact interface *(20)*. If the metal catalyst layer is solid, mass-transport through its grain boundaries is typically not sufficient which leads to the semiconductor substrate porosification and results in poor pattern transfer fidelity *(20)*. This issue has been by-passed with the aid of nanoporous catalytic films which allowed one to Mac-Imprint arrays of inverted pyramids *(23)* or parabolic concentrators *(24)*.

While necessary, this approach results in the nanoscale roughening of the Mac-Imprinted surfaces which occurs because the pore size of the nanoporous catalysts exceeds the resolution limit of the technique. The surface roughness is especially critical for the optoelectronic devices due to the high light scattering losses and has to be minimized if Mac-Imprint were to be implemented for the fabrication of functional optoelectronic devices. Until now, this issue has not been properly addressed due to the insufficient understanding of the fundamental mechanisms behind the etching resolution of MACE and Mac-Imprint.

1.1.2 Advanced Mac-Imprint Stamps for Etching Solution Management Towards Full-Wafer Planar and Curvilinear Substrate Patterning

On the microscopic level, the management of the etching solution mass-transport through the nanoporous catalysts offers clear improvements to the pattern transfer fidelity of Mac-Imprint. This approach, however, fails on the macroscopic level due to limited etching solution storage capacity of the nanoporous thin-film catalyst. Specifically, upon the contact between the centimeter-scale stamp and the substrate, the initial amount of etching solution stored in the porous thin-film catalyst or in the microscale liquid gap

entrapped between the stamp and substrate is quickly depleted which leads to limited etch depths of less than 1 micrometer, and uneven etch depth throughout the stamp/substrate contact interface with shallower etch depth in the center and deeper close to it's edges *(25)*.

This issue has been previously addressed by designing arrays of macroscopic pillars (i.e., 500x500x200 µm) on the surface of the semiconductor substrate prior to performing Mac-Imprint. The spacing between them provided etching solution storage volume uniformly distributed throughout the contact interface between stamp and substrate. Thus, each individual semiconductor pillar was successfully patterned with arrays of parabolic concentrators *(24)* or waveguides with high etch depth uniformity *(25)*. This approach, however, limits the footprint of the fabricated devices and does not allow for "true" full-wafer patterning which is required for Mac-Imprint's integration into industry.

A potential solution to this problem is the use of fully porous stamps that can simultaneously (i) provide diffusional pathways to the bulk of the etching solution and (ii) act as a solution storage reservoirs. However, the attempt to employ stamps made completely out of porous catalyst was not entirely successful due to the formation of the porous Si defects during Mac-Imprint which was associated with the high surface area of the catalyst *(23, 26)*. Moreover, the hard nature of such stamps limits Mac-Imprint to planar substrates as it does not allow for the conformal contact to curvilinear surfaces. The latter can be achieved if the stamps are made out of flexible and stretchable materials analogously to the conformal formats of regular NIL *(27)*. Both of these issues require re-thinking of Mac-Imprint stamp fabrication with a renewed emphasis on (i) high pore-volume fraction materials with (ii) chemical inertness and (iii) flexibility.

1.2 Scope of Research and Dissertation Outline

In light of the discussed motivation, this dissertation pursues two objectives. At first, it investigates the resolution limit of Mac-Imprint and it's effect on the reduction of the nanoporous catalyst-induced Si roughness. This knowledge is then applied for the first time to fabricate functional Si rib waveguide using Mac-Imprint. Secondly, a new class of flexible stamps made out of fully porous polymer membranes is developed and employed for the centimeter-scale Mac-Imprint of Si chips and plano-convex Si lenses.

The first part of the dissertation is focused on the reduction of the surface roughness induced by the morphology of the nanoporous catalysts and it's effect on the fabrication of Si waveguides. At first, it was demonstrated that the waveguide-specific geometries can not be Mac-Imprinted onto the pre-patterned silicon-on-insulator (SOI) wafers with high pattern transfer fidelity using solid catalysts due to the restricted mass-transport in the direction perpendicular to the primary axis of the waveguide. Consequently, nanoporous catalysts made by dealloying of Au/Ag alloy were implemented as a mass-transport enabling media which allowed to Mac-Imprint arrays of Si waveguides with high pattern transfer fidelity and etch depth uniformity. Next, the theoretical resolution limit of Mac-Imprint is hypothesized to be proportional to the Debye length and discussed in the context of existing literature on the electrochemical *(28)* and MACE *(29)* etching of Si. Based on this hypothesis, nanoporous catalyst-induced Si surface roughness was minimized by the reduction of the catalyst's pore sizes to approach the resolution limit of Mac-Imprint. At the smallest pore size, the grain morphology of the nanoporous catalyst was distinguished on the surface of the Mac-Imprinted Si which further supports the proposed hypothesis. It

was established that the sidewall roughness of the fabricated Si waveguides is proportional to the surface morphology of the catalyst and at its smallest levels is comparable with that of the waveguides fabricated by conventional photolithography and RIE. Lastly, the functionality of the fabricated Si waveguides was demonstrated in the light propagation tests which revealed single mode light propagation with limited levels of sidewall scattering closely matching simulation results.

The second part of the dissertation is focused on the development of the next generation of Mac-Imprint stamps with (i) enhanced etching solution storage capacity and (ii) flexibility and stretchability. Gold-coated highly-porous polyvinylidene fluoride (PVDF) membranes are proposed for this task. At first, commercially available porous PVDF membranes were employed for the plate-to-plate Mac-Imprint of centimeter scale Si chips and the results are discussed in context of both microscopic pattern transfer fidelity and macroscopic patterning uniformity as well as anti-reflective optical properties of the imprinted surfaces. Based on these preliminary results, this thesis explored patternable porous PVDF membranes made by thermally-induced phase separation as an ideal material for Mac-Imprint. Such membranes with hierarchical periodic patterns are subsequently fabricated and tested in the plate-to-plate configuration. Next, a pressure actuated Mac-Imprint setup has been developed for conformal imprinting of flat and curvilinear Si substrates. In this context, the mechanical stability of the flexible PVDF stamps becomes paramount due to the development of the bi-axial stresses upon the stamp inflation which could lead to the cracking and delamination of the thin-film catalyst layer. Thus, the integrity of the thin film catalyst was investigated using the electrical conductance

measurements as a function of the catalyst film thickness and applied air pressure. Next, a finite-element elastic model has been developed to predict the stress and strain levels in the membranes upon inflation and has been validated using experimental data. Implementation of this model allows to establish range of Mac-Imprint operational conditions upon which stamps do not overcome elastic deformation limits which assures membrane's reusability and reproducibility of the imprint results over many imprinting cycles. The implementation of the model for the prediction of the stamp's pattern distortions and necessity for its reverse engineering upon membrane fabrication is discussed in the context of the future work. Lastly, the pressure-actuation Mac-Imprint setup has been implemented for the conformal Mac-Imprint of flat Si chips and plano-convex Si lenses with radius of curvature of 36.4 mm.

The last part of the dissertation summarizes its major outcomes and provides recommendations for the future directions of Mac-Imprint development towards (i) roughness minimization, (ii) improvement of the large-area patterning and (iii) integration with the existing commercial micromachining processes.

CHAPTER 2

BACKGROUND AND LITERATURE REVIEW

The objective of this chapter is to introduce Mac-Imprint as a method and to provide its current state-of-the-art and limitations. At first, this chapter focuses on the in-depth review of the fundamental mechanism behind Mac-Imprint which is MACE. Here, the electrochemical reactions of the Si dissolution catalyzed by the noble metal are presented. Next, the stoichiometric balance between these reaction is discussed in the context of the rate of electrochemical etching as well as the formation of porous silicon defects. The discussion continues with the introduction of the current understanding of the mass-transport mechanisms behind these reactions and its relation to the pattern transfer fidelity and formation of porous silicon defects. Next, motion of the catalyst during Si dissolution controlled by the attraction forces between former and latter and independent from the crystallography orientation of Si is presented as a way to fabricate arbitrary 3D patterns. After the discussions of MACE, the chapter transitions to the historical perspective of Mac-Imprint and challenges associated with its development. Here, the importance of the mass-transport for the high pattern transfer fidelity inherited and exacerbated from MACE is presented and discussed in the context of the first successful Mac-Imprint of intentionally porosified Si substrates. The chapter continues with the discussion of different approaches aimed to overcome diffusional limitations of Mac-Imprint which were focused on the management of mass-transport. Lastly, current best method for the Mac-Imprint of monocrystalline Si substrates is presented and its results and limitations are discussed in the context of the motivation for this dissertation.

2.1 Fundamentals of Metal-Assisted Chemical Etching

In 1997, Dimova-Malinovska et al. *(30)* has firstly reported the results of porous Si fabrication in the etching solution of $HF:HNO_3:H_2O$ = 1:3:5, where etching was facilitated by the presence of thin Al film on the surface of Si wafer. The authors came to this conclusion because the Si etching in the similar solution without Al presence required so-called "incubation" time, a delay between Si immersion in the solution and beginning of the etching. In 2002, X. Li and P. W. Bohn *(22)* investigated the influence of the Au, Pt or Au/Pd nanoparticles on the etching of Si in the aqueous solutions of HF, H_2O_2 and EtOH (1:1:1 by vol.) demonstrating the concomitant anisotropic etching of silicon underneath the catalyst-semiconductor interface and porous silicon formation. They also introduced, for the first time, the method and term "Metal-assisted chemical etching" in literature. They have established that Si etching was localized around catalytic metal particles resulting in the formation of porous Si layer with interconnected or columnar pore structure in p^+ or p^- and n^+ silicon, respectively. It was proposed that the localized etching is the result of two electrochemical reactions occurring simultaneously on the catalytic metal particles (cathode sites) and Si surface (anode site). Cathodic reaction is described by the reduction of the hydrogen peroxide, catalyzed by metal nanoparticles *(22, 31)* during which positive charge carriers (holes) are generated:

$$H_2O_2 + 2H^+ \rightarrow 2H_2O + 2h^+ \qquad E_0 = +1.76\ V/NHE \qquad (1)$$

Next, the holes are injected into the Si under the catalyst nanoparticles through metal/Si Schottky junction *(32, 33)*. The heights of the Schottky barrier strongly depends on the work function of the used metal (Cu, Au, Ag, Pt, Al), doping type and level of the Si substrate, as well as externally applied bias *(32, 33)*. These holes are subsequently consumed during the anodic reaction of Si dissolution *(31)*:

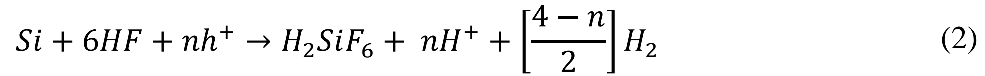

$$Si + 6HF + nh^{+} \rightarrow H_2SiF_6 + nH^{+} + \left[\frac{4-n}{2}\right] H_2 \qquad (2)$$

Thus, the overall balanced reaction of the MACE process can be written as following *(22, 31)*:

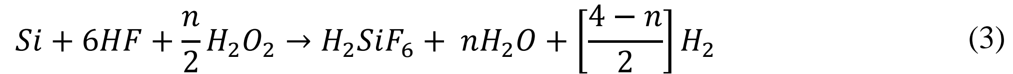

$$Si + 6HF + \frac{n}{2} H_2O_2 \rightarrow H_2SiF_6 + nH_2O + \left[\frac{4-n}{2}\right] H_2 \qquad (3)$$

The kinetics of the cathodic and anodic reactions plays critical role in the MACE of Si. Chartier et al. in 2008 *(31)* has established that the ratio of the HF to H_2O_2 in the solution affects the rate of Si dissolution as well as the confinement of the etching in the proximity of the catalyst nanoparticles. He came up with solution parameter ρ, a ratio of the molar concentration of HF to HF and H_2O_2, which has been coined as the "Chartier-Bastide ratio", and can be described as follows:

$$\rho = [HF]/([HF] + [H_2O_2]) \qquad (4)$$

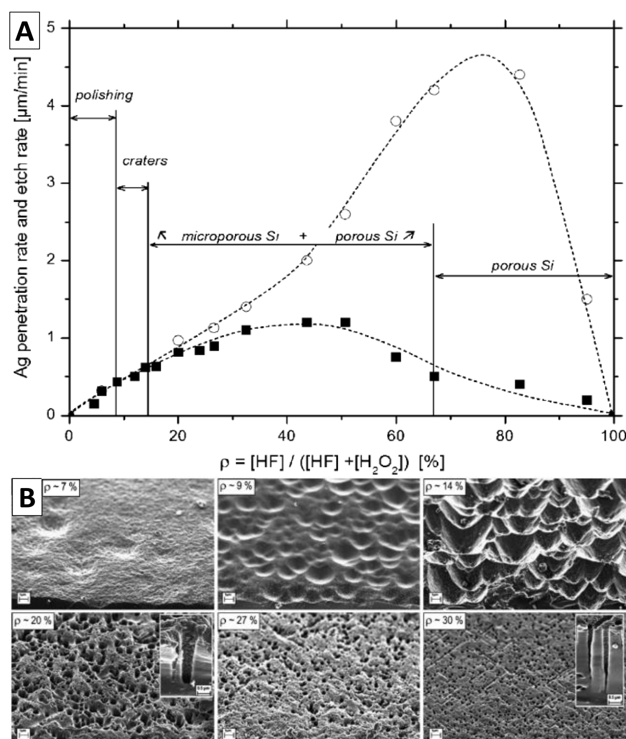

Figure 2. A – Etch rates as a function of ρ. Open circles: penetration rate of Ag particles. Filled squares: etch depth after NaOH treatment. B – Bird's eye SEM images of Si surface etched at different ρ values. Reproduced with the permission from *(31)*. Copyright 2008, Elsevier.

It was firstly established that the Si etching was localized around catalyst nanoparticles and their penetration rate into Si substrate of the was maximized at ρ ~ 75% (Figure 2A, open circles) due to the reactions (1) and (2) existing in stoichiometric balance. This result holds true if the particles are small (<100 nm) and do not pose mass-transport limitations. With the reduction of the H_2O_2 concentration and increase of ρ beyond 75%, the catalyst nanoparticle penetration rate decreased because rate of hole generation becomes smaller than of its consumption. The etching, however, remains highly localized around catalyst nanoparticle. On the other hand, the increase of the H_2O_2 concentration from its stoichiometry values (9%< ρ < 75%) leads to formation of the porous Si around

catalyst nanoparticles was (Figure 2B). At the $\rho < 7\%$ MACE has entered so-called "polishing" regime, where Si surface becomes macroscopically smooth. It was proposed that with the increase of H_2O_2 concentration injected holes are able to diffuse away from metal/Si contact interface and participate in the secondary reaction of Si porosification.

2.2. Mass-Transport Mechanisms During Metal-Assisted Chemical Etching

Another important aspect that has attracted a lot of attention during the study of the MACE process is a mass-transport phenomena during Si dissolution. Currently, three main models are considered *(33, 34)* (Figure 3): (i) diffusion of the reactants and by-products through thin catalyst *(35–37)*; (ii) diffusion of the reactants and by-products through thin porous Si layer underneath the catalyst *(38, 39)*, and (iii) diffusion of the Si atoms through catalyst film, their catalytic oxidation and subsequent dissolution on the surface of metal film *(40)*. In support of the first model Li et al. *(35)* has conducted MACE of Si under two different conditions. Specifically, 20 nm thick and 1.1 μm wide (Figure 3B) and 10 nm thick and 2 μm wide (Figure 3C) Au strips were used to pattern trenches in Si substrate. It was observed that when Au layer thickness reaches a certain threshold value (20 nm in current study), the mass-transport of the reactants through its grain boundaries can no longer be supported to achieve uniform Si dissolution which leads to faster etching around the edges of the strip (Figure 3B). However, when the catalyst thickness was kept below 20 nm the trench in Si was etched uniformly throughout the entire catalyst/Si interface (Figure 3C) thus supporting the first mass-transport model. With regards to the second mass-transport model (Figure 3D), Geyer et al. *(34)* has tested MACE of Si with Au strips which had fixed thickness of 40 nm and different width of 390 nm and 710 nm (Figure 3,

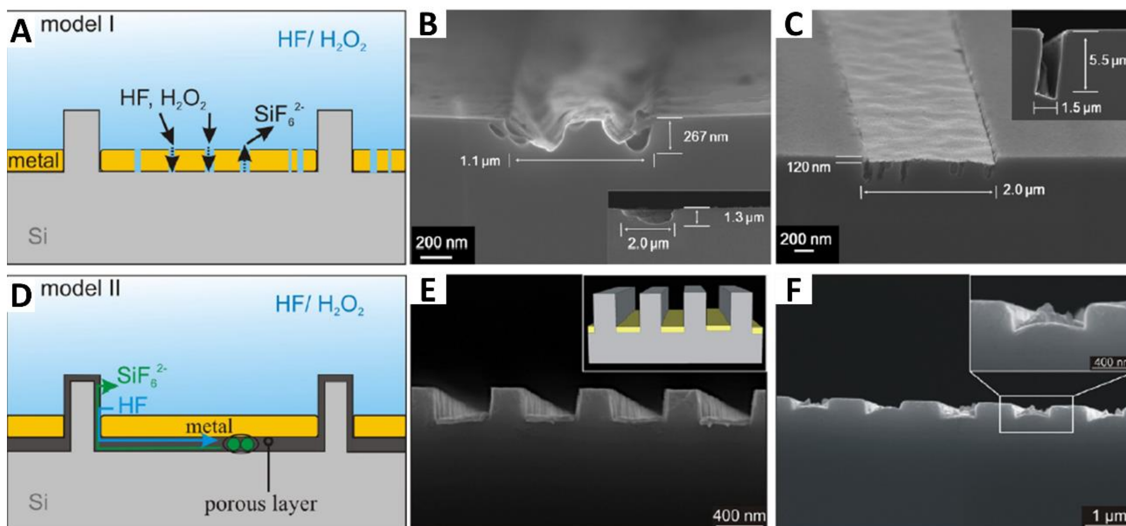

Figure 3. A-C – Model of the reactants diffusion through thin Au film; B – bird's eye SEM image of the Si etched with 20 nm thick, 1.1 µm wide Au film; C - bird's eye SEM image of the Si etched with 10 nm thick, 2 µm wide Au film *(34, 35)*. D-E - Model of the reactants diffusion through thin porous layer; E – cross-sectional SEM image of the Si 40 nm thick, 390 nm wide Au film; F – cross-sectional SEM image of the Si etched with 40 nm thick, 710 nm wide Au film *(34)*. A, D-E, F - Reproduced with the permission from *(34)*. Copyright 2012, American Chemical Society; B, C - Reproduced with the permission from *(35)*. Copyright 2014, American Chemical Society.

E and F respectively). In the former case, a uniform vertical etching was observed (Figure 3E) indicating that the mass-transport of the etching solution was not restricted. Additionally, high magnification SEM images revealed the formation of thin porous Si layer underneath metal catalyst stripe even though the etching solution used in the study had very low H_2O_2 concentration (ρ ~ 98%). On the other hand, MACE with 710 nm wide strip resulted in the non-uniform etch profile with etching being more pronounced near the edges of the strip (Figure 3E), although porous Si layer was also observed in this case. The increase of the strip width beyond 1 µm further exacerbated the problem. Following observations lead to the conclusion that the proposed model is valid, albeit the thin porous

Si film can only support constant mass-transport required for the uniform etching on the length scales of around 500 nm. As of now there is no direct evidence for either of the models being dominant during MACE of Si. In fact, both of them could be simultaneously happening, competing with each other and prevailing in particular MACE cases (catalyst geometry and etching conditions).

2.3. Controlled Catalyst Motion During Metal-Assisted Chemical Etching Towards 3d Patterning of Silicon

The ability of MACE to etch different crystallography orientations of Si *(41–43)* makes it of particular interest for low-cost and high-throughput fabrication of various 3D patterns using 2D templates. In 2011 Hildreth et al. *(44)* demonstrated the out-of-plane Si etching using patterned pinned catalyst with controlled geometry. It was established that by varying the distance between pinpoints as well as width of the catalyst arm it was possible to achieve full 3D control of the etch profile (Figure 4A-J). This was attributed the attraction forces between Si and catalyst during MACE and their competition with geometric constraints of the catalyst patterns. Specifically, based on the analysis of the catalyst deformation performed using the SEM images, these forces were calculated to be within 0.5-3.51 μN with corresponding pressures ranging between 0.5-3.9 MPa. These findings ruled out the possibility of gravitational nature of catalyst motion. Thus, several other forces were proposed and compared to the previous research including electrophoresis and van der Waals with fast electrophoresis being a most likely candidate for the catalyst driving force during MACE. The authors, however, highlighted that their results were not adequate for the determination of the specific catalyst driving forces.

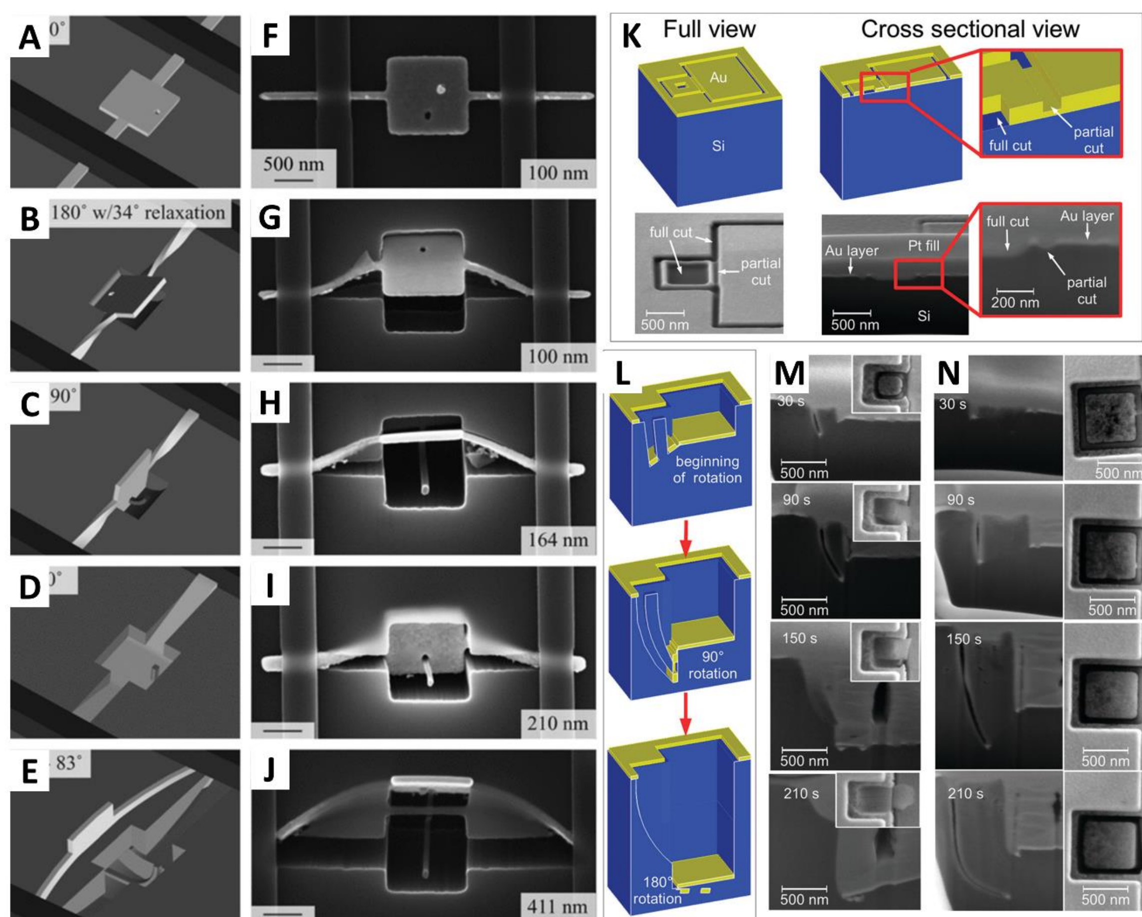

Figure 4. 3D catalyst motion during MACE. A–E – Schematics of pinned catalyst with denoted rotation angle. F–G – Top-down SEM images of pinned catalyst motion during Si etching for 4 minutes. A–J reprtinted with permission from *(44)*.K – Schematics and SEM images of the free-standing FIB pre-defined catalyst. L – Schematics of the catalyst motion during MACE. M and N – SEM images of the motion of the catalyst with side length of 350 nm and 700 nm, respectively. K–N reprinted with permission from *(45)*.

Another study on the control of catalyst motion during MACE was conducted by Rykaczewski et al. *(45)* in which the catalyst film was not intentionally restricted, but it's shape was predefined using FIB milling (Figure 4K). The study was also able to achieve 3D etching with high catalyst motion control which was attributed to the difference in the Si etch rates under the catalysts with mismatched characteristic dimensions (Figure 4L-N)

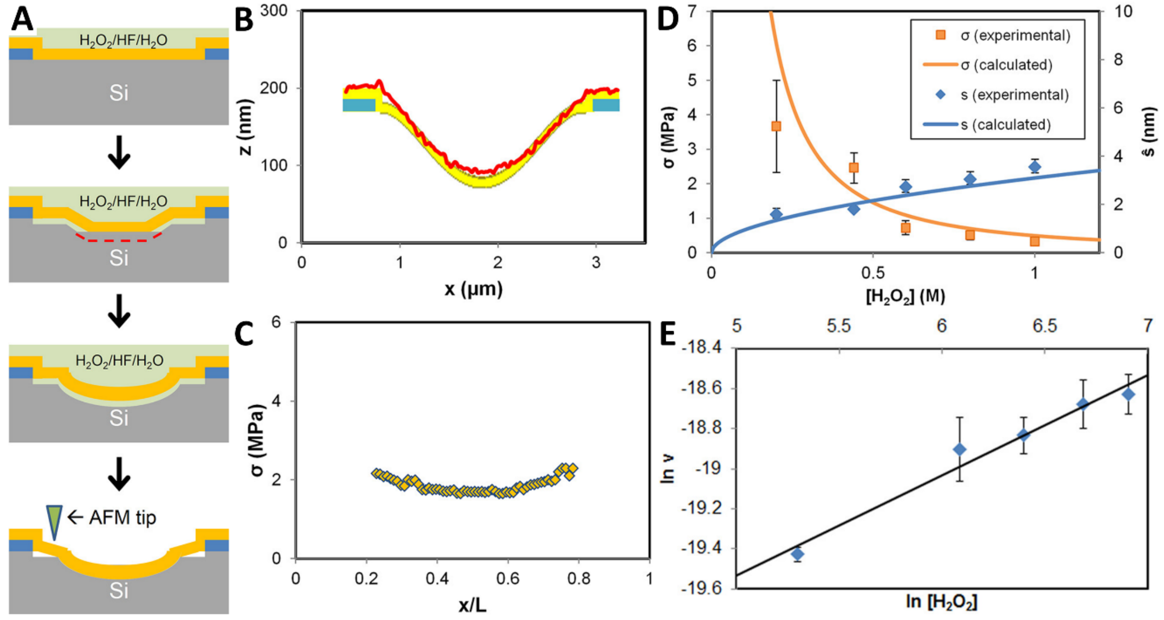

Figure 5. Analysis of the attraction forces between catalyst and Si in MACE. A – Schematics of the experiment setup in which gold catalyst is pinned and it's deformation upon etching is measured using AFM. B – AFM measurement of catalyst beam deformation upon etching. C – Calculated pressure (σ) distribution throughout catalyst/Si contact interface. D – Dependence of the σ and etch depth (s) on the concentration of the hydrogen peroxide. E – Etch rate (v) as a function of the hydrogen peroxide concentration. Reprinted with permission from *(46)*.

as well it's shaping prior MACE aimed to facilitate bending motion. These examples highlight versatility of MACE which allows fabrication of arbitrary 3D dimensional structures. These approaches, however possess several disadvantages that are associated with the (i) necessity for careful experiment design to achieve desired etching profile and (ii) non-reusability of the catalyst.

With the purpose of better understanding the mechanism behind the catalyst motion in MACE, Lai et al. designed and conducted series of experiments *(46)* in which the catalyst was also pinned on the both sides (like in the studies of Hildreth et al. *(44)*). It's

geometry, however, was simplified to a single beam in order to avoid rotational movement and only allow for the elastic deformation, which was accurately measured *ex situ* using the AFM (Figure 5A). Upon the etching the catalyst beam deformation was observed with the maximum deflection happening in the middle point between two pin-points (Figure 5B). Based on these measurements the pressures (σ) were calculated to be ~2 MPa (Figure 5C) which falls in the range of values estimated by Hildreth et al. *(44)*. Careful analysis of the σ and etch rate (v) as a function of the hydrogen peroxide concentration revealed the inverse relation in the former (Figure 5D) and direct relation in the latter (Figure 5E). These findings contradicted hypothesis of the electrophoretic motion of the catalyst as σ is expected to be proportional to v, thus it was concluded that the van der Waals forces are the main mechanism behind catalyst motion in MACE.

2.4 Fabrication of the Functional Optical Devices Using Metal-Assisted Chemical Etching

The ability of MACE to fabricate high aspect-ratio structures (i.e. Si nanowires) with sub-10 nm resolution was exploited to fabricate zone plates for X-ray optics *(47, 48)*. An important requirement for it was to achieve control over vertical directionality of etching. In 2014 Chang et al. *(47)* has demonstrated the use of sacrificial catalytic structures acting as an electron-hole concentration balancers which allowed to achieve uniform concentration profile of injected electron-holes throughout the catalyst/Si contact interface and significantly improve vertical directionality of etching (Figure 6A and B). This approach allowed vertical etching with 100:1 aspect-ratio which was used to fabricate non-linear patterns for high-performance X-ray zone plates (Figure 6C). Another interesting

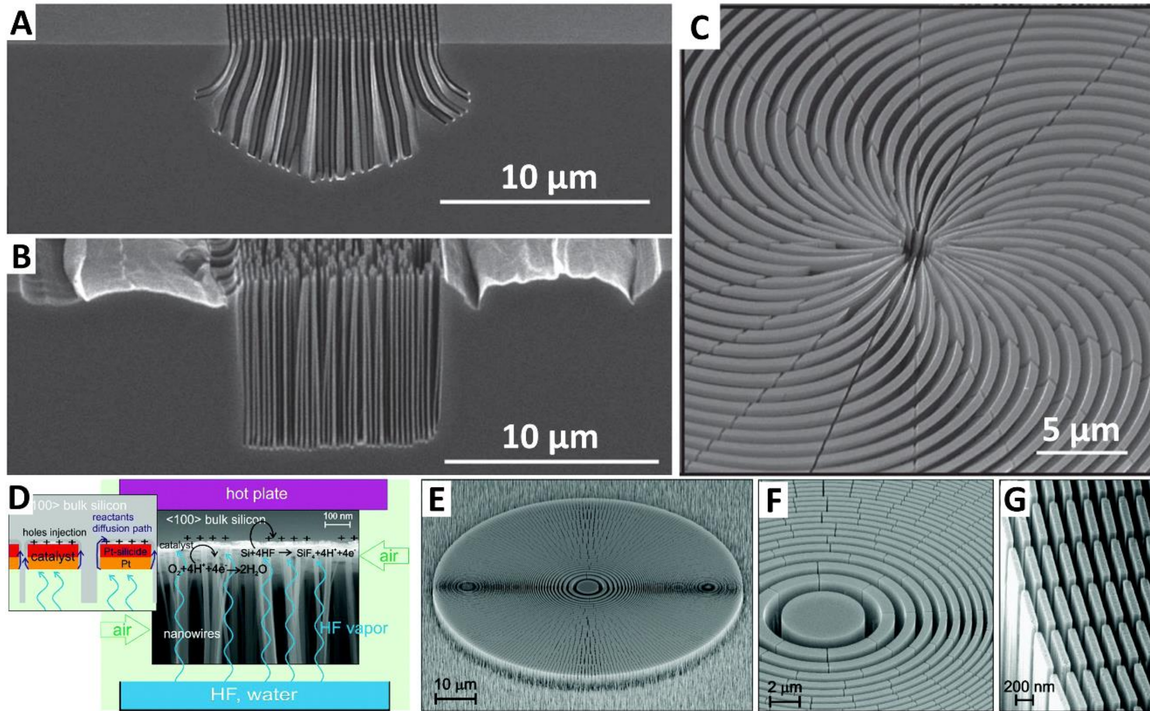

Figure 6. X-ray zone plate fabrication using MACE. A – Cross-sectional SEM image of the Si substrate etched without vertical directionality control structures. B – Cross-sectional SEM image of the Si substrate etched with vertical directionality control structures (i.e. 10 µm wide catalyst stripes on the sides of the pattern). C – Top-down SEM image of the X-ray zone plate with non-liner pattern. A-C reprinted with permission from *(47)*. D – Schematics of the MACE in vapor phase. E-G – SEM images of the X-ray zone plates. D-G reproduced with permission from *(48)*.

approach was demonstrated by Romano et al. *(48)* in which MACE was performed in the vapor phase with the schematics of the process demonstrated on Figure 6D. Here, the etchant was supplied through the evaporation of the diluted HF acid while the O_2 was used as an oxidant and was supplied from the continuous airflow. At first, this technique allowed to fabricate vertically aligned Si nanowires with high aspect ratio and reduced agglomeration comparing to the classical MACE in liquid phase. This process then was extended to fabricate X-ray zone plates with aspect-ratio of about 80:1.

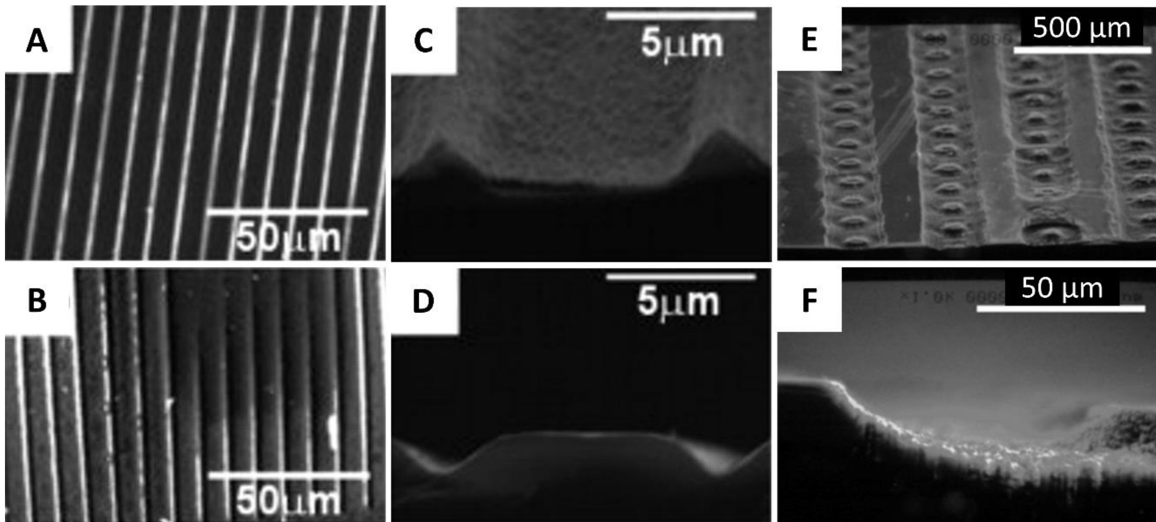

Figure 7. The results of the first attempt for direct patterning of Si using catalytic structures. A and B – top-down low magnification SEM images of stamp with groove structure and etched Si, respectively. C and D – cross-sectional high magnification SEM images of groove structure and etched Si, respectively. Reproduced with permission from *(49)*. E – bird's eye SEM of Si substrate etched with Pt mesh with porous sponge as a backing material. F – cross-sectional SEM image of individual groove highlighting rough surface. Reproduced with permission from *(50)*.

2.5 Direct Electrochemical Micromachining of Silicon

The necessity of the defect-free low-cost and high-throughput Si patterning with optically smooth 3D structures pushed the development of novel nano- and micromachining techniques. In the 2011 Fukushima et al. *(49)* has firstly reported the patterning of mono- and polycrystalline Si wafers with Pt-coated pyramidal structures in the presence HF/H_2O_2 etching solution. Authors have observed the transfer of the pyramidal structures onto Si (Figure 7, A-C) around the perimeter of the stamp and attributed it to the insufficient etching solution in the center of the stamp/Si contact. This method was called "Surface structure transfer". Two years later the same group has

published a results of Si surface patterning with Pt mesh *(50)*. In the study Pt mesh was attached to the porous material and brought in full contact with 6" Si wafer. The etching solution of HF and H_2O_2 was supplied through the back of porous material using syringe. This technique allowed to pattern Si surface with 200 μm wide groves with etch depth varying form 5 to 80 μm depending on the contact time and etching solution composition (Figure 7, E and F). In both reported cases the patterning was accompanied by the formation of the Si nanoctrystalline layer. Although it was favorable to the goal of the research (reduction of the Si reflection in the visible range), this could be critical for the fabrication of devices, where optical smoothness is required. Moreover, these studies did not focus on the microscopic mass-transport limitations of the process.

2.6 Mass-Transport Investigation in Mac-Imprint of Porous Si

In 2016 Azeredo et al. *(20)* demonstrated patterning of porous Si with diffraction gratings, parabolic cylinders and paraboloids. It was achieved by the implementation of Mac-Imprint, a combination of MACE and nanoimprint lithography. In this method, Au-coated polymer stamps possessing 10 μm wide 3D features (parabolic cylinders and paraboloids) as well as diffraction gratings with period of 1 μm were brought in contact with the intentionally porosified Si wafers, prepatterned with 400 μm wide pillars spaced by 900 μm in the presence of the etching solution. The imprinting is a result of two simultaneously occurring cathodic (1) and anodic (2) reactions. The solution parameter ρ was kept high (between 90 and 98 %) in order to confine the etching reaction around catalyst/porous Si contact interface. In the work, the authors have established the necessity of the porous Si layer for the facilitation of the mass-transport (Figure 8A). In particular,

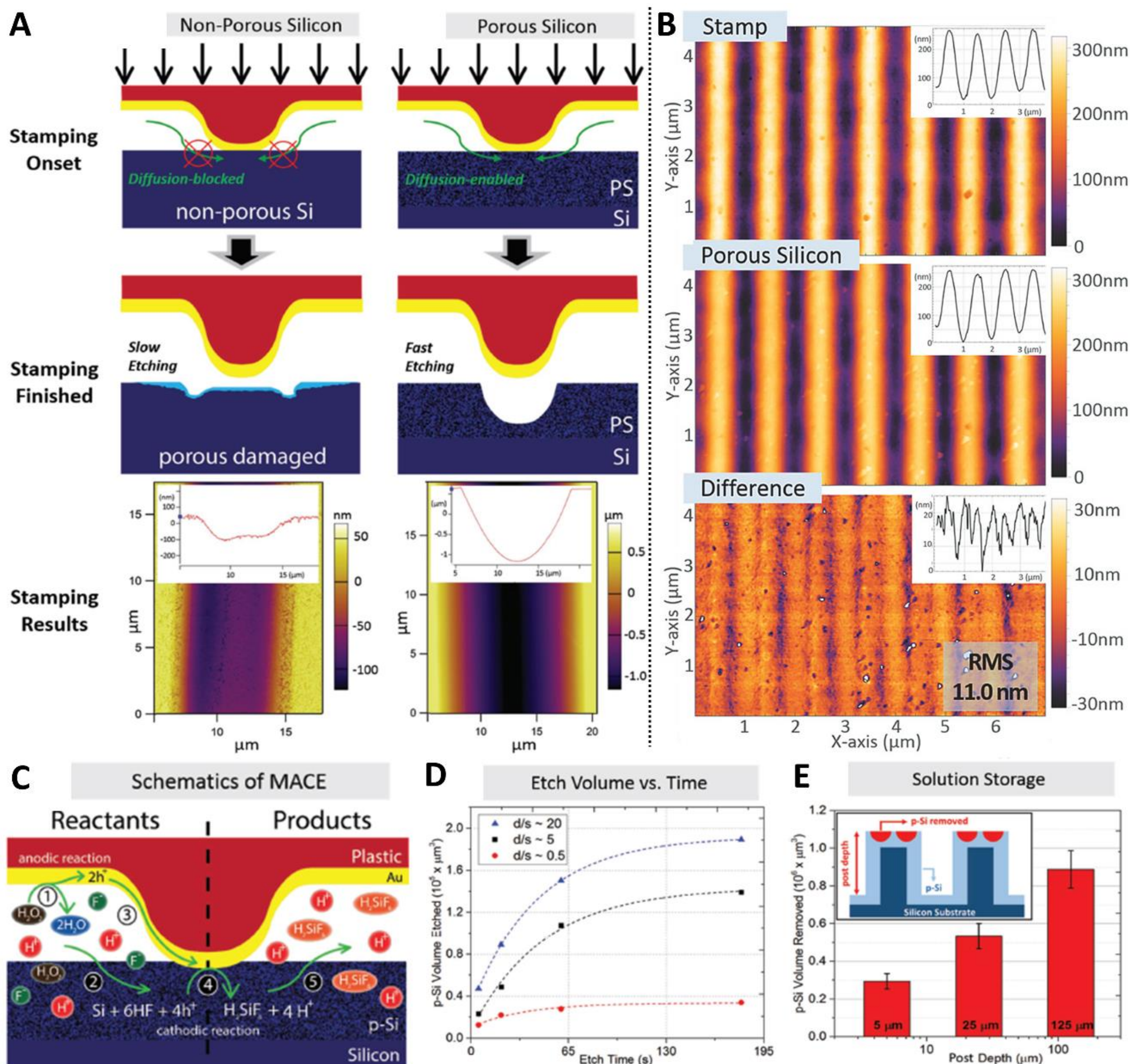

Figure 8. A – The results of Mac-Imprint onto monocrystalline Si (left column) and porous Si (right column). B – AFM scans of sinusoidal Mac-Imprint stamp (top) and imprinted porous Si surface (middle) at the complimentary locations and their difference (bottom). C – Schematic of the mass-transport processes during porous Si imprinting. D – porous Si etch rate as a function of porous layer thickness. E – volume of porous Si removed a s a function of pillar heights. Reproduced with the permission from *(20)*. Copyright 2016, Willey-VCH.

the attempt to Mac-Imprint parabolic cylinder with width of ~10 μm onto monocrystalline nonporous Si wafer with a solid and impervious gold-coated stamp resulted in lack of

pattern transfer fidelity (Figure 8A, left column). Moreover, unintentional porosification of Si near it's contact interface with the catalyst was observed. These results are consistent with the mass-transport model II, discussed in the previous section dedicated to mass-transport mechanisms in MACE. However, when the porous Si layer with controlled thickness was intentionally fabricated prior Mac-Imprint (Figure 8A, right column), the imprinted pattern matched the shape of the used stamp due to the facilitated mass-transport (Figure 8C). The high pattern transfer fidelity was further confirmed by comparing the AFM scans of Mac-Imprint stamp with sinusoidal patterns and imprinted porous Si, acquired in the complementary locations (Figure 8B). The RMS of height difference between former and latter was found to be 11 nm which highlighted the accuracy of the process. It was also observed that the etch rate during Mac-Imprint does not scale linearly with the etch time which was attributed to the gradual depletion of the etching solution species resulting in the reduction of the etch rate (Figure 8D). Additionally, the etch rate and imprint depth was investigated as a function of the thickness of porous Si layer. It was found that use of thicker porous Si layers resulted in faster and deeper etching (Figure 8D, black and blue curves) which was explained by (i) better mass-transport of etching solution and (ii) larger quantities of etching solution stored in the porous Si in the proximity of the etching reaction. In addition to the previous findings, it was also proposed that Si wafer prepatterning with 400 μm wide pillars spaced by 900 μm is necessary in order to provide solution storage confined between stamp and substrate in the close proximity to the etching interfaces. Figure 8E represent the dependence of the etched porous Si volume as a function of pillar heights. The etching conditions (i.e. ρ, time and contact force) were kept constant

throughout the experiments. As can be clearly seen from the diagram, the amount of the stored etching solution is in direct positive relation with the volume of the etched porous Si, or, in other words, etch depth.

2.7 Mac-Imprint of Monocrystalline Si

The findings of Azeredo et al. *(20)* have demonstrated the importance of mass-transport for the high pattern transfer fidelity in Mac-Imprint. The authors also highlighted its difference from the classical MACE in which the etching solution is abundant around the catalyst/Si contact interface. These findings paved the way for the Mac-Imprint of monocrystalline Si which was independently developed in two directions.

2.7.1 Mac-Imprint with Solid Catalysts

In 2017 Zhang et al. *(51)* demonstrated the Mac-Imprint of monocrystalline Si with sub-micrometer pillars fabricated by NIL. It was observed that the relatively small lateral sizes of the pillars (i.e., ~340 nm) were accurately transferred onto monocrystalline Si without observable porous Si formation (Figure 9A-D) which is in agreement with the mass-transport model II in classical MACE. Additionally, the etch depth in this case was equal to ~112 nm which is only 20% of the height of the stamp pillars. At this heights, the diameter of the etched Si hole was equal to 364 nm. In the same study the stamp's pattern size was increased to several micrometers (i.e., 3.5 µm) and the pattern transfer was still observed with imprinted details as small as 110 nm (Figure 9E-H). However, in this case an extensive formation of porous Si during Mac-Imprint was detected (Figure 9H). These experimental results are in good agreement with the findings of Azeredo et al. highlighting

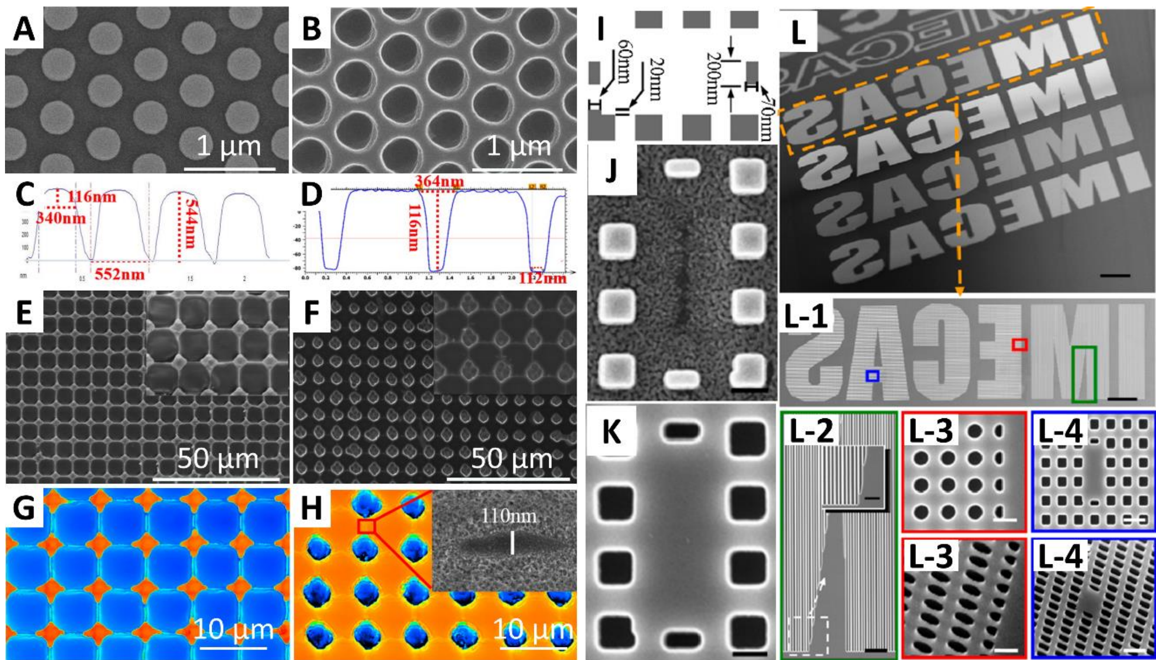

Figure 9. Results of monocrystalline Si Mac-Imprint with solid catalysts. A and B – top-down SEM images of stamp and imprinted Si, respectively. C and D – AFM line scans of stamp and Si, respectively. E and F – top-down SEM images of stamp and imprinted Si, respectively. G and H – AFM area scans of stamp and Si, respectively. High-magnification SEM image highlight formation of porous Si. A – H are reproduced with permission from *(51)*. I – schematics of the Mac-Imprint stamp design. J and K – top-down SEM images of stamp and imprinted Si, respectively. Scale bars are 200 nm. L – results of simultaneous Mac-Imprint of various patterns: lines (L-2), dots (L-3) and rectangles (L-4). Scale bars for L and L-1 are 25 µm. Scale bars for L-2 – L-4 are 600 nm. I – L are reproduced with premission from *(52)*.

the restricted mass-transport in the Mac-Imprint of features whose lateral size exceeds several hundreds of nm.

In 2019 Li et al. *(52)* has performed a series of experiments in which the stamps possessed nanoscale patterns with different geometry, which highlighted several important aspects of Mac-Imprint. At first, the successful transfer of features as small as 20 nm by 60 nm was demonstrated (Figure 9I-K). Secondly, it was possible to Mac-Imprint

structures with different lateral sizes in the same cycle with the uniform etch rate dictated by the largest pattern size (Figure 9I-J). Thirdly, arrays of trenches as long as 76 µm were successfully Mac-Imprinted. Importantly (Figure 9L), in every case the width of the patterns was kept below 250 nm. This geometry allowed for the efficient mass-transport of the etching solution with limited levels of porous Si formation.

2.7.2 Mac-Imprint with Porous Catalysts

Torralba et al. *(26)* in 2017 has firstly reported the combination of nanoporous Au films and anodic-formats of Mac-Imprint – obtained by externally biasing a Pt counter electrode in the solution against the gold catalyst - as another way to pattern monocrystalline Si without mass-transport restrictions. The stamps were electrically connected to the potentiostat and brought in light contact (0.04 lbf) with the monocrystalline Si wafer in the presence of 5M HF aqueous solution (Figure 10A). In this study the 3D etching capability of Mac-Imprint was highlighted by using stamps with pyramidal structures with the dimensions approaching 15 µm in all three directions. The stamps were made out of fully porous gold films with total radius of 10 mm, patterned central area of 64 mm^2 and overall thickness of 350 µm. Such stamp design was achieved by sintering AuAg powders in patterned Si mold and subsequent electrochemical dealloying of sintered film at elevated temperatures. These dealloying conditions resulted in highly developed porous Au networks (Figure 10, B and C) with total surface area of 9-11 $m^2 \cdot g^{-1}$. The experiment established the relation between externally applied bias and etch

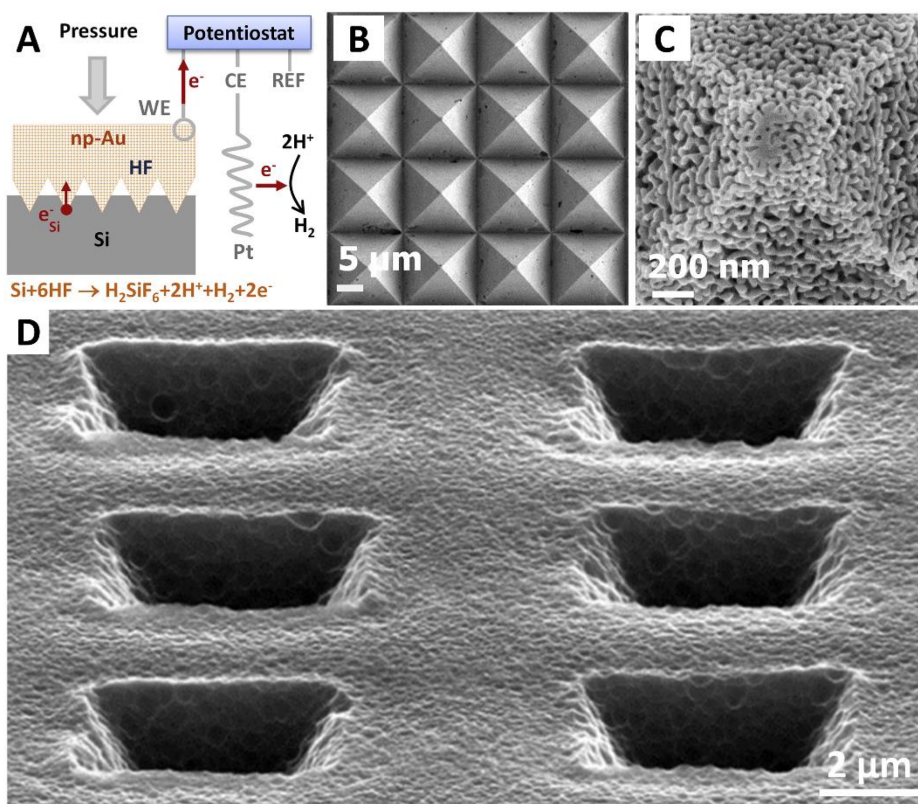

Figure 10. Results of the monocrystalline Si Mac-Imprint with nanoporous Au stamps. A – schematics of the Mac-Imprint setup. B and C – Top-down SEM images of nanoporous Au pyramidal pattern D –bird's view SEM images of the imprinted Si surface. Reproduced with the permission from *(26)*. Copyright 2017, Elsevier.

rate with the highest etch rate of 0.5 $\mu m \cdot min^{-1}$ achieved at positive biasing of 0.3 V against Mercury/Mercurous Sulfate Reference Electrode (SME). These conditions yielded uniform Si substrate patterning with inverted pyramid structures with the opening areas of ~25 μm^2 and etch depth of ~3.6 μm. (Figure 10D) over the 1 mm^2 area. The imprinted pattern also maintained original period of the stamps. These results were attributed to the fully porous nature of the stamps which allowed for unrestricted mass-transport. It should be noted that albeit the pyramidal pattern was transferred uniformly, the imprinted Si surface was

significantly porosified and roughened which was explained by misbalance between hole injection and consumption rates resulting in the delocalization of the etching reaction.

In 2019, two independent studies on the Mac-Imprint of monocrystalline Si with nanoporous Au catalysts with variable pore sizes were reported. The first work of Bastide et al. *(23)* was focused on Mac-Imprint of inverted pyramids and groves onto the surface of Si using nanoporous Au stamps with coarse (Figure 11B) and fine (Figure 11C) porosity with and without external biasing. The stamp fabrication strategy remained the same as in *(26)* except stamps with the coarse porosity were dealloyed without external biasing. All of the approaches reported successful pattern transfer (Figure 11D-G). Remarkably, a complete pattern transfer of the pyramidal structure was achieved with coarse gold electrode (Figure 11D) under positive biasing of 0.2 V against SME during 20 min with maximum etch rate of 0.36 $\mu m \cdot min^{-1}$. Similar results were achieved during the Mac-Imprint without external biasing. However, both Si surface roughening and Si surface porosification was observed with the latter being exacerbated in the case of catalyst with fine porosity (Figure 11, E and G). This observation was attributed to incomplete Ag removal during the dealloying which lead to it's re-deposition on the surface of Si and delocalization of the etching.

In the second work *(24)* arrays of parabolic cylinders with lateral sizes of 8 µm were imprinted onto the monocrystalline Si substrate predefined with pillars similarly to *(20)*. Stamp's parabolic patterns were fabricated using photolithography and dewetting of the photoresist with subsequent sputter-coating of thin Ag/Au layer and it's dealloying. By varying dealloying conditions the work has investigated influence of the pore volume

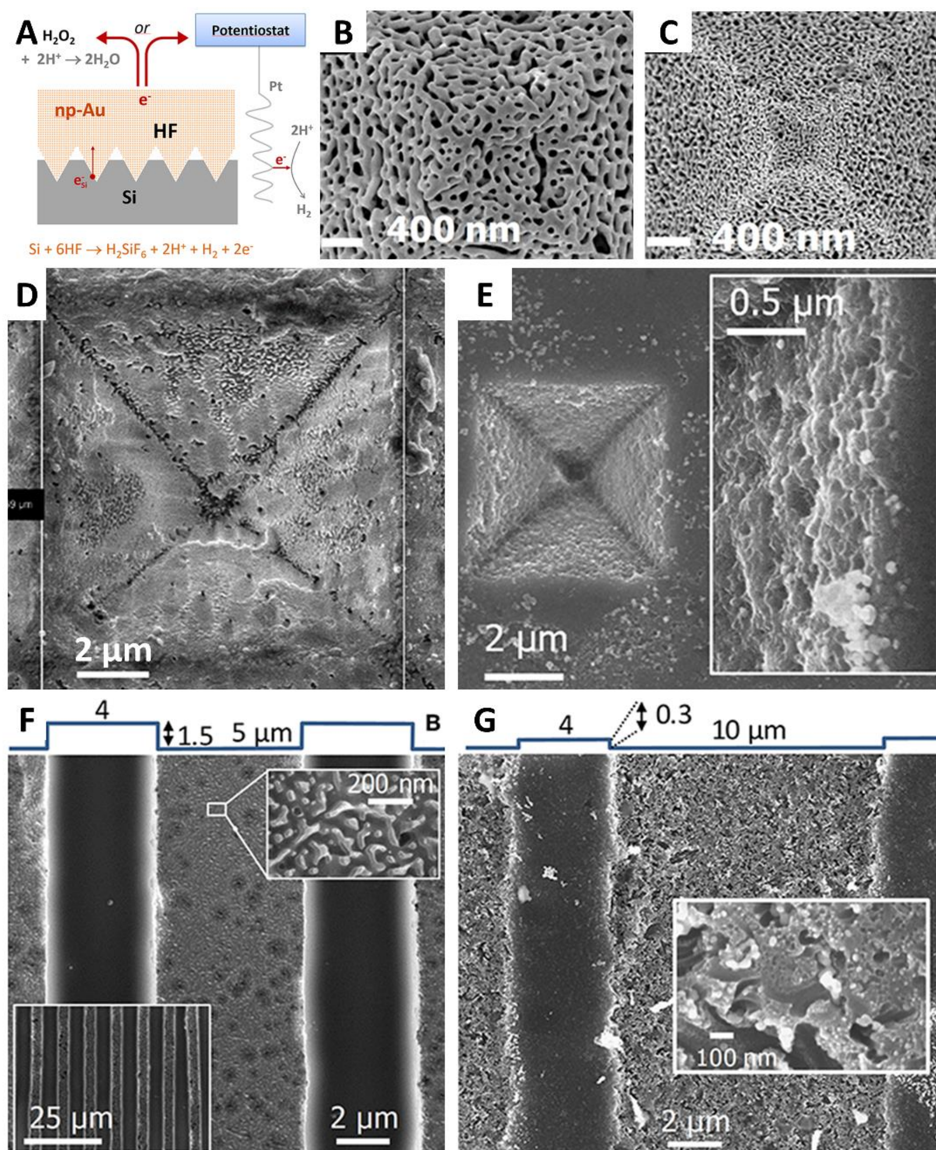

Figure 11. Results of the monocrystalline Si Mac-Imprint with nanoporous Au stamps. A – schematics of the Mac-Imprint setup. B and C – Top-down SEM images of coarse and fine nanoporous Au electrodes, respectively. D and E – Top-down SEM images of the inverted pyramids imprinted with coarse and fine electrodes, respectively. F and G – Top-down SEM images of the grooves imprinted with coarse and fine electrodes, respectively. Reproduced with the permission from *(23)*.

fraction (PVF) of the nanoporous catalysts on pattern transfer fidelity and the etching kinetics during Mac-Imprint. At first, the parabolic cylinders were successfully transferred

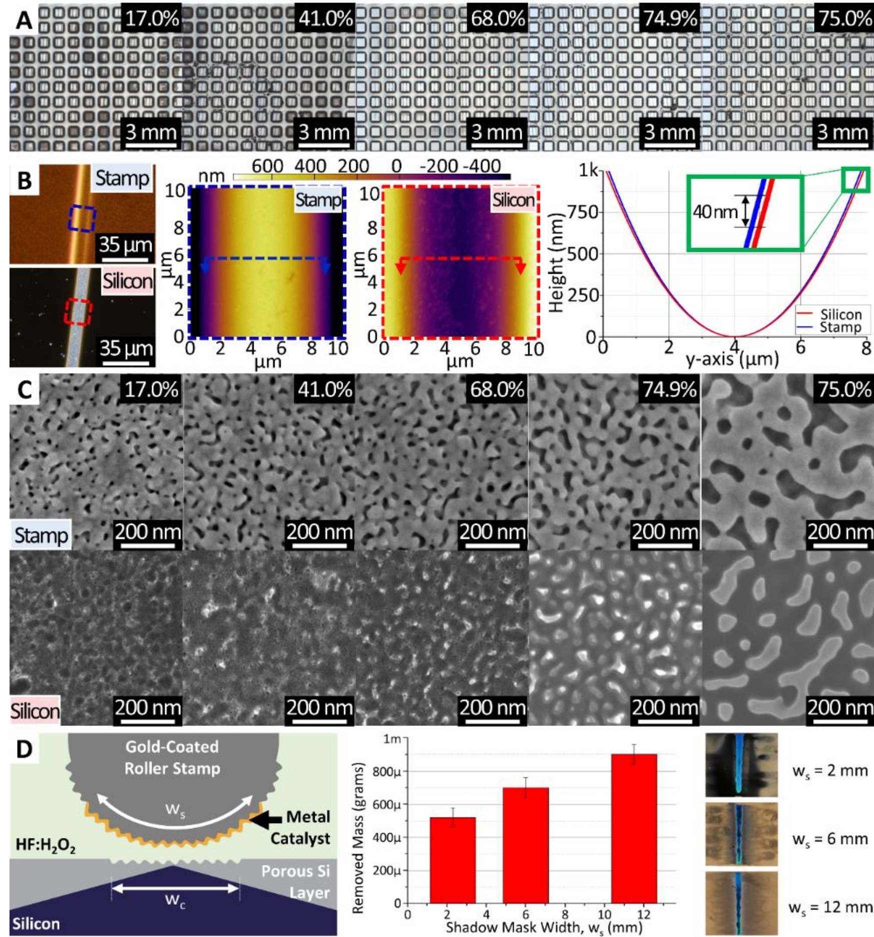

Figure 12. Results of the monocrystalline Si Mac-Imprint with nanoporous Au stamps. A – Top-down optical images of pillar arrays Mac-Imprinted with stamps with different PVF, denoted in the top right corner. B – Comarison between AFM scans of stamp and Si imprinted with PVF = 68% stamp. C – Top-down SEM images of the porous Au with different pore volume fractions (top row) and corresponding imprinted Si surface (bottom row). D – Influence of the catalyst surface area on the amount of the etched Si. Reproduced with permission from *(24)*.

onto the Si pillars for the whole range of studied PVF (Figure 12A) with high pattern transfer fidelity achieved at PVF = 68% (Figure 12B). Secondly, the direct positive correlation between stamp's pore size and imprinted Si surface roughness was established (Figure 12C). In addition, the porosification of the imprinted surface has been observed for

stamp's PVF of <68% (Figure 12C) and was explained by the insufficient mass-transport through undeveloped porous catalyst network that lead to the delocalization of the etching reaction. Moreover, it was established that the increase of the catalyst surface-to-contact area ratio scales the rate of H_2O_2 reduction which shifts it's balance with the anodic reaction of Si dissolution away from stoichiometry and results in etching delocalization and formation of porous Si (Figure 12D).

Despite recent advancements in the Mac-Imprint of monocrystalline Si described in the previous paragraphs several remaining challenges associated with mass-transport of the etching solution are restricting its application for fabrication of functional 3D optoelectronic devices and large-area 3D metasurfaces. In the next chapters this dissertation presents and discusses steps in understanding fundamental mechanisms behind Mac-Imprint and their effects on the fabrication of new generation of advanced stamps for major technique improvement.

2.8 Improvements to the Mac-Imprint System

Recently, an extensive work has been conducted aimed to improve the throughput and accuracy in Mac-Imprint of GaAs *(53, 54)* and these findings are also translatable onto Si. With respect to the Mac-Imprint throughput Meng et al. investigated the importance of the stamp-to-substrate alignment for the macroscopic uniformity of Mac-Imprint with up to 12 mm wide stamps *(53)*. Specifically, the Mac-Imprint system was modified with two elastic cushions being added underneath the GaAs substrate and above the stamp (Figure 13A) in order to self-balance and compensate for tip-and-tilt misalignments and the imprint results were compared to those of the unmodified system. It was demonstrated that

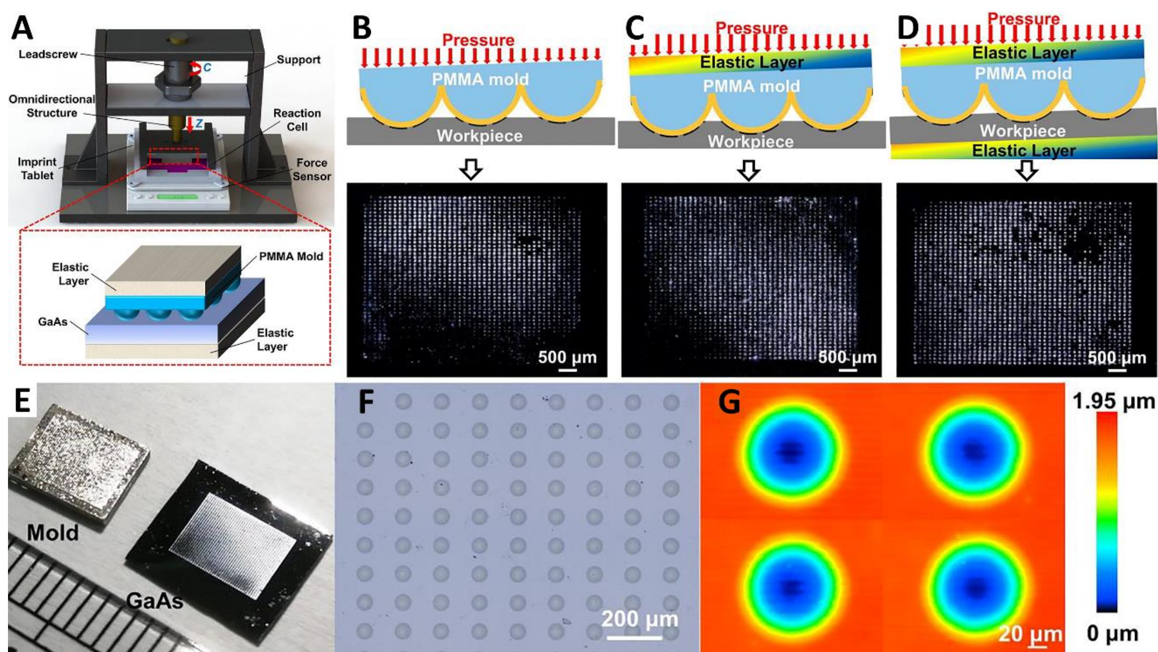

Figure 13. Modulation of the contact uniformity during Mac-Imprint. A – design of the Mac-Imprint system with double cushion for the compensation of misalignments. B-D – schematics and imprint results of unmodified system (B), single cushion system (C) and double-cushion system (D). E – Photograph of the Mac-Imprint stamp and imprinted GaAs substrate highlighting the macroscopic contact uniformity. F – Optical image of the imprinted microlens array. G – Depth profile of the microlenses imprinted in the four corners of the stamp. Reprinted with permission from *(53)*.

macroscopic contact uniformity with one elastic cushion was improved from 78.1% of total stamp area (i.e., unmodified Mac-Imprint system) to 85.3% with some tip-and-tilt misalignment still present (Figure 13B and C). The addition of another cushion underneath the GaAs lead to further improvements with 94.7% (Figure 13D and E) of the total stamp area being uniformly imprinted (Figure 13F) with high microscopic pattern transfer fidelity (Figure 13G).

The influence of the oxidant concentration on the cathodic potential of the catalytic stamp and it’s effect on the pattern transfer fidelity during Mac-Imprint of GaAs was

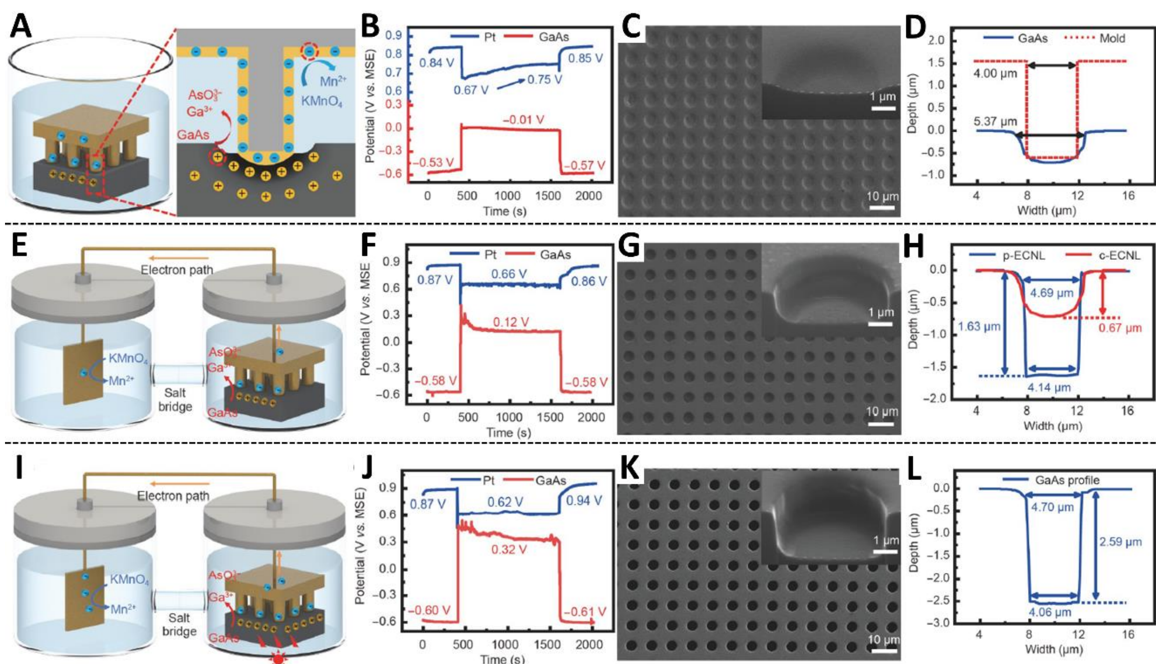

Figure 14. Mac-Imprint system improvements. A – Schematics of classical Mac-Imprint system. B – Potentials on the catalyst (blue) and GaAs (red) interface. C – SEM image of the imprinted surface. D – cross-sectional height profiles of the imprinted hole (blue) and stamp's pillar (red). E – Schematics of spatially-separated Mac-Imprint system. F – Potentials on the catalyst (blue) and GaAs (red) interface. G – SEM image of the imprinted surface. H – cross-sectional height profiles of the holes imprinted with spatially-separated (blue) and classical (red) Mac-Imprint. I – Schematics of spatially-separated phot-enhanced Mac-Imprint system. J – Potentials on the catalyst (blue) and GaAs (red) interface. K – SEM image of the imprinted surface. L – cross-sectional height profile of the imprinted hole. Reprinted with permission from *(54)*.

studied by Xu et al. *(54)*. Specifically, it was discussed that the depletion of the oxidant near the catalyst/GaAs interface in the classical Mac-Imprint setup (Figure 14A) leads to the decrease of the cathodic overpotential on the catalyst/electrolyte interface (Figure 14B). This effect slows down the rate of cathodic reaction leading to the disbalance of the anodic reaction of GaAs dissolution. Overall this results in the shallow etching (Figure 14C) with poor patter transfer fidelity (Figure 14D). In order to overcome this limitation an improved

Mac-Imprint system was developed in which the reduction reaction was spatially separated from the anodic reaction as is demonstrated on (Figure 14E). This approach allowed to stabilize the potential on the catalyst/electrolyte interface (Figure 14F) which lead to the ~2.5 times improvement of the etch depth (Figure 14H) as well as better confinement of the etching reaction (Figure 14G). The addition of the back illumination (Figure 14I) increased the rate of the anodic reaction (Figure 14J) which lead to the ~1.6 times deeper etching (Figure 14L) comparing to the non-illuminated spatially-separated Mac-Imprint setup. The confinement of the etching reaction was maintained similar to the pervious case (Figure 14K). It should be noted that while spatially-separated Mac-Imprint system helped to improve both etch depth and the confinement of the etching reaction, it also allowed to avoid substrate contamination with the byproducts oxidant reduction reaction. Both of these studies are presented to highlight the necessity for the improvement of the Mac-Imprint systems.

CHAPTER 3

ROUGHNESS SUPPRESSION IN ELECTROCHEMICAL NANOIMPRINTING OF SI FOR APPLICATIONS IN SILICON PHOTONICS

The results presented in this chapter have been largely reproduced form previously published work *(25)*.

Metal-assisted electrochemical nanoimprinting (Mac-Imprint) scales the fabrication of micro- and nanoscale 3D freeform geometries in silicon and holds the promise to enable novel chip-scale optics operating at the near-infrared spectrum. However, Mac-Imprint of silicon concomitantly generates mesoscale roughness (e.g., protrusion size ~ 45 nm) creating prohibitive levels of light scattering. This arises from the requirement to coat stamps with nanoporous gold catalyst that, while sustaining etchant diffusion, imprints its pores (e.g., d_{ave} ~ 42 nm) onto silicon. In this paper, roughness is reduced to sub-10 nm levels, which is in par with plasma etching, by decreasing pore size of the catalyst via dealloying in far-from equilibrium conditions. At this level, single-digit nanometric details such as grain boundary grooves of the catalyst are imprinted and attributed to the resolution limit of Mac-Imprint which is argued to be twice the Debye length (i.e., 1.7 nm) – a finding that broadly applies to metal-assisted chemical etching. Lastly, Mac-Imprint is employed to produce single-mode rib-waveguides on pre-patterned silicon-on-insulator wafers with RMS line edge roughness less than 10 nm while providing depth uniformity (i.e., 42.9 ± 5.5 nm), and limited levels of silicon defect formation (e.g., Raman peak shift <0.1 cm^{-1}) and sidewall scattering.

3.1 Introduction

Silicon photonics utilizes a variety of micro- and nanostructured waveguide and metamaterial-based components to enable applications such as optical interconnects within a chip, from chip-to-fiber and chip-to-chip *(55)*. However, the efficiency, performance, minimum feature size, and scalable manufacturing of chip-scale silicon photonic devices is presently constrained to 2D designs compatible with modern deep ultraviolet (DUV) or immersion lithography combined with reactive ion etching (RIE) *(56, 57)*. Introduction of 3D designs with grayscale or multi-level etch depths has been proposed to increase the performance and/or compactness of grating couplers *(58–60)*, edge couplers *(61)*, multi-mode waveguide bends *(3)*, waveguide crossings *(62)*, polarization convertors *(4)*, small-mode area waveguides *(63, 64)* and more. It also allows for the fabrication of advanced 3D photonic devices such as spoof surface plasmon structures *(1)*, chromatic-aberration corrected lenses, *(6)* and quasicrystal interferometers with physical unclonable functions *(65)*. However, such 3D structures are sensitive to depth and shape inaccuracy of plasma etching and have so far remained challenging to realize while maintaining the scalability requirements of the semiconductor industry.

Recent demonstrations of 3D or multi-level silicon photonic components have utilized multiple lithography and RIE steps to achieve multi-level etch depths *(58–60)*, or grayscale electron beam lithography (EBL) to achieve analog profiles *(3, 62)*. The former multi-step photolithography-based process inherently prohibits the independent and arbitrary control of lateral feature size and depth, while the latter EBL-based process is a direct writing technique and is not a scalable manufacturing solution. Both processes also

require precise control over RIE selectivity, etching rate, and time to achieve the precisely desired silicon micro- or nanostructure dimensions. This challenging task is further complicated by loading effects and aspect-ratio dependent etch rates *(10, 11)*. Alternatively, the independent control of feature size and depth can be attained using direct parallel nanofabrication methods such as nanoimprint lithography of inorganic materials, which can either (i) mechanically pattern molten or porosified substrates *(66, 67)*, or (ii) electrochemically carve it via metal-assisted electrochemical nanoimprinting (Mac-Imprint) *(20, 21, 26)*. The former two approaches are unable to pattern SOI wafers and retain its solid and single-crystalline SOI characteristics. Mac-Imprint by-passes this issue by catalyzing the corrosion of silicon at the contact points between itself and a noble-metal coated stamp in the presence of hydrofluoric acid and an oxidizer (Figure 15A) *(20, 24)* whose detailed mechanism has been explained in existing literature on metal-assisted chemical etching (MACE) that is focused on thin-film catalysts directly deposited onto silicon *(22, 31, 33)*. Unlike MACE, in which the noble metal catalyst is not reusable and it's motion governed by the crystallography orientation of Si and etching conditions *(41, 45)*, Mac-Imprint by-passes these issues as the noble-metal catalyst is mechanically attached to the stamp and is retrieved upon each imprint cycle. At the same time, it introduces demolding issues such as delamination particularly prominent in high-aspect ratio structures (>1).

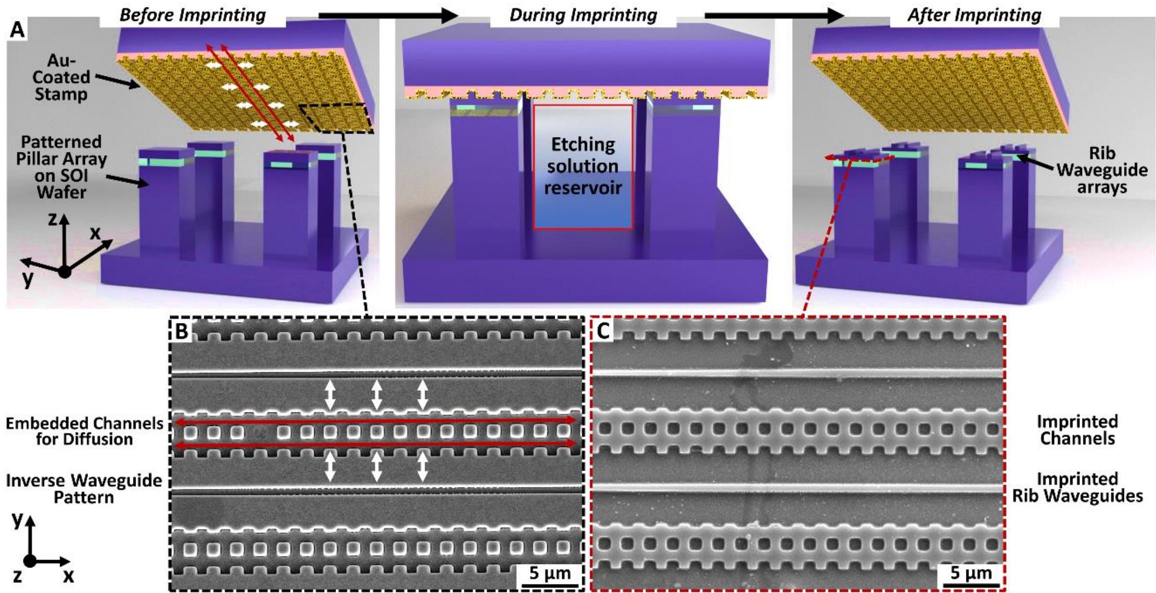

Figure 15. A – Schematics of the catalytic stamp and patterned SOI wafer interaction during Mac-Imprint; B and C – Top-down SEM images of catalytic stamp and Si rib waveguide patterns respectively. The coordinate systems indicate the parallel (x), perpendicular (y) and vertical (z) directions relative to the principal axis of the waveguide. Arrows highlight the solution diffusion pathways: red - through the embedded channels towards the center of the SOI pillar, and white – through the catalyst in-between embedded channels and waveguide patterns.

High pattern transfer fidelity during Mac-Imprint of monocrystalline Si (Figure 15, B and C) requires mass-transport of reactants through a nanoporous gold (np-Au) catalyst *(23, 24)* because solid catalysts cannot provide sufficient diffusion on length scales larger than 0.5 µm if Si is to be etched without concomitant porosification *(34)*. At the same time, the catalyst pore size (e.g., d_{ave} ~ 42 nm in Sharstniou et al. *(24)*) is accurately transferred onto the bottom and sidewalls of the imprinted surface which increases bottom and line edge roughness (LER) of imprinted structures (i.e., ~ 49 nm *(24)*) and induces prohibitive levels of scattering losses in waveguides *(16)*. Conventional RIE machined waveguides

have an as-machined roughness of 10 nm that can be smoothened in post-processing down to 2 nm *(17)*.

With the goal of prototyping functional silicon rib waveguides using Mac-Imprint of SOI wafers, this paper elucidates the mechanism by which roughness is generated and suppresses it by reducing the pore size of the catalyst to sub-10 nm levels. The latter is attained via the synthesis of np-Au in far-from-equilibrium conditions using established process-structure relationships for dealloying *(68)*. Bottom roughness surrounding the waveguide and its LER are reduced to less than 10 nm which represents a 75 % improvement relative to prior work *(24)*. At the lowest roughness levels, the grain boundary grooves of the np-Au are discernable on the surface of the imprinted Si and is a major contributor to it. This observation is discussed in the context of the resolution limit of Mac-Imprint and MACE which was first hypothesized by Sugita et al. *(28)* to be proportional to the Debye length present at the metal-solution interface. Albeit never experimentally confirmed, a new analysis of previous work on MACE with ultra-fine gold nanoparticles reported by Liu et al. *(29)* along with experimental data presented in this work strongly support Sugita's hypothesis to be true. This finding directly applies to both Mac-Imprint and MACE as they share the same fundamental mechanisms. Additionally, the influence of the solution diffusion supported by the porous catalyst on Mac-Imprint's patterning fidelity is presented in comparison to its solid counterpart. The reduced pore sizes of the catalyst increase the cathodic reaction rate *(24)* which is compensated by increasing the Chartier-Bastide parameter (known as 'ρ' in literature *(31)*) to 99.5% yielding Si waveguides with limited levels of defect formation as characterized by Raman

spectroscopy. Finally, the optical characterization of nanoimprinted rib waveguides (i) confirms the single mode light propagation which matches electromagnetic simulations, and (ii) IR imaging reveals no significant levels of light scattering from its walls.

3.2 Results and Discussion

Mac-Imprint of Si waveguides onto the SOI pillars requires diffusion of reactants and byproducts over a large (e.g., >75 µm) and a heterogeneous pathway. This path extends from the edge of the pillar where reactants are stored in the solution reservoir confined around the pillar and towards its center (Figure 15, A and B) and consists of embedded channels in the stamp parallel (i.e., x-direction) to the waveguide's principal axis (red arrows on Figure 15, A and B) that are formed in the gaps between stamp and substrate upon their contact. Additionally, the solution must diffuse in the perpendicular direction (i.e., y-direction) between the waveguide and the embedded channels through the catalytic film (white arrows on Figure 15, A and B) for a total distance of 3 µm. Note that the scenario in which diffusion takes place through a porosified silicon layer *(24)* is detrimental to the waveguide's performance as it can create refractive index spatial variations. When both pathways support enough etching solution diffusion, the pattern from the stamp is accurately transferred onto Si without porous defects (Figure 15C).

3.2.1 Limiting Diffusional Pathways

In order to evidence the role of the catalyst film's porosity on supporting diffusion of the etching solution, pre-patterned SOI chips were Mac-Imprinted with stamps coated with thin-films of solid Au (Figure 16, A and B) and porous Au (Figure 16, C and D).

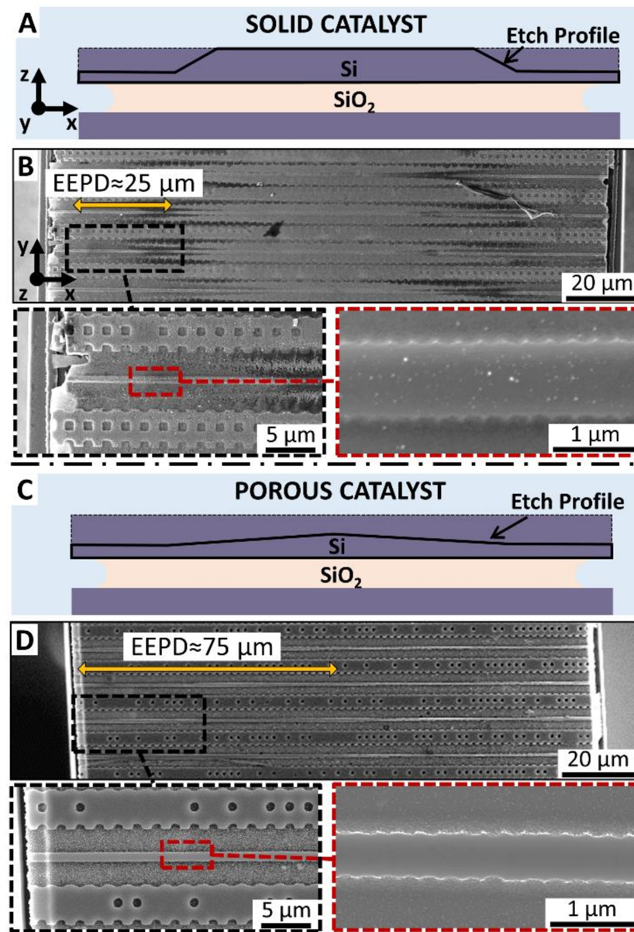

Figure 16. A and B – Schematic cross-section and top-down SEM images respectively of waveguide arrays imrinting with solid Au catalyst. Inset in B highlights the beginning of porous silicon formation region. C and D – Schematic cross-section and top-down SEM images respectively of the waveguide arrays imprinting with porous Au catalyst. Solid yellow arrows indicate the length of the region with distinguishable waveguide pattern (EEPD).

Pillars imprinted with solid Au stamps yielded waveguide patterns near its edges with distinguishable profile and depth (Figure 16B). However, the pattern becomes shallower and loses contrast in the SEM images as it approaches the center of the pillar. The average distance from the edge of the pillar to the end of the distinguishable waveguide pattern is indicated by solid yellow arrows in Figure 16, B and D and termed as the effective etching

penetration distance (EEPD). At the end of the EEPD, not only patterns become indistinguishable, but SEM images reveal the formation of porous silicon defects (dark areas in Figure 16B). Note, that periodic grating with the period of 273 ± 8 nm and heights of 82 ± 10 nm could be observed on high magnification SEM image (Figure 16B) along the edge of the waveguide. The geometry of this grating mimics the one of original Si master mold highlighting the resolution capability of Mac-Imprint.

In contrast, pillars imprinted with porous Au stamps (Figure 16D) yielded an EEPD value that is maximum, and, thus, the entire half-width of the SOI pillar was successfully imprinted with the waveguide's pattern without any observable defect (e.g., porous silicon) formation. Note, the periodic grating with the period of 255 ± 2 nm and heights of 64 ± 7 nm is also observed in the case of Mac-Imprint with np-Au (Figure 16D). In order to understand the EEPD limitation of Si waveguide Mac-Imprinting with porous catalysts a blank SOI wafer was imprinted as the etching solution diffusion in the parallel direction could only happen from the edges of the stamp (Figure 17A). The photograph of the imprinted SOI chip demonstrates bright stripes forming a rectangle in it's center (Figure 17B) which represent the waveguide pattern imprinted on the periphery of the macroscopic stamp/SOI contact interface. The close inspection of the edge of the contact interface perpendicular to the direction of waveguide's propagation indeed reveals the arrays of waveguides accurately imprinted over the distance of about 700 µm making it the largest achieved EEPD. These findings suggest that the porous catalyst and embedded channels cannot support etching solution diffusion beyond that length scale.

Figure 17. Analysis of the EEPD limitation. A – Schematics of the Mac-Imprint onto the blank SOI chip. B – Photograph of the Mac-Imprinted SOI chip. C – Optical image of the edge of imprinted area highlighting the EEPD.

In contrast to the imprint results with the solid catalyst (Figure 16, A-B), the addition of the thin porous catalyst represents a small increase in the cross-sectional area available for free-solution diffusion in the parallel direction (x-direction) and, thus, the effective diffusion constant is expected to be marginally altered. However, the effective diffusion constant along the perpendicular direction (y-direction) has been increased by orders of magnitude in comparison to the case of the solid catalyst. That is because the diffusion in the solid catalyst is supported through the grain boundaries which support a diffusional regime known as molecular sieving with an effective diffusion constant that is orders of magnitude lower than the diffusion in free solution *(24)*. Meanwhile, the porous catalyst has pore sizes ranging from 10-42 nm which are much larger than the electric double layer thickness which is approximately 8.6 Å (for detailed calculations, see APPENDIX A), and can support free solution diffusion *(69)* with simple corrections for tortuosity *(70, 71)*. Note that the thickness of the precursor film was selected to be much larger (e.g. 9 times) than the catalyst's pore size (i.e., 42 nm) to sustain diffusion through a well-developed 3D pore network without any optimization in its selection. A 'digital

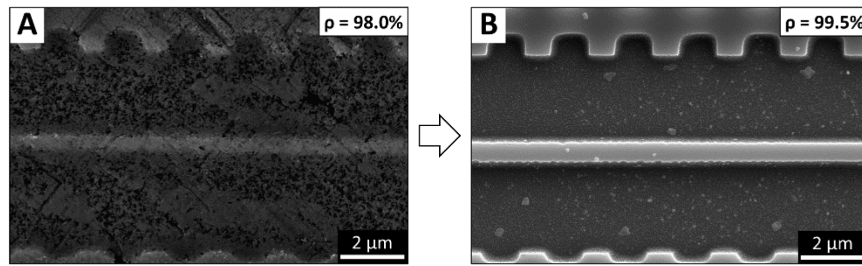

Figure 18. Adjustment of the etching solution to compensate for the increasing catalyst surface area. A – SEM image of the waveguide imprinted with porous catalyst at ρ = 98.0 %. B – SEM image of the waveguide imprinted with porous catalyst at ρ = 99.5 %.

twin' model that captures both reaction rate and diffusional transport for Mac-Imprint with thinner catalysts is likely needed in the future to address such design questions. Instead, in this paper, the catalyst's high-surface area and its increased cathodic reaction rate is compensated by increasing the Chartier-Bastide parameter (known as 'ρ' in literature *(31)*) to 99.5% until porous silicon formation is suppressed (Figure 18) as was confirmed by Raman spectroscopy. Alternatively, the use of a counter electrode in solution biased against the gold catalyst as in prior works of Torralba et al. *(26)* and Kim et al. *(72)* is recommended as it does not require hydrogen peroxide and the reaction rate can be externally controlled via biasing.

In addition to the role of diffusion mechanisms, the results for the solid catalyst case such as the short EEPD, the non-uniform etch depth and the porous silicon formation (Figure 16, A-B) cannot be fully understood unless one considers the kinetics of the etching reaction during metal-assisted chemical etching (MACE). At first, oxidant is reduced on the surface of a noble metal (cathodic reaction), which results in the generation of positive charge carriers (holes) in Si *(31)*. Then, the holes are injected into Si through noble metal/Si Schottky junction and subsequently consumed during Si dissolution (anodic reaction) *(31)*.

Thus, whenever the diffusion of reactants towards the catalyst/Si contact interface is not sufficient, instead of confined etching under the catalyst, the porosification of silicon takes place around the catalyst/Si/etching solution triple junction in both conventional MACE as well as in Mac-Imprint *(20, 24, 34)*. This is expected to take place in the case of Mac-Imprint with solid catalyst since the mass-transport for the etching solution in the perpendicular direction (i.e., labeled as "2" in Figure 19A) is constricted. Thus, the holes injected into Si at its junction with the catalyst (i.e., step labeled as "1" in Figure 19A) can diffuse through the substrate to the interface between the etching solution and Si (i.e., step labeled as "3"). Once holes reach the etching solution/Si interface they induce its porosification (step labeled as "4"). Upon the growth of a porous silicon layer underneath the catalyst, the anisotropic etching of silicon can take place since etching solution can now reach the catalyst/Si interface. This mechanism can explain the concomitant observation of anisotropically etched features (i.e. waveguide geometry) near the edges of the Si pillar (Figure 16B) and the porosification of the silicon surface observed in Figure 19C. Note that porous silicon is observed both in the regions surrounding the waveguide as well as in itself.

Ultimately, the uncontrollable porosification process is more pronounced on the edge of the pillar due to the abundant supply of reactants and is followed by its fast depletion in the embedded channel resulting in shallow etching depths in the center of the pillar which defines the EEPD distance. These findings highlight the fundamental limitation of solid catalyst since it cannot support the perpendicular diffusion for anisotropic imprinting of the designed 3 μm wide features, which is consistent with MACE

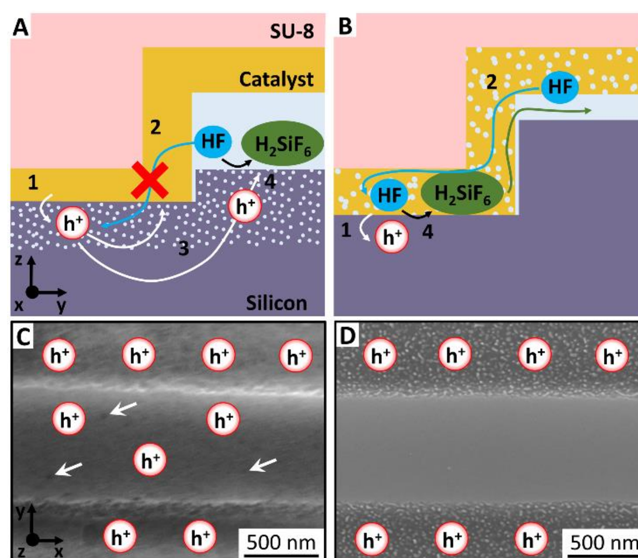

Figure 19. A and B – Schematics of charge- and mass-transport processes. C and D – High-magnification top-down SEM images of the individual waveguides. Holes are added to illustrate the charge carrier distribution around catalyst/Si interface. White arrows point to the visible pores. A, C and B, D correspond to Mac-Imprint with solid and porous catalysts, respectively.

literature on thin-film catalyst formats *(34, 35, 48)*. In recent literature of Si Mac-Imprint with solid catalysts, this issue was by-passed by designing stamps with an array of widely spaced patterns that simultaneously provided space for solution storage and were narrow enough (<520 nm) to sustain diffusion through the grain boundaries of catalyst or a porous layer underneath it *(52)*. Despite enabling diffusion, the nanoporous catalyst has higher specific surface area compared to its solid counterpart. This will inevitably increase the rate of H2O2 reduction and, as a result, lead to Si porosification *(24)*. Thus, this work implemented a reduction of the H_2O_2 concentration relative to the literature in MACE based on thin-films *(31)* and increase in ρ value to 99.5% to minimize this effect and yield solid waveguides in Figure 19D. It should be noted that the cathodic reaction can be spatially-separated from the anodic reaction *(54)* with a counter electrode placed in solution

polarized against the gold catalyst with or without a salt bridge *(26)* which guarantees that diffusion and solution storage limitations associated with H_2O_2 and its reaction products can be eliminated *(54)*.

In order to qualify the imprint results, the waveguide's cross-section depth profiles were extracted via AFM (Figure 20A) and analyzed. Its average depth was 42.9 ± 5.5 nm (Figure 20B) with a maximum of 60 nm at the edge and a minimum of 29.7 nm at approximately 20 µm from the edge. The maximum depth is closer to the edge of the pillar (Figure 20B) which could be explained by (a) the non-flatness of the stamp resulting from molding issues, (b) the proximity to the solution storage reservoir resulting in a faster etching, and (c) the bending of the stamp due to contact forces. A gradual reduction of the depth profile as a function of the distance from its edge (i.e., horizontal axis in Figure 20B) is consistent with abovementioned scenarios "b" and "c". However, given the random nature of the depth profile (Figure 20B), the stamp's non-flatness (i.e., scenario "a") is the most consistent explanation. In fact, stamps were prepared by UV NIL of spin-coated SU-8 resist with soft PDMS-based molds (as described in the Experimental Section) which is known to introduce pattern distortions during demolding operation such as rimming *(73–75)* which is a protrusion of the pattern's edges similar to the inverse of the silicon pattern observed in the inset of Figure 20B. Thus, the depth profile in Figure 20B is irregular since Mac-Imprint imprints the distorted geometry of the mold with high fidelity. This hypothesis was further confirmed in the additional experiment where AFM scans of imprinted SOI pillar and Mac-Imprint stamp were acquired at complimentary locations and are indeed mirror images of each other (See Figure 42 in the APPENDIX A). Note that the

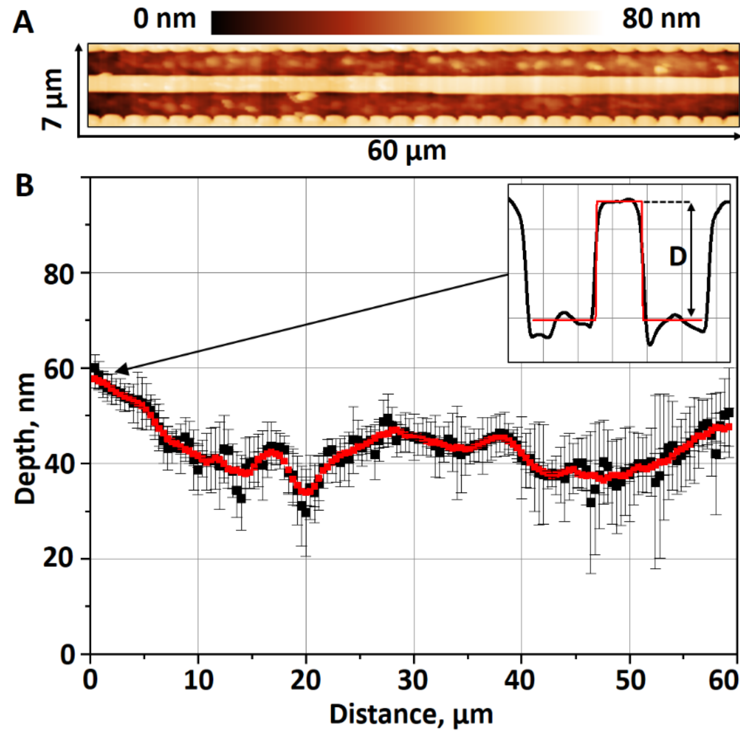

Figure 20. Depth analysis of imprinted waveguide with uniform depth showing (A) large area AFM scan of a single waveguide from the edge (left) to the center (right) of the SOI pillar, and (B) waveguide's depth profile (black squares) and 3 point moving average (red squares) with inset highlighting one of the waveguide's cross-section and depth measurement (label D). The bottom sub-20 nm roughness of the waveguide surroundings induced by the catalyst cannot be detected due to the low resolution of the large-area AFM scan shown in (A). Data represents depth extracted through fitting of step-height function with error bar representing fitting error.

large and low-resolution AFM scan in Figure 20A does not provide enough resolution (see details in the Experimental Section) to capture the porous gold morphology imprinted onto silicon.

3.2.2 Roughness Reduction and Its Fundamental Limits

Mac-Imprint introduces bottom and sidewall roughness which originates from its resolution limit (i.e., minimum discernible positive feature) being smaller than the pore diameter of the catalyst and results in the accurate transfer of the catalyst's nanopores onto the imprinted surface *(23, 24)*. Thus, with the goal to address the roughness issue, it becomes necessary to find a theoretical basis to Mac-Imprint's resolution limit. In 2011, Sugita et al. *(28)* first interpreted the band bending in silicon around the electrolyte-silicon-metal triple junction in the context of anodic electrochemical machining of silicon. Based on the work of Nakato et al. *(76)*, Sugita et al. proposed that the strong electric field developed in the electrical double layer at electrolyte-metal interface (represented by dashed black lines on Figure 21A) induces the bending of the isopotential lines in silicon near the electrolyte-silicon-metal junction (represented by solid black lines in Figure 21A). This should lead to the migration of holes in silicon away from the triple junction to a distance proportional to the Debye length (highlighted by black arrow in Figure 21A). If this theoretical basis is correct, it would result in silicon features being overetched by a lateral distance, φ, that is proportional to the Debye length (Figure 21B) which has not been experimentally verified in literature. While Sugita et al. worked with feature sizes ranging from 10-100 μm, recent experimental work on MACE by Liu et al. yielded sub-5nm features *(29)*. Using data from Liu et al. *(29)*, it is possible to calculate the average overetched distance (i.e., φ_1 in Figure 21D), which is the difference between catalyst

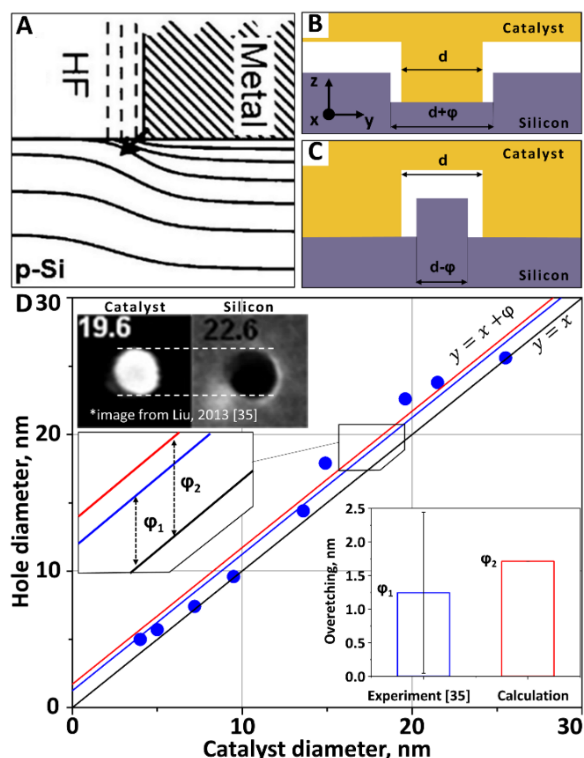

Figure 21. Theoretical model for band bending during anodic electrochemical machining of Si proposed by Sugita et al. Dashed lines at metal-solution interface represent isopotentials within the electrical double layer (Debye length) and solid lines represent isopotentials bending around the triple junction. Reprinted (adapted) with permission *(28)*. Copyright 2011 American Chemical Society. B and C – schematics of the overetching for the negative and positive Si features, respectively (not to scale). D – plot of silicon hole versus catalyst diameter using imported data from Liu et al. *(29)* Three lines with a unity slope are plotted with different offsets: zero (black - reference), best fit of experimental data (blue, φ_1) and two times the Debye length (red, φ_2). ϕ_1 on the bar plot is reported as average ± standard deviation based on 9 reported measurements. The upper inset contains top-down SEM images of the metal catalyst and the resulting hole in Silicon. The inset images and data are reprinted (adapted) with permission *(29)*. Copyright 2013 American Chemical Society.

diameter and silicon hole diameter and equals to 1.24 nm. This value closely matches two times the theoretical value of the Debye length (φ_2 in Figure 21D) which is 1.71 nm (see

calculations in APPENDIX A). Note that the large standard deviation of φ_1 (i.e., ±1.2 nm, details in the Supporting Table 2) could be attributed to (i) errors of the measurement technique associated with limited resolution or (ii) catalyst particle size distribution if catalyst and hole widths are not measured in complementary locations *(77)*.

Next, this work attempts to eliminate roughness by designing catalyst films whose pore sizes approach the Debye length to within at least an order of magnitude (Figure 21C). This was accomplished by using previously established process-structure relationship in the electroless dealloying of $Au_{49}Ag_{51}$ thin-films at far-from-equilibrium from literature which allows for ligament control between 25 and 64 nm *(68)*. By reproducing it and further reducing the dealloying time and temperature (for additional details, see Methods), catalyst films with average pore diameters of 42, 27, 14 and 10 nm were fabricated (Figure 22, A-D) and used to Mac-Imprint arrays of linear rib waveguide structures (Figure 22, E-H). Additionally, albeit pores on Figure 22C and D appear isolated, a developed porous network structure is still formed throughout the thickness of the catalytic films which was confirmed by high-magnification cross-sectional SEM images (see Figure 44 in APPENDIX A). The impact of the pore size of the catalyst on the surface roughening during Mac-Imprint was established through the SEM analysis of imprinted linear rib waveguide structures. Overall, the catalyst size downscaling to 10 nm reduced the Si protrusion size linearly (Figure 22I) from 45 nm (Figure 22E) to 10 nm (Figure 22H). In the latter case, it was observed that the grain boundary grooves of the catalyst are also transferred onto silicon which limits further reductions in its roughness.

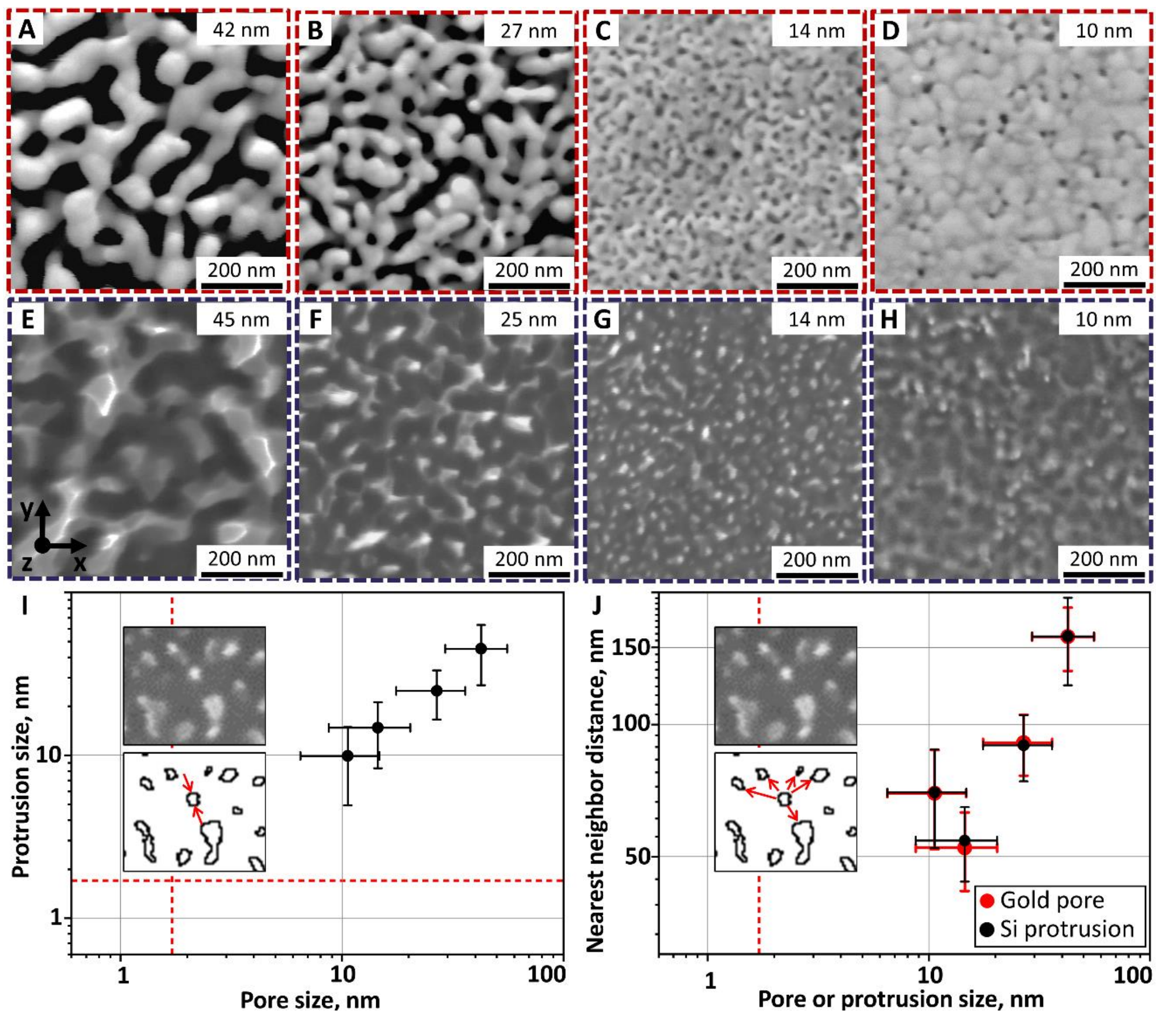

Figure 22. Top-down SEM images of the catalytic stamps with different average pore diameters (A-D) and imprinted waveguide surroundings (E-H). The boxes in the top right corner of the SEM images contain the average pore (A-D) and protrusion (E-H) diameters. Dependence of Si protrusion size on the catalyst pore size (I). Inset on I illustrate how the feature size (either pore or protrusion) was calculated. Dependence of nearest neighbor distance on the catalyst pore size and Si protrusion size (J, red and black, respectively). Inset on J illustrate how the nearest neighbor distance was calculated. Data is reported as average ± standard deviation. Red dashed lines on I and J indicate the resolution limit (i.e. double the Debye length).

In context to existing literature, Bastide et al. *(23)* and Sharstniou et al. *(24)* each attempted to reduce the catalyst pore size and roughness, but, at least in qualitative terms,

their work did not reduce either the silicon protrusion size or roughness due to stamp defects (e.g., cracks, delaminated catalyst) transferred during imprinting and concomitant substrate porosification. In their works, the smallest distinguishable average Si protrusion size without indication of porosification was approximately 31 nm and 27 nm *(23, 24)*. Finally, according to the nearest neighbor analysis (for details, see Experimental Section) the average distance between nearest neighbor pores in the catalyst matches that of the Si protrusions (Figure 22J, red and black dots, respectively). Note that there is an increase of the nearest neighbor distance in the case of the smallest catalyst pore size (i.e., 10 nm) which is attributed to incomplete Ag removal during dealloying which is known to produce lower pore surface area coverage and, thus, increases the interpore distances *(68)*.

Since the smallest pore size attained via electroless dealloying in this paper is still 5-6 times larger than the theoretical value for twice the Debye length, further reduction in the Si protrusion size is theoretically possible albeit the synthesis of catalysts with sub-10 nm average pore size becomes the limiting factor. In the literature of nanoporous gold synthesis through dealloying, the electroless and electrochemical dealloying methods have demonstrated the smallest pore size of approximately 5 nm by either reducing its temperature (e.g., -20 °C) *(78)* or inhibiting gold adatom surface diffusion *(79, 80)*. It was also shown that during dealloying ligament and pore size are inversely proportional to the melting temperature of host metal *(81)* suggesting that higher melting temperature metal or alloys catalysts suitable for MACE, such as platinum, could be potential candidates to further reduce pore size into the sub-5 nm domain *(32, 48, 82)*. It should also be noted that, to promote smoothening of the nanoimprinted surfaces, the Debye layer thickness can be

increased to approach the catalyst's pore size by (i) heating the etching solution and (ii) decreasing its ionic strength. The first approach would increase Debye layer thickness by ~1 Å given the low boiling point of the solution. The second approach can be achieved by reducing its concentration or by using solutes with a weaker dissociation constant both of which would reduce etch rates dramatically. These strategies should motivate future work to either eliminate the roughness or to improve the resolution limit of Mac-Imprint or MACE.

Although the bottom roughness of the waveguide surroundings may interfere with the guided electromagnetic wave, most of the propagation losses occur due to light scattering on the sidewall roughness of the waveguide. In Mac-Imprint, it is generated by the tangential movement of the np-Au surface parallel to the vertical direction of the Si sidewalls as the etching progresses, leaving 'scratch' marks along it. Thus, in theory, the flatter and less rough the porous Au surface is, the smoother the sidewalls should become. To verify this hypothesis, the LER of the imprinted waveguides was measured at its top as a function of the pore size of the catalyst according to the procedure described in the Methods. Figure 23E shows that, with the reduction of the pore size of the catalyst from 42 nm to 10 nm, the LER non-linearly decreases from 48 nm (Figure 23A) to 10 nm (Figure 23D), which is comparable with values reported for plasma-based micromachined silicon waveguides without post-processing strategies for smoothening *(17, 83)*. The smallest LER in silicon features achievable by Mac-Imprint would be inherently limited by the LER of the stamp's pattern coated with solid gold which was measured to be ~7.5 nm (Figure 23E, yellow dashed line) and is attributed to the roughness of gold thin-film and imperfections

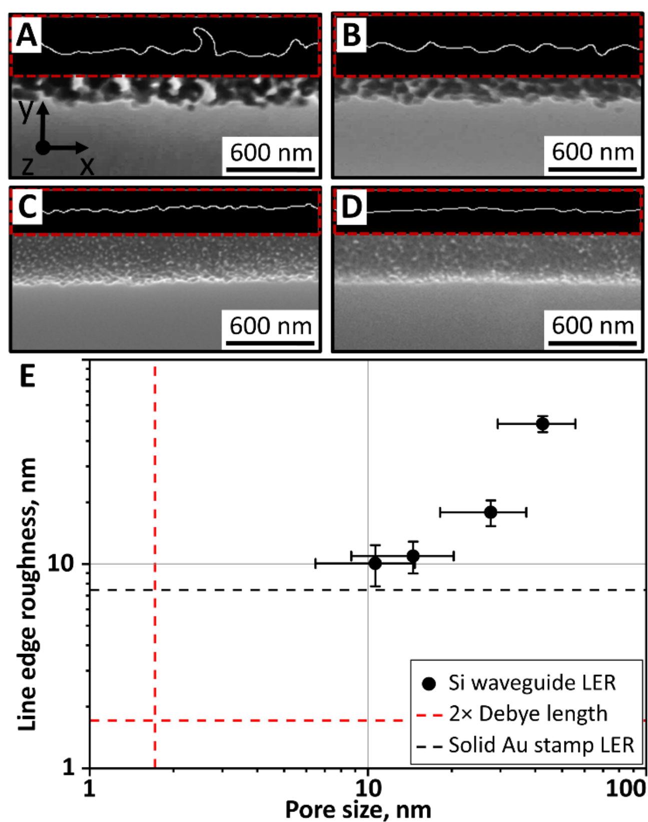

Figure 23. Top-down SEM images and edge profiles (framed with red dashed lines) of the waveguides, imprinted with porous catalysts with average pore sizes 42-10 nm respectively. E – Waveguide line edge roughness as a function of catalyst pores size. Data is reported as average ± standard deviation. Dashed lines indicate twice the Debye length (red) and solid Au stamp sidewall LER (black).

from soft-lithography steps used to fabricate the stamp. Thus, the improvements in sidewall roughness tend to saturate for pore sizes approaching 7.5-10 nm (Figure 23E) limiting further improvements. It is worth noting that, at the magnification and the pixel size of the analyzed SEM images which are 30 000x and 6.7 nm respectively, it might also limit measurement of further improvements at sub-10 nm pore sizes and require the use of alternate metrology techniques.

The minimization of LER to sub-10 nm is expected to have a positive impact on the minimum line-width resolution (MLWR) of Mac-Imprint. Albeit never experimentally determined, a reasonable criteria to estimate the minimum line-width resolution (MLWR) of a process is to use a 6-sigma approach based on sidewall LER (see Figure 43 in APPENDIX A). According to this assumption, the reduction of the LER achieved with np-Au's pore size of 10 nm would translate to MLWR values of approximately 60 nm which is a significant improvement comparing to the state-of-the-art whose largest pore size of np-Au used was 42 nm *(24)*.

3.2.3 Nanoscopic Defect Analysis

It is important to mention that the reduction of the catalyst pore size through the far-from-equilibrium dealloying leads to the incomplete removal of silver that can negatively affect Mac-Imprint process. In particular, in contrast to gold, silver (i) induces changes to the energy band bending in silicon near catalyst/Si interface due its lower work function, which affects hole injection and transport in Si and induces its porosification *(32, 84)* and (ii) is prone to dissolution and subsequent re-deposition *(85, 86)*. Despite catalysts with the smallest pore size being made with the shortest dealloying time, the large residual silver content of up to 42 at.% did not appear to induce porosification as evidenced by the SEM or optical microscopy. However, the porosification of Si could be happening in nanoscale form that would be challenging to detect using these techniques.

The analysis of the such defects during Mac-Imprint was accomplished by Raman spectroscopy, which has been extensively used in literature to characterize defects in silicon such as lattice strains *(87)*, microporosity (i.e., sub-2 nm) and mesoporosity (i.e., 2-

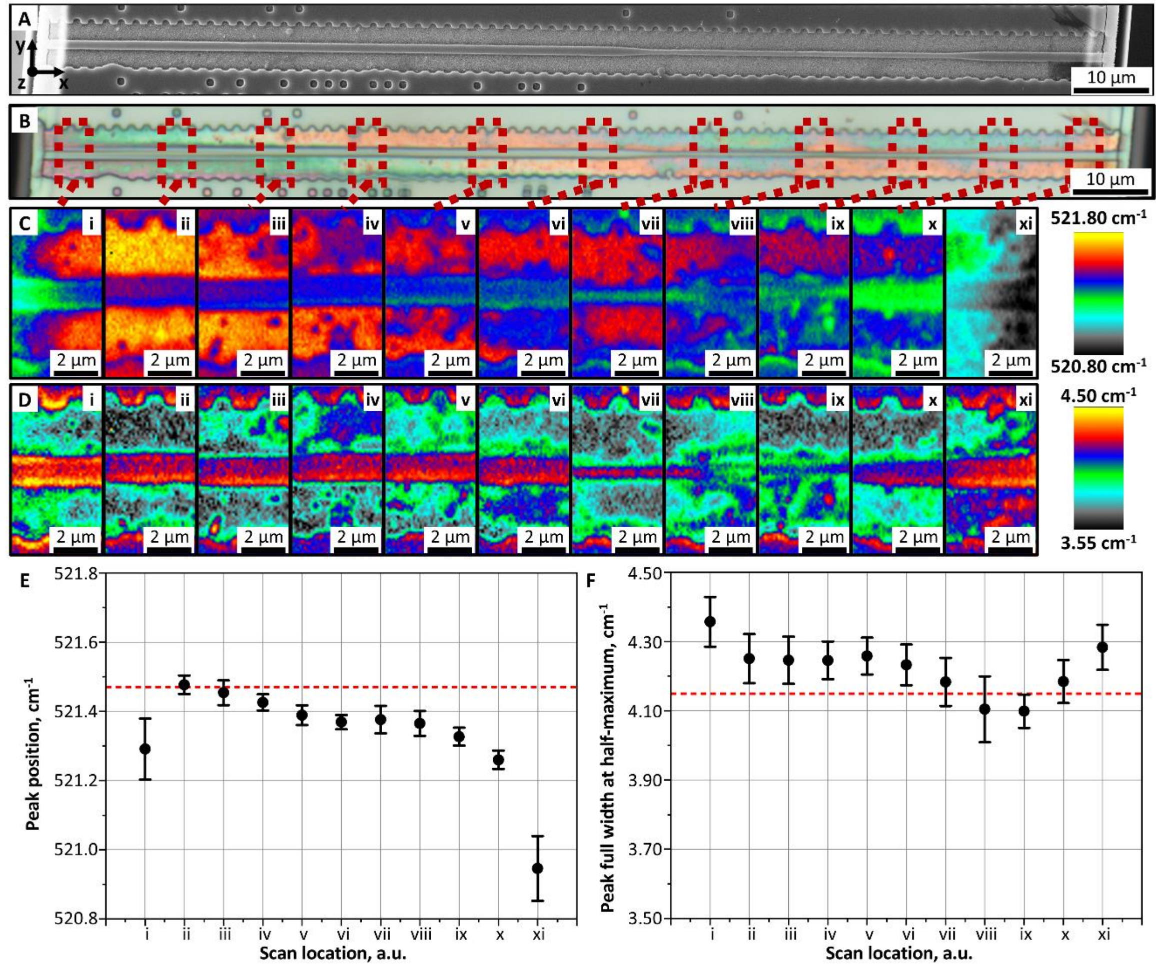

Figure 24. A and B – Top-down SEM and optical images of a single imprinted waveguide respectively. C and D – Maps of Raman signal peak position and full width at half-maximum respectively, taken at locations marked on B. E and F – Average values for Raman peak position and full width at half-maximum, respectively, of the waveguide at location marked on B. Data is reported as average ± standard deviation. Red dashed lines on E and F highlight the Raman peak position and full width at half maximum of the blank SOI wafer.

50 nm) *(88)* and amorphous regions *(89)*. The imprinted waveguide, presented on Figure 24, A and B, exhibited average peak position and full width at half-maximum (FWHM) of ~521.38 ± 0.07 cm^{-1} and ~4.20 ± 0.06 cm^{-1} respectively (Figure 24, C and D) throughout the center section of the waveguide excluding 6 µm away from each edge. At each of the

edges, a 0.09 cm^{-1} and 0.44 cm^{-1} shift to lower frequencies, and a 0.16 cm^{-1} and 0.08 cm^{-1} broadening of the Raman signal was observed (see locations i and xi in Figure 24, E-F). These edge effects are attributed to the release of the residual stresses and strains in the Si device layer by the undercut (Figure 16A) of the buried oxide layer during Mac-Imprint, as seen on Figure 24A and B near the edges of the SOI pillar. In fact, SOI processing is well known to introduce strains in the Si device layer which causes Raman peak to shift by $\pm$ 0.4 cm^{-1} from its mean position *(90)*. In our case, the blank SOI wafer had a peak position and FWHM of 521.47 $\pm$ 0.02 cm^{-1} and 4.15 $\pm$ 0.04 cm^{-1}, respectively. With regards to it, the average peak position at the center of the waveguide shifts and broadens by approximately 0.2 cm^{-1} and 0.1 cm^{-1}, respectively which is smaller than the expected values for microporous silicon (i.e., both approximately 1 cm^{-1} for crystallite sizes of < 5 nm *(88)*). Note that, in locations viii and xi in Figure 24 on the waveguide's narrowest section, there are geometrical defects originated from molding defects in the stamp that cannot be well understood. Overall, the center section has a constant peak position and width relative to the Raman signal from the original SOI wafer which adds further confirmation of the crystallinity quality of the imprinted waveguides. In future applications, these edge effects can be by-passed if necessary to avoid unnecessary scattering by patterning away from the edge or protecting the buried oxide layer during Mac-Imprint.

Lastly, optical waveguiding is demonstrated in a Mac-Imprinted silicon rib waveguide (Figure 25A). The top view IR imaging (Figure 25B) did not reveal a detectable scattering of the signal from the waveguide's walls, which suggests low scattering loss. The waveguide unfortunately was too short (L = 0.015 cm) to precisely measure its loss.

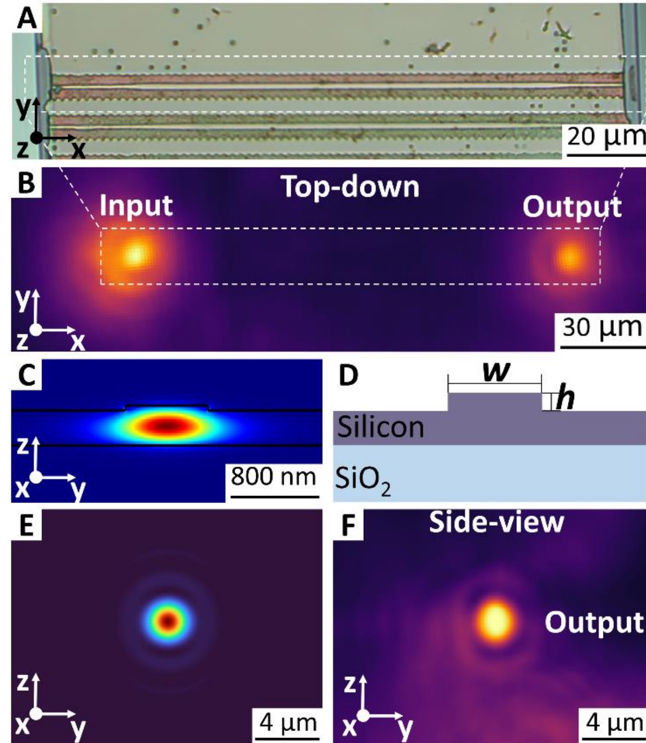

Figure 25. A – top-down optical image of the individual SOI pillar prior to waveguide testing. B – top-down infrared image of the individual SOI pillar during waveguide testing. Dashed lines on A and B highlight the tested waveguide. C – side-view of waveguide mode simulation. D – cross-sectional schematics of the waveguide, used for the simulation. E – side-view of simulated waveguide mode, corrected by PSF of 0.42 numerical appertire objective. F – side-view infrared image of the output waveguide facet.

The waveguide mode simulation of the rib waveguide with nominal width, w = 750 nm, and imprint depth, h = 43 nm, (Figure 25D) is presented on Figure 25C and demonstrates the single mode and quasi-transverse-electric (TE) polarized nature of the waveguide. The convolution of the simulation with the point-spread-function (PSF) of the 0.42 numerical apperture imaging objective is presented on Figure 25E and closely matches the output side-view image of the waveguide facet (Figure 25). For more details on the convolution between simulated waveguide mode and PSF of the objective refer to the Figure 45 in the APPENDIX A. It has previously been shown that that single mode rib waveguides with

similar dimensions can exhibit favorable loss characteristics when compared to fully etched strip waveguides, owing to limited interaction between the waveguide mode and the waveguide surface *(91)*. Hence, optical propagation losses are expected to be a function of both the waveguide design and the surface roughness. The optical characterization demonstrated here importantly confirms that the Mac-Imprint process can be utilized to fabricate functional silicon photonic waveguides.

3.3 Conclusion

This study reported the first extension of Mac-Imprint to SOI substrates and to geometries specific to requirements of silicon rib waveguides. It was established that the mass-transport of the reactants in the perpendicular direction of the waveguide's longitudinal axis is the limiting factor for attaining imprinting of uniform patterns without porosity. This mass transport could not be supported by solid catalysts. In contrast, a nanoporous catalyst provided necessary diffusional pathways which allowed for fabrication of Si waveguides with an average depth of 42.9 nm ± 5.5 nm. This depth variation was attributed to the stamp distortions during demolding of the stamp during its fabrication which can be improved using commercial nanoimprinting tooling. The bottom and sidewall roughness induced by Mac-Imprint was controlled by reducing the pore sizes to within an order of magnitude of the Debye Length (i.e., the resolution limit of the Mac-Imprint). In particular, 10 nm pore size catalyst resulted in a 10 nm bottom and sidewall roughness of the Si rib waveguide which is comparable to similar structures which are made by conventional plasma etching methods. The limited levels of Si defect formation during Mac-Imprint were achieved by the use of the etching solution with high ρ parameter

of 99.5% and were confirmed by Raman analysis of the imprinted waveguide, which revealed a uniform peak position and FWHM thought the middle portion of the waveguide excluding edges. Fabricated waveguides support single-mode light propagation which was measured by the side-view IR imaging and closely matches electromagnetic simulations. Additionally, top-down IR imaging does not reveal detectable light scattering from the waveguide walls. Overall, this paper represents a significant step towards commercial implementation of the Mac-Imprint for the fabrication of functional 3D freeform optoelectronic devices, such as advanced waveguides *(3, 4, 62–64)* surface plasmon structures *(1)* and chromatic-aberration corrected lenses.*(6)* Moreover, Mac-Imprint's unique ability to tailor its nanoscale roughness could be advantageous in fabrication of quasicrystal interferometers with physical unclonable functions which are essential for hardware and information security *(65)*. In the future, improvements to the stamp design aimed at embedding the etching solution storage reservoir in it instead of in the substrate are necessary for scaling the technique to blank SOI wafers. The work on determining the maximum EEPD supported by the thin-film catalyst in this paper should inform the reasonable pitch that should exist between the embedded reservoirs in such proposed stamp designs. This approach will also allow for free optimization of Mac-Imprint parameters as the undercut of the BOX layer of the SOI pillar will be eliminated entirely. The authors also see potential scaling of Mac-Imprint in its integration with commercial mask aligners and nanoimprinting technologies presently used for polymer patterning by (i) adding liquid handling capabilities, (ii) using less hazardous chemicals to simplify equipment design and (iii) investigating demolding strategies particularly for high-aspect ratio patterns.

3.4 Methods

3.4.1 Substrate Preparation

Mac-Imprint was performed on SOI wafers with 340 nm thick, p-type boron-doped device layer which has resistivity of 14 – 22 Ω·cm and (100) crystal orientation. Prior to Mac-Imprint, arrays of 270 µm tall and 150 µm wide pillars spaced by 900 µm were fabricated on the SOI wafers by photolithography and deep-reactive ion etching in order to provide etching solution storage volume. The articulation on the necessity of SOI wafer pre-patterning and guidelines for the design of pillar size can be found in APPENDIX A. Pre-patterned SOI wafers were firstly thoroughly rinsed with acetone, isopropyl alcohol and deionized (DI) water. Afterwards, the RCA-1 cleaning was performed for which they were immersed for 15 min into hot (i.e. 70 °C) aqueous solution of ammonium hydroxide and hydrogen peroxide in (5:1:1 by vol.). After the RCA-1 cleaning pre-patterned SOI wafers were thoroughly rinsed with DI water and were considered ready for the Mac-Imprint.

3.4.2 Stamp Preparation

The fabrication of Mac-Imprint stamps consisted of four steps which are described below and detailed protocol of those can be found elsewhere *(92)*.

3.4.2.1 PDMS replica molding (Figure 26): At first, waveguide pattern was created on a Si master mold using e-beam lithography followed by reactive ion etching. Next, the pattern of the Si master mold was replicated onto PDMS according to the standard replica molding procedure *(93)*. Here, the Si master mold was firstly cleaned with RCA-1 solution

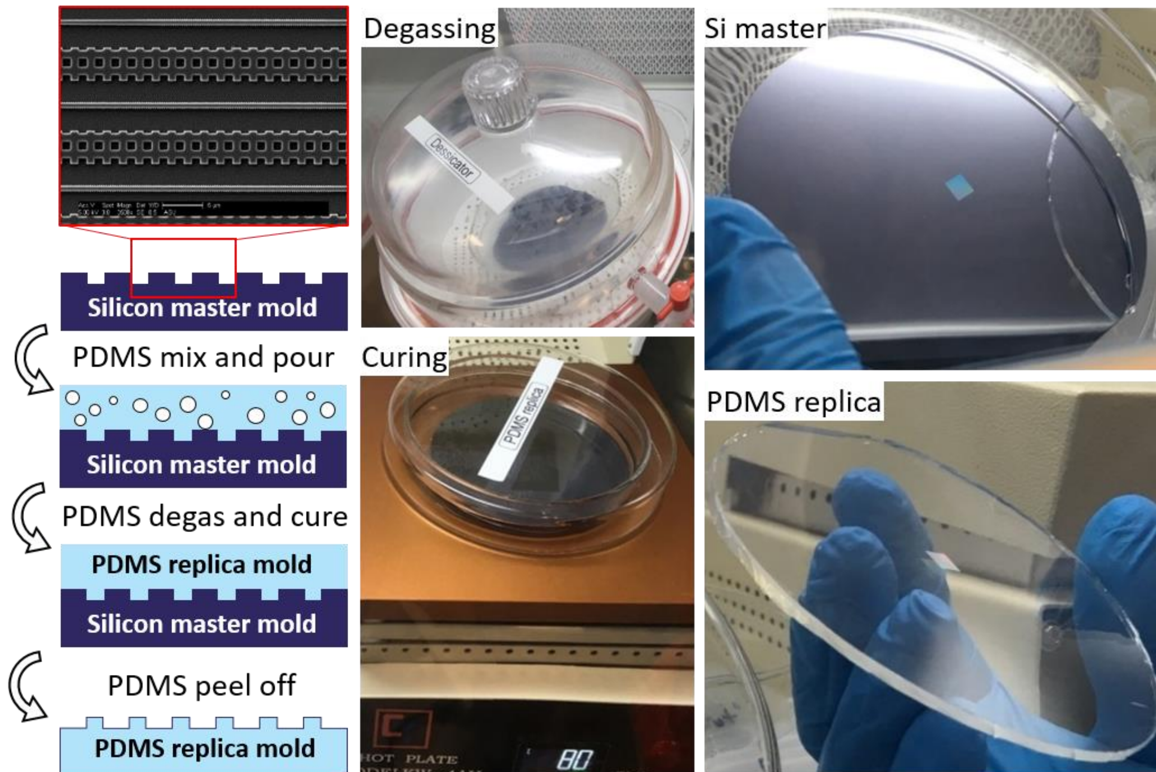

Figure 26. PDMS replica molding procedure.

followed by DI water rinsing. Next, the Si master mold was placed inside the desiccator next to the Petri dish with few droplets of trichloro(1H,1H,2H,2H-perfluorooctyl)silane (PFOCS) and the vacuum was applied for 15 min. This step lead to the PFOCS deposition on the surface of the Si master mold which made it hydrophobic. After that the liquid PDMS was prepared by mixing base and curing agents of the SYLGARD 184 Silicone elastomer kit in 10:1 ratio (by mass). Liquid PDMS was subsequently poured over the Si master mold and vacuum was applied for additional 30 min to remove air bubbles trapped into the liquid PDMS. After that the PDMS was cured at 80 °C for 120 minutes using leveled hotplate. Upon curing the PDMS replica mold was peeled off from the Si master mold and was considered ready for the next step.

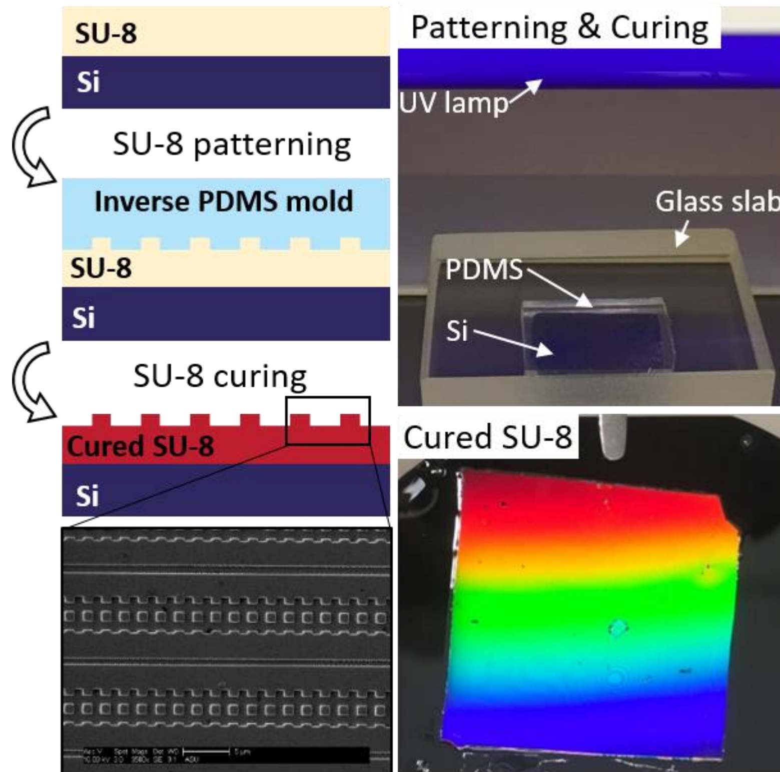

Figure 27. Waveguide pattern transfer onto the SU-8 layer using soft nanoimprint lithography.

3.4.2.2 Soft nanoimprint lithography (Figure 27): After that, PDMS replica mold was used to pattern photoresist by means of nanoimprint lithography. To do so, 2.5 x 2.5 cm^2 Si chips were firstly cleaned by RCA-1 solution followed by DI water rinsing. Next, a 20 µm-thick layer of SU-8 2015 photoresist was spin-coated onto clean Si chips. Upon spin-coating, the PDMS replica mold was placed on top of the photoresist layer with pattern facing down and pressed with the UV transparent glass slab, yielding 15 g/cm^2 of pressure. The UV curing was performed under 6 W UV bulb placed at 10 cm distance from the SU-8 surface for 2 hours.

3.4.2.3 Catalytic metal sputtering (Figure 28): Upon UV curing, Si chips with patterned SU-8 layer were placed inside NSC-3000 magnetron sputter chamber at 20 cm

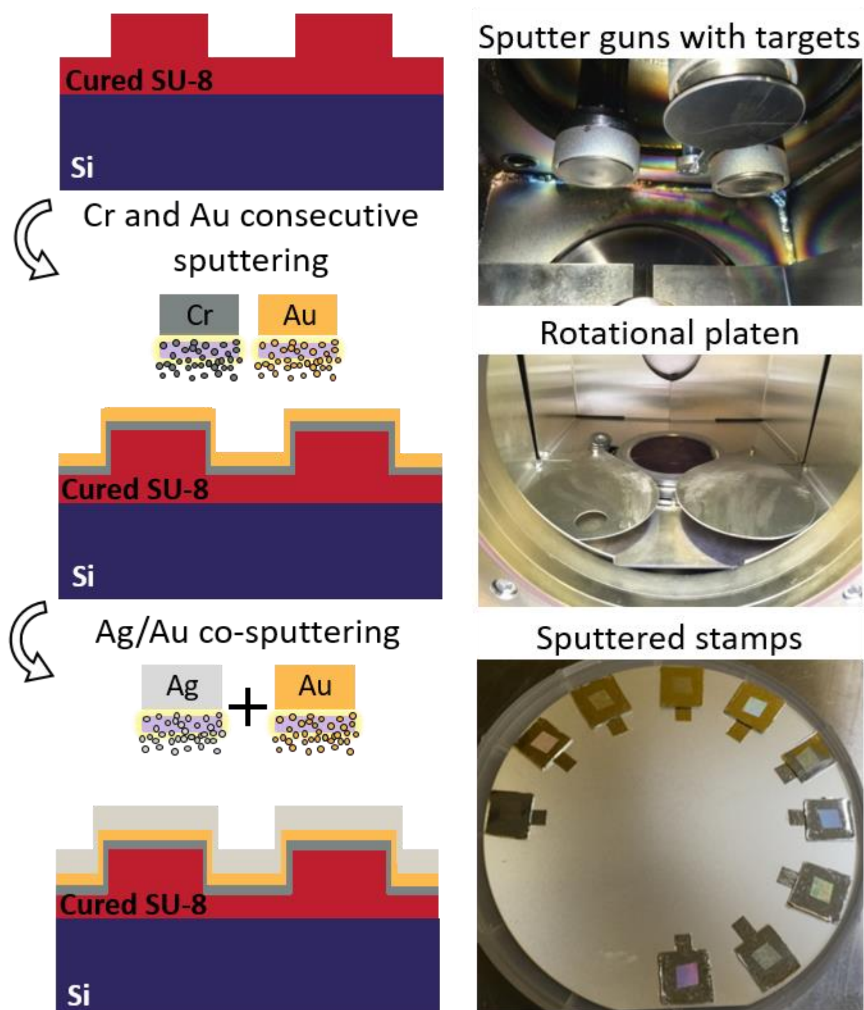

Figure 28. Schematics of the thin-film catalyst deposition by magnetron sputtering and photographs of the process.

distance from the sputtering targets. For the Mac-Imprint with solid catalyst, two layers of metal were deposited onto the stamp in the following order: 20 nm Cr (adhesion) and 80 nm Au (catalyst). For the Mac-Imprint with porous catalyst, three layers of metal were deposited onto the stamp in the following order: 20 nm Cr (adhesion), 50 nm Au (intermediate) and 375 nm Ag/Au alloy (precursor for porous catalyst).

3.4.2.4 Porosification of catalyst: In order to create nanoporous catalysts, stamps with 375 nm Ag/Au alloy (51 at.% of Ag) were subjected to selective dissolution of Ag by means of dealloying in far from equilibrium conditions. The dealloying was performed in aqueous solution of nitric acid (H2O:HNO3 = 1:1 by vol.) at a constant stirring rate of 100 rotations per minute following the protocol established in the work of Niauzorau et al. *(68)*. The pore size of the catalyst was controlled by varying dealloying time and solution temperature. In particular, the np-Au with average pore sizes of 10 and 14 nm was produced at room temperature solution within 10 and 30 min, respectively, while the 27 nm average pore sizes were obtained at 65 °C temperature solution within 10 min. After the dealloying, a subset of porous catalytic stamps with average pore sizes of 27 nm was annealed in Ar environment at 250 °C for 1 hour in order to increase average pore size to 42 nm through thermal coarsening.

3.4.3 Mac-Imprint Setup and Conditions

The Mac-Imprint set-up is composed of an electrochemical cell, a Teflon rod acting as a stamp holder, a load cell, and a vertical stage (Figure 29A). The electrochemical cell holds substrates and etching solutions while the stamp holder connects the stamp to the vertical stage trough the load cell. Critical to any nanoimprinting technique is to achieve conformal contact between stamp and substrate. Since both substrate and stamp in this case are flat and rigid monocrystalline Si chips, tip-and-tilt misalignments between them can reduce the contact area dramatically *(53)*, leading to imprinting inconsistency and deregulating Mac-Imprint redox kinetics *(24)*. To address this issue, the SOI substrate was placed first into an electrochemical cell in dry conditions and its plane was used as a

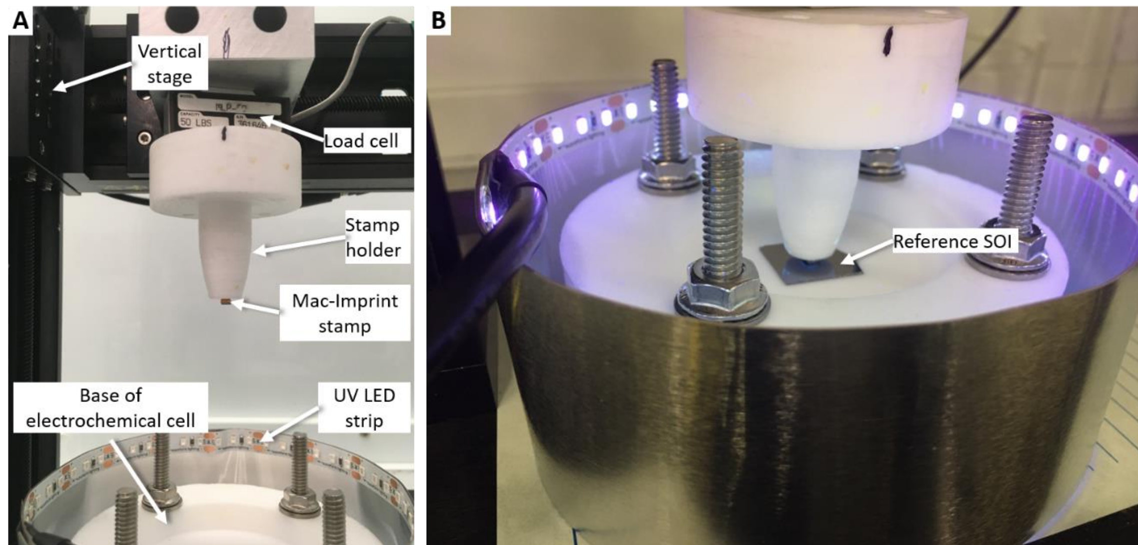

Figure 29. Mac-Imprint system. A - Photograph of the Mac-Imprint system in the disengaged state. B – Photograph of the stamp-to-substrate alignment step with omniderictional UV curing.

reference for the stamp-to-substrate alignment. The stamp was placed on the top of the SOI substrate with the catalyst side facing down and a small portion of SU-8 2015 was dropped on the back side of the stamp to adhere the stamp to a Teflon rod. The Teflon rod was brought in contact with SU-8 droplet by manual commands. Circular illumination by 365 nm UV light for 1 hour was used to uniformly cure the SU-8 2015 in place (Figure 29B). Since this attachment step was performed at room temperature and stress-free conditions, the alignment was preserved. After curing, the stamp can be retracted by the automated stage without loss of alignment. The SOI substrate is placed inside the electrochemical cell, which is then filled with the etching solution. The vertical stage brings a stamp holder with mounted stamp in plate-to-plate contact with SOI substrate. The contact force of 22.24 N is developed within 0.1 sec and maintained within ±5% of the set-point for 10 ± 0.1 s. This allows Mac-Imprint of the waveguide patterns to be reproducible provided the stamp-to-

substrate alignment remains unaltered. After the imprinting, the stamp is retracted into home position and etching solution is aspirated from electrochemical cell. Further, SOI substrate is immediately flushed with excess amount of isopropyl alcohol to terminate the undercut of buried oxide layer. The total time of SOI substrate exposure to the etching solution is 70 sec. Detailed description of Mac-Imprint setup and protocol can be found elsewhere *(92)*. It should be noted that ±5 sec variation in the Mac-Imprint total processing time (i.e., ~ 70 s) does not significantly affect the buried layer undercut depth (see Figure 46 APPENDIX A).

The etching solution with ρ equal to 99.5 % is prepared by mixing HF (48 % by vol.) and H_2O_2 (30 % by vol.) in the 68:1 ratio (HF:H_2O_2; by vol.). Moreover, pure ethanol is added to the etching solution (4 % of the etching solution volume) in order to improve solution's wettability. A fresh etching solution was mixed prior every Mac-Imprint operation. All chemicals were ACS grade, purchased from Sigma Aldrich.

3.4.4 Morphological, Structural and Functional Characterization

Morphological properties of the Mac-Imprint stamps and imprinted waveguides were characterized by scanning electron microscopy (SEM) using Philips XL-30 FEG SEM. All SEM images were acquired at 10 kV accelerating voltage and 130 pA beam current.

Imprint depth profiles were characterized by atomic force microscopy (AFM) using the Witec Alpha 300 RA+ system. AFM scans were acquired in tapping mode using NHCV-A Bruker probes with tip radius of 8 nm, spring constant of 40 N/m and resonant frequency of 320 kHz. For AFM image acquired in Figure 20, the lateral resolution is

determined by sampling distance which is set to be 234 nm and 39 nm in the x- and y-directions, respectively. The resolution of its height is set by the AFM instrumentation which, as per the vendor, it is 0.5 nm.

The nanoscale defects of the imprinted waveguides and surroundings were characterized by confocal Raman microscopy using the same Witec system. The Raman signal was excited by 532 nm laser with the 0.1 mW output power. Raman signal was acquired using 1800 g/mm grating yielding 1 cm-1 spectral resolution with the accumulation time of 0.2 sec. Individual Raman mapping was performed over 4 x 9 µm2 area with total amount of 40x90 data points.

The performance of the waveguide was characterized using near-IR (O-band) light from a tunable laser (Santec TSL-550), which was coupled onto the chip using through a polarization controller and tapered lensed fiber (OZ optics) and aligned using XYZ piezo controlled alignment stage (Thorlabs NanoMax). Fiber-to-chip alignment and successful waveguiding was verified by IR imaging both the top surface and output side-view of the chip with infrared cameras (Hamamatsu C2741). Waveguide mode simulation of the nanoimprinted silicon waveguide cross-section were performed at the wavelength 1310 nm using the finite difference eigenmode method (Ansys Lumerical MODE). The waveguide cross-sectional facet view IR imaging was modelled by convoluting the waveguide mode profile with the point spread function (PSF) of the NA = 0.42 imaging objective.

3.4.5 Scanning Electron Microscope Image Analysis

The quantification of (i) np-Au average pore size and (ii) bottom roughness of the waveguide surrounding as performed through the analysis of the top-down SEM images

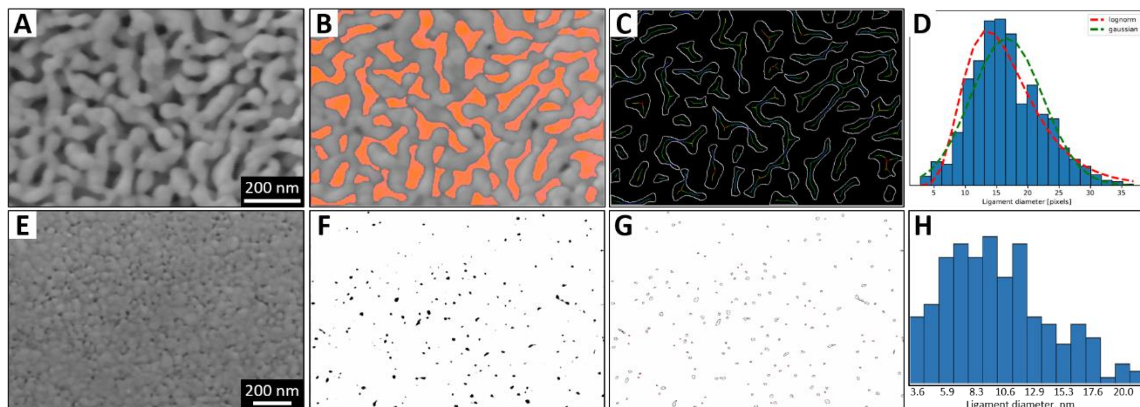

Figure 30. Analysis of the np-Au pore sizes using AQUAMI (A-D) and ImageJ (E-F). A and E – Original top-down SEM images. B and F – threshold operation. C and G – outlines of individual pores. Note, lines within the outlines on C represent weighted centers of the pores with colors representing distance to it's edges. D and H – Distribution of the pore diameters.

using AQUAMI *(94)* and ImageJ software. The AQUAMI software has specifically developed threshold algorithm that makes it effective for the analysis of bi-continuous porous Au structures. Here, an input SEM image (Figure 30A) is firstly thresholded (Figure 30B) and converted to the binary mask. After that, the weighted center line for each individual pore or protrusion is computed and the distance from it to the edge of the pore is found. The distance is represented by the color on Figure 30C. Based on these values the distribution of all diameters across the SEM image is calculated as average ± standard deviation (Figure 30D). However, this algorithm failed to analyze small, isolated objects, which is the case of np-Au with the small pore sizes (Figure 30E) and corresponding imprinted Si surface. For the analysis of those samples ImageJ software with manual threshold (Figure 30F) was used. The individual pore or protrusion diameter in this case was calculated from the it's area using circular approximation (Figure 30G). This

assumption was made based on the fact that in the early stages of dealloying pores nucleate at the grain boundaries of the precursor alloy and would assume circular or near-circular shape. In this case the average pore or protrusion size and it's standard deviation was calculated based on all pores detected on the original SEM image (Figure 30H).

The analysis of the line edge roughness was performed by calculating the RMS of the waveguide's line edge profile obtained from high-magnification SEM images (Figure 31A). Each LER is an average of four independent RMS measurements of different 2-μm long waveguide segments (Figure 31B). Thus, a specifically written Python code utilized Canny edge detection algorithm with Gaussian filter size sigma equal to 2.6 in order to obtain the profiles of the waveguide edges (Figure 31C). Finally, the LER of extracted line edge profile was found as an RMS of the pixel values multiplied by pixel size. It is worth noting that the accuracy of this algorithm depends on the pixel size of the SEM image. In this work, all images had a pixel size of 6.43 nm.

Nearest neighbor distance analysis was performed using ImageJ software according to the algorithm published elsewhere *(95)*. The nearest neighbor distance is found for each particle detected on the image as an average of five nearest neighbors with the example presented on Figure 32A-C. Note that nearest neighbor distance for the each sample is calculated as average of all particles detected on the original SEM image.

3.4.6 Statistical Analysis

Analysis of AFM data was performed using Gwyddion software. Prior extracting imprint depth, the AFM data was leveled with respect to the non-imprinted top surface

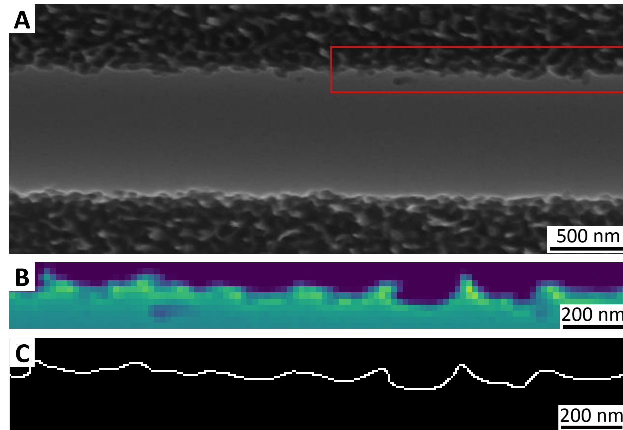

Figure 31. LER analysis. A – original top-down SEM image with highlighted portion of the waveguide for the Python algorithm. B – Cropped portion of the waveguide imported into the Python algorithm. C – extracted line edge profile

using "Mean Plane Subtraction" function. The individual imprint depth (Figure 20B, inset) was found from "Step-height" fitting function of "Critical dimension" module with error bar representing fitting error. The average imprint depth and it's standard deviation (SD) was calculated based on 148 measurements along the AFM scan.

In the analysis of work by Liu et al. the average overetched distance and it's SD was calculated based on 9 reported measurements.

The analysis of the average size of np-Au pores, Si protrusions and nearest neighbor distance was performed using AQUAMI and ImageJ software without any pre-processing of SEM images. The magnification was kept constant throughout the SEM images to maintain the same pixel size. Sample size for each measurement in this case was different and dependent on the amount of pores/protrusions present on the SEM image. Note that for a given sample the nearest neighbor distance for individual particle is found as an average distance to five nearest neighbors. The nearest neighbor distance of the sample is

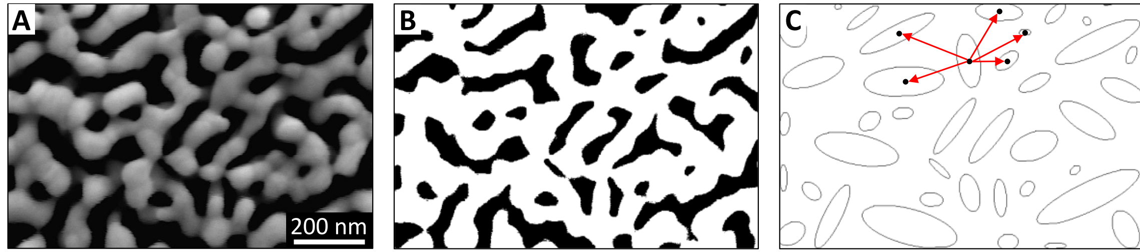

Figure 32. Nearest neighbor distance analysis with original top down SEM image (a), threshold mask (b) and distances between centers of five nearest neighbors (c, red arrows). then calculated as average of all individual nearest neighbor distances. Data was presented as average ± SD.

The analysis of the LER was performed by calculating the RMS of the waveguide's line edge profile obtained from high-magnification SEM images. The magnification was kept constant throughout the SEM images to maintain the same pixel size. Prior importing SEM images to the Python code, the bottom surface on the SEM images was thresholded and images were converted into .txt format using ImageJ. Waveguide line edge profiles were obtained on 2-µm long waveguide segments using Canny edge detection algorithm with Gaussian filter size sigma equal to 2.6. The LER of individual line edge profile was calculated as an RMS of the pixel values multiplied by pixel size. The LER of the sample is then calculated as average of 4 independent measurements of different waveguide segments. Data were presented as average ± standard deviation (SD).

The analysis of the Raman data was performed using Project FIVE software. Prior extracting Raman signal position and full width at half-maximum, the signal was fitted using Lorentz function. The average peak position, full width at half-maximum and it's SD was calculated using data from the waveguide region only (i.e., excluding waveguide surroundings).

CHAPTER 4

ELECTROCHEMICAL NANOIMPRINTING OF SILICON LENSES: TOWARDS BIO-INSPIRED INFRARED META-OPTICS

Anti-reflection coatings for IR lenses were designed for imagining in harsh environments such as dust (e.g., moon), micrometeorites (e.g., Lagrange points), and high-radiation fluctuations (e.g., Mars) with limited lifetimes. Multifunctional optical meta-surfaces (MOMS) can simultaneously deliver high thermal stability and anti-fouling behavior due to its monolithic nature (e.g., no CTE mismatch) and low dust adherence, respectively. Due to the incompatibility of micromachining with non-planar inorganic substrates, MOMS have only been demonstrated in polymeric lenses. In this paper, a new method of conformal electrochemical nanoimprinting is presented to directly micromachine a nature-inspired sharklet pattern onto a silicon lens. Uniquely, this approach uses gold-coated patterned membranes that are used as stretchable catalytic stamps that can be inflated against a non-planar substrate. With the advent of designs methodologies for 3D optical metasurfaces, MOMS may now be extended into lenses made of silicon, germanium and potentially other III-V semiconductors.

4.1 Introduction

Biological three-dimensional (3D) hierarchical structures from the compound moth eye (Figure 33A) serve as multifunctional optical meta-surfaces (MOMS) that not only perform focusing and broadband, omnidirectional anti-reflection (AR) *(96)* but also deliver

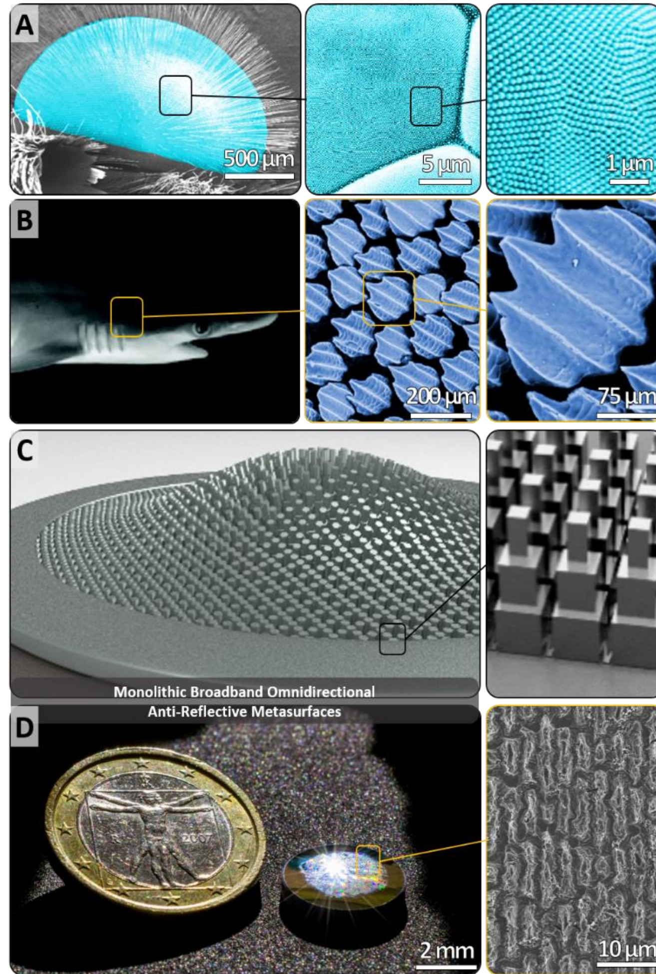

Figure 33. Conformal electrochemical nanoimprinting of Si lens. (A) Compound moth eye structure with SEM images highlighting hierarchical structure of it's ommatidia. Reproduced with permission from *(123)*. (B) Antifouling shark skin with SEM images highlighting ridges on it's scales. Reproduced with permission from *(124)*. (C) Concept of broadband omnidirectional antireflective surface monolythically integrated onto the plano-convex lens. (D) Optical image of the unifromly patterned plano-convex Si lens demonstrating strong light diffraction from the imprinted surface. The lens is placed next to the picture of Vitruvian man on the back of 1 Euro coin for size comparison. SEM image demonstrates a unit cell of imprinted sharklet pattern.

anti-fouling behavior similar to that observed in shark skin (Figure 33B) *(97)*. To reproduce them into synthetic devices, many researchers have utilized modern nanomanufacturing

tools, both additive *(98–100)* and forming methods *(101, 102)* with ample success in polymer-based smart lenses *(5)*. While MOMS have been successfully translated into planar inorganic semiconductor wafers (e.g., Si, Ge or GaAs), their integration onto 3D curvilinear substrates such as lenses are severely limited due to the lack of compatible and scalable techniques to fabricate them. If possible, MOMS monolithically integrated onto semiconductor IR lenses (Figure 33C) could solve several issues associated with commercial AR coatings for harsh environments (e.g., space exploration) such as thermal degradation and image distortion due to CTE mismatch in ceramic coatings *(103)* meanwhile providing desired functions such as regolith dust anti-fouling on the Moon or Mars *(104)* for its long-term exploration and human inhabitation.

3D parallel lithographical methods for polymeric resins and micromachining processes can be combined to etch 3D microscale geometries into planar inorganic wafers. Due to the incompatibility of planar masks used in lithography to non-planar substrates, conformal lithography approaches were invented to pattern on curvilinear surfaces (e.g., lenses) such as detachment lithography *(105)*, microcontact printing *(12, 106)* or nanoimprint lithography *(27)*. However, when the latter is combined with micromachining processes such as deep-reactive ion etching, not only it is plagued by its traditional limitations such as (i) limited control of the etch selectivity of the mask and (ii) the aspect ratio-dependent etch rate, both of which result in depth spatial inaccuracies and limits the 3D shape patternability *(10, 107)*, but also (iii) pattern distortions due to the misorientation of incident ion flux relative to the normal vector of the surface of curvilinear substrates resulting in spatially varying etch rates and depths *(12, 13)*.

Metal-assisted electrochemical nanoimprinting (Mac-Imprint) is an established contact-based catalytic wet etching method *(20)* capable of micromachining 3D hierarchical patterns in silicon wafers. It works by catalyzing the selective dissolution of silicon at the contact points between itself and catalyst-coated rigid stamps in the presence of a wet etching solution *(31)*. In this work, a new generation of stretchable and inflatable composite stamps based on porous polyvinylidine fluoride (PVDF) are introduced to enable a conformal format of Mac-Imprint for non-planar substrates. The next paragraphs present an evolution of rational materials selection for Mac-Imprint stamps contextualized to prior work that culminates with the demonstration of patterning of hierarchical shartlet patterns onto a silicon lens (Figure 33D).

4.2 Results and Discussion

4.2.1 Proof of Concept. Plate-to-Plate Mac-Imprint

In the first generation of stamps developed for Mac-Imprint of silicon (Figure 34A), the enabling mechanism is the diffusion path created through a network of nanopores embedded in the thin-film catalyst *(24)* that allowed for uniform patterning of 3D microscale features with high-fidelity (i.e., sub-22 nm shape deviations) over features as wide as 10's of microns while imprinting the catalyst's pore morphology into the substrate. This demonstration highlighted Mac-Imprint's ability to, in a single-step, deterministically pattern hierarchical structures whose width spans nearly 3 orders of magnitude. Suppression of the catalyst's pore size via dealloying in far from equilibrium conditions to within an order of magnitude of the Debye Length (i.e., 0.9 nm) was presented in the previous chapter and it yielded roughness reduction down to sub-10 nm comparable to that

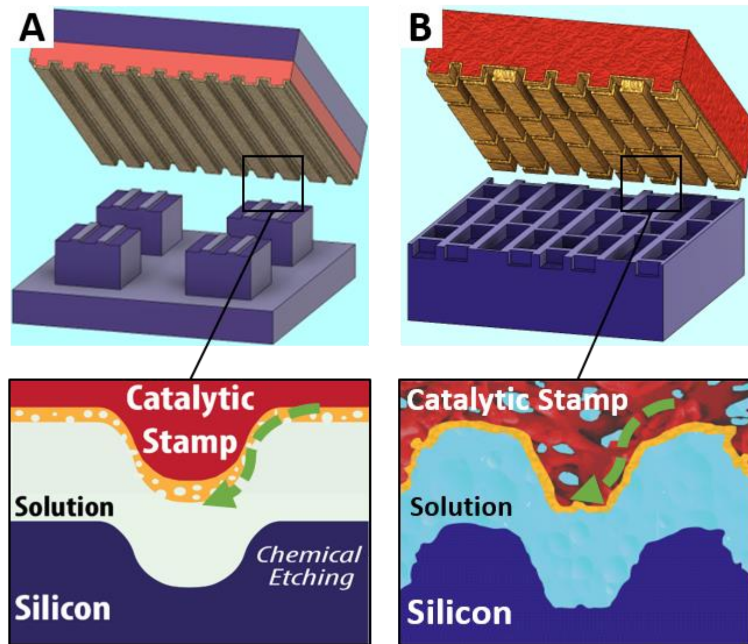

Figure 34. Development of the Mac-Imprint stamps. A – First generation stamps in which the reactant diffusion pathways were embedded into the porous catalytic layer of the stamp and etching solution storage was embedded into the substrate. B – Proposed next generation of the stamps in which both reactant diffusion pathways and etching solution storage would be embedded into the stamp.

generated by deep-reactive ion etching and fine periodic structures as small as 220 nm opening up applications for designer rib waveguides *(25)*. However, the first generation required embedded gaps in the substrates or stamps in the order of 100's of microns to store solution (e.g., pre-etched pillars, Figure 34B) since neither the substrate nor the stamp were porous and could offer ample solution storage which limited etching depths to sub-1 μm *(24, 25)*. This issue was extensively discussed in the previous chapter in the context of maximum achievable EEPD when the Mac-Imprint with the first generation of the stamps was performed on the bare SOI wafer (Figure 17).

Similarly to the first generation of the Mac-Imprint stamps in which etching solution diffusion pathways were embedded into the stamp it was hypothesized that the same approach could be implemented to solve etching solution storage limitation (Figure 34B). In order to achieve this goal, this work draws inspiration from literature in water filtration *(108)*, and proposes to use gold-coated porous PVDF membranes as a new class (i.e., 2nd generation) of HF-resistant stamps for Mac-Imprint which not only provides diffusional pathways but also stores reactants within its thickness at the vicinity of the metal-silicon interface (Figure 35A), eliminating the need for pre-etched or embedded gaps between the substrate and stamp, and expanding Mac-Imprint to chip- and wafer-scales (Figure 35B). Estimation of the etching solution storage capacity of porous polymer membranes and it's comparison with that of pre-patterned wafers is presented in APPENDIX B. This approach possesses two key challenges. First, its patterning capabilities are restricted to randomly textured Si surfaces (Figure 35C) that represent the inverse morphology of membrane's pores (Figure 35D). Through engineering the membrane's pore morphology during its synthesis via phase inversion *(108)* it can be tailored to design monolithically integrated surfaces with hydrophobicity (Figure 35E and F) for self-cleaning and anti-fouling applications *(109, 110)* and broadband omnidirectional anti-reflection (Figure 35G) for high-performance infrared optics *(96, 111)*. Second, most of these membranes are made from high-throughput roll-to-roll processes and possess macroscopic imperfections such as scratch marks, spatial variations

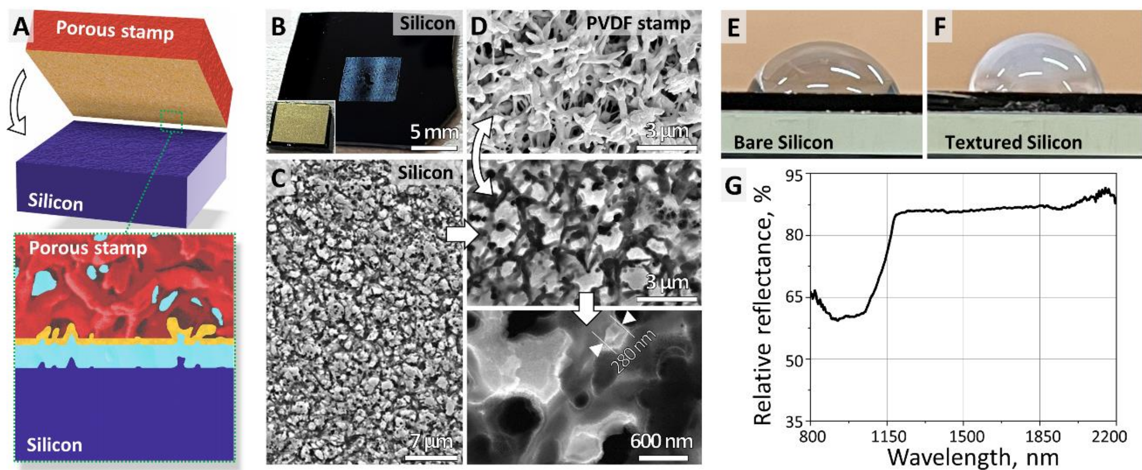

Figure 35. Proof of concept. A – Schematics of Mac-Imprint with second generation of the stamps. B – Photograph of imprinted Si chip. C – SEM images of the Si surface, imprinted with random protrusions. D – SEM image of the second generation of the stamps. E – Water contact angle with bare Si chip. F – Water contact angle with imprinted Si chip. G – Hemispherical reflectance of imprinted Si chip relative to bare Si.

of the pore sizes and limited flatness that are deterministically transferred onto Si (e.g., dark marks on Figure 35B).

The key to address these challenges lays in the membrane patterning and improvements of the it's surface quality to meet strict flatness requirements of the Mac-Imprint. To achieve this several routes exists, one performs patterning of the existing membranes by means of thermal embossing nanoimprint lithography *(112)* while the other focuses on the in-lab fabrication of porous membranes using thermal-induced phase separation (TIPS) technique *(113)*. Specifically, in the former approach patterning of commercially-available water filtration membranes is performed similarly to classical NIL, however the temperatures are kept below glass transition of the polymer in order to minimize pore clogging. This approach indeed also helps to improve surface flatness of the membranes, however the large-area macroscopic defects of the roll-to-roll manufacturing

processes still remain present on the membrane. On the other hand, the TIPS approach doesn't suffer from those defects as membranes are made from liquid solution casted over the mold and the surface quality of the membranes is determined by that of the mold, which could not only assure flat surface but could also allow for the *in-situ* membrane patterning.

Due to these advantages TIPS has been selected as a most promising method for the fabrication of the next generation of Mac-Imprint stamps with improved flatness and 3D sharklet patterns (Figure 36A). Its hierarchical features sizes – i.e., 30 μm, 4 μm, 1.5 μm and ~200 nm corresponding to the sharlet's pattern period, its grating period, spacing and pore morphology, respectively (Figure 36D) – successfully Mac-Imprinted deterministically over the entire contact area (Figure 36B) with no observable loss of nanometric detail (Figure 36C) owning to the short Debye length of the electrolyte (21). Similar to prior work in Mac-Imprint with nanoporous gold catalysts *(23–25)*, the stamp's pore size limits the smallest lateral features size that is imprintable as well as its line-edge roughness (Figure 36C).

Albeit not optimized, the imprinted hierarchical sharklet patterns possess broadband anti-reflection in the mid-IR range *(114)* (Figure 36G) owning to the sub- and near-wavelength geometries reducing backward light scattering *(96)*. The monolithic nature of Mac-Imprinted AR surfaces makes it a great candidate for enhancing thermal imagining in extreme environments particularly in space exploration since it overcomes (i) the environmental and thermal degradation associated with polymer-based coatings *(115)* and (ii) the thermal-induced stress and distortions associated with ceramic-based coatings owning to their mismatch in the coefficient of thermal expansion *(103)*. In fact, if higher

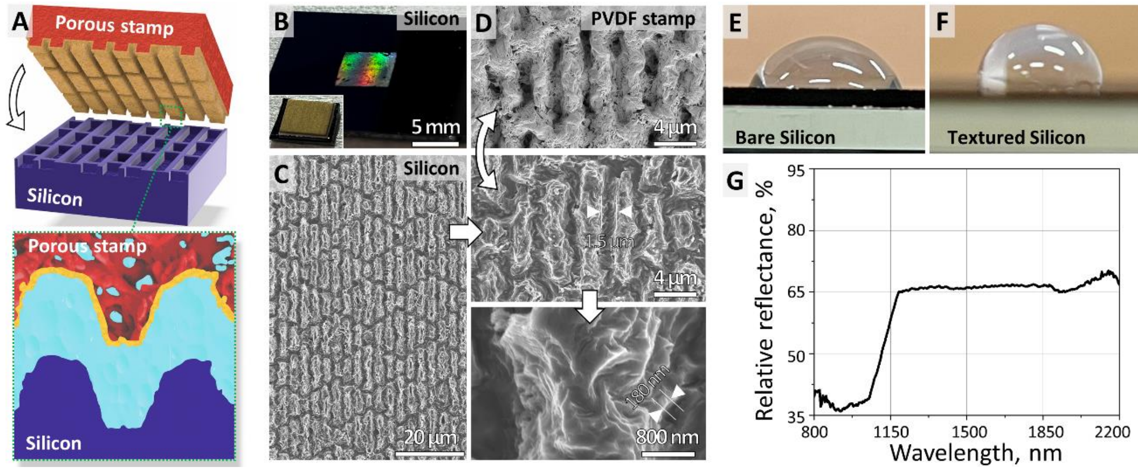

Figure 36. Mac-Imprint of hierarchical patterns. A – Schematics of Mac-Imprint with the third generation of the stamps. B – Photograph of imprinted Si chip. C – SEM images of the Si surface, imprinted with Sharklet patterns. D – SEM image of the third generation of the stamps. E – Water contact angle with bare Si chip. F – Water contact angle with imprinted Si chip. G – Hemispherical reflectance of imprinted Si chip relative to bare Si.

aspect ratio surfaces could be Mac-Imprinted in the future, it is possible its performance in terms of broadband and omnidirectional anti-reflectivity would be comparable or better than traditional interferometric coatings as prior literature on silicon nanowires and nanocones *(116, 117)*. Note that aspect ratio in Mac-Imprint is limited by demolding issues and relieve angle of its features *(74)*. In the future, advancements in patterning technologies for nanoporous polymers with reduced pore size and feature dimensions could expand the application of the 3rd generation of Mac-Imprint stamps to more complex geometries and towards shorter operating wavelengths in 3D visible *(7)* and X-ray *(8)* range optics.

It should be noted that relatively low reflectance suppression of Si textured with random and sharklet patterns (i.e. 90% and 65% of bare Si in the near IR range, respectively) is partially attributed to the contributions of IR light passed through the Si

chip and reflected from it's un-patterned back side. This observation suggests that for the efficient reflection suppression both front and back sides of the Si have to be patterned as has been demonstrated by Kamizuka et al. *(118)*.

In order to validate the explanation of differences in the macroscopic imprint uniformity of commercial and TIPS membranes their surface topology was investigated using optical profilometry (Figure 37). At first, arrays of bright dots uniformly distributed throughout the membrane surface, randomly distributed bright scratch marks and "S"-shaped dark artefact in the center of the membrane can be observed on the optical image of commercial PVDF stamp (Figure 37A). These features are faithfully transferred onto the surface of imprinted Si in the form of non-imprinted regions in addition to the areas of shallower etching as indicated by lesser brightness (Figure 37B). The origin of latter can not be understood from the optical image of the stamp, however it's optical profilometry reveals areas of macroscopic indentations indicated by the dark color on Figure 37C which lead to the non-uniform contact between stamp and Si resulting in it's uneven etching. Additionally, dark-colored "S"-shaped artefact can also be distinguished in the center of the optical profilometry scan. It should be noted that relatively small resolution of the large-area scan (i.e. spot size is 25 µm) does not allow to clearly identify the arrays of bright dots. However, the small-area optical profilometry with the scan resolution of 10 µm easily identifies them as the indentations with the lateral sizes ranging from 20 to 100 µm (Figure 37D).

On the other hand, the optical image of the TIPS PVDF (Figure 37E) does not reveal any periodic artefacts which is attributed to it's manufacturing process (i.e. solution casting

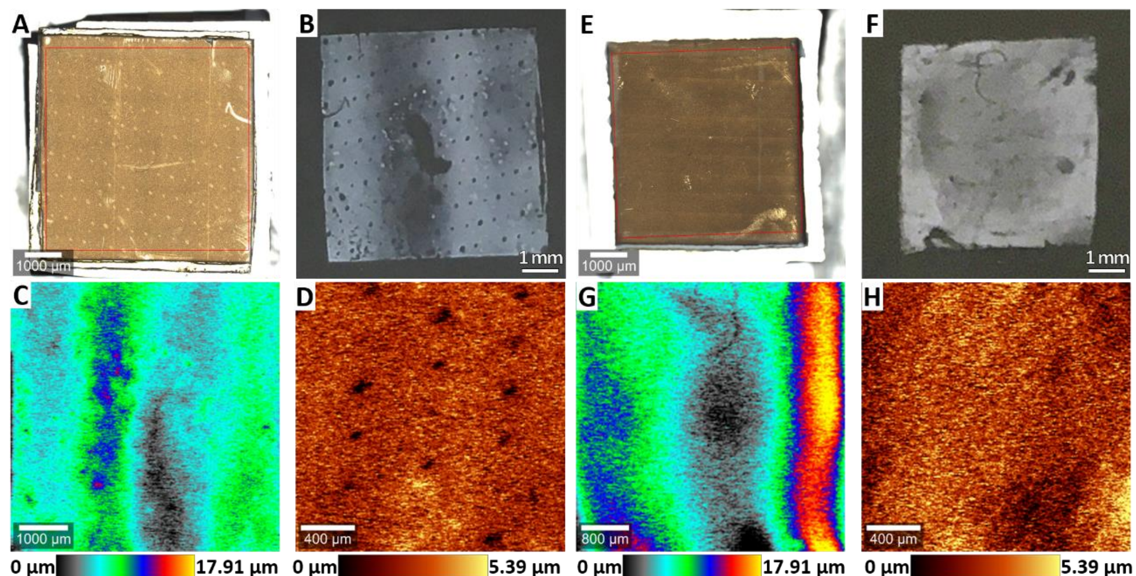

Figure 37. Analysis of the surface topology of porous PVDF plate-to-plate stamps. A – Optical image of the commercial PVDF stamp. Red square highlights portion of the stamp used for the large area optical profilometry. B – Photograph of the imprinted Si chip. C – Large-area optical profilometry. D – Small-area optical profilometry. E – Optical image of the TIPS PVDF stamp. Red square highlights portion of the stamp used for the large area optical profilometry. F – Photograph of the imprinted Si chip. G – Large-area optical profilometry. H – Small-area optical profilometry.

onto the master mold). Some bright scratch marks on it's surface can be attributed to the membrane handling during the stamp preparation (i.e. tweezers indentations). These local defects can be observed on the surface of imprinted Si in the form of unimprinted areas (Figure 37F). However, macroscopically patterned area looks more uniform than that of the Si imprinted with the commercial PVDF stamp with only slight decrease of the pattern brightness in the center (Figure 37F). Large area optical profilometry scan reveals macroscopic indentation in the center of the membrane (Figure 37G) with peak-to-valley heights almost 2 times larger than that of the commercial PVDF. More uniform imprinting in this case could be attributed to the mechanical behavior of the thick TIPS PVDF

membrane which allows for some non-flatness compensations upon plate-to-plate contact while still remaining under the elastic deformation. The small-area optical profilometry does not reveal any periodic defects further adding to the superior surface quality of the TIPS PVDF comparing to that of the commercial PVDF (Figure 37H).

4.2.2 Development of the Conformal Mac-Imprint

The elastic properties of thin, porous membranes such as low Young's modulus (~330 MPa) and its extended elastic limit allows them to achieve mechanical flexibility, and reasonable stretchability (up to 2% strain). When coated with a conformal gold catalyst thin-film layer with sub-80 nm thickness, the membrane's remains flexible and stretchable because the gold coating is so thin that its 3D morphology is allowed to flex mimicking materials used in stretchable electronics *(119)*. In Mac-Imprint, these mechanical characteristics are now exploited to create stamps that can conform to both flat and curvilinear silicon substrates which is a new capability for Mac-Imprint. This is achieved by laminating them with a solid polyimide (PI) film and applying hydrostatic pressure on its back to inflate the laminate composite against the surface of a silicon substrate (Figure 38A) which mimics the stamp's actuation strategy of modern NIL equipment *(120, 121)*. When immersed in the electrolyte, the gold coated membrane micromachines the silicon surface while in a bi-axial state of stress. This configuration overcomes key limitations of plate-to-plate Mac-Imprint *(53)* such as (i) the tip-and-tilt misalignment which leads to uneven etching and (ii) pressure non-uniformity which leads to stress concentrations and catalyst delamination (Figure 38B). In order to test the stretchability limit of the laminate composite in a bi-axial state of stress, the catalysts with different thicknesses (i.e., 20, 80,

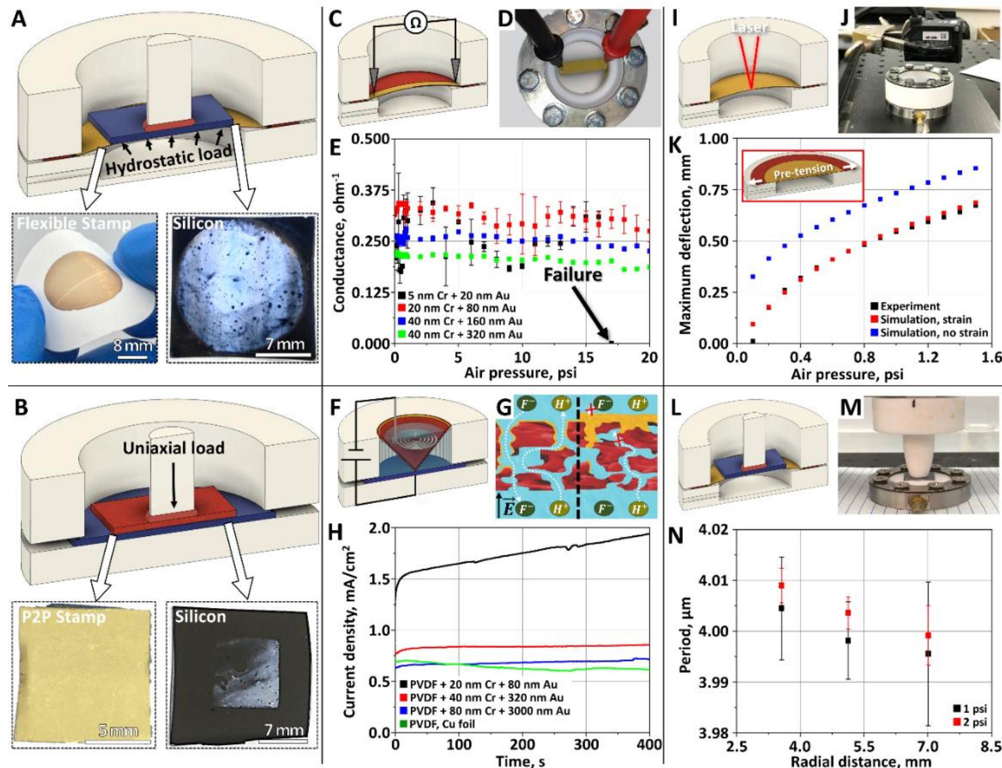

Figure 38. Test of the conformal Mac-Imprint configuration. A – Schematics of the conformal Mac-Imprint of flat Si chip and photographs of flexible and stretchable stamp (left) and imprinted Si chip (right). B – Schematics of the plate-to-plate Mac-Imprint of flat Si chip and photographs of rigid stamp (left) and Si chip imprinted with tip-and-tilt misalignment (right). C – Schematics of the catalyst stretchability test. D – Photograph of the test setup. E – Electrical conductance of the membrane as a function of catalyst thickness and applied air pressure. F – Schematics of the membrane permeability test setup. G – Schematics of the ionic movement through partially clogged membrane (left) and completely clogged membrane (right). H – Current density as a function of catalyst thickness. I – Schematics of the membrane deflection test. J – Photograph of the test setup. K – Membrane deflection in it's center as a function of applied air pressure. L – Schematics of the conformal Mac-Imprint with flat Si chip. M – Photograph of the conformal Mac-Imprint with flat Si chip. N – Variation of the imprinted pattern period as a function of the radial distance from the center of the contact point and applied air pressure.

160 and 320 nm) were deposited through a 3 mm wide shadow mask (Figure 38C and D)

to form a line through the center of the membrane. Its electrical conductance was measured as a function of catalyst layer thickness and applied hydrostatic pressure (Figure 38E). All gold-coated laminated stamp composites withstand up to 20 psi of back pressure without break of electrical contact except for the sample with the catalyst thickness of 20 nm which failed at 17 psi (Figure 38E, black dots). In all Mac-Imprint experiments performed in this study, pressures of less than 2 psi were applied to guarantee the experiments did not yield the laminated stamp composites and they remain in the elastic regime.

Concomitant with the experiment above, a mechanical finite-element model for the elastic deformation of the stamp and its clamping unit (i.e., o-ring and metal ring clamp) was first experimentally validated by measuring the membrane's free maximum deflection as a function of pressure (Figure 38I-K). The model included the non-linear elastic constants for a Neo-Hookean model of the rubber o-ring, its compression level during assembly, non-sliding boundary conditions between the membrane and its backing PI film, their Young's modulus and Poisson's ratio extracted from tensile testing, and the membrane's initial strain (i.e., prior to pressure application) induced during its attachment to the imprinting set-up obtained via digital image correction. The model accurately predicted its displacement without a single fitting parameter within the elastic limit and found the existence of stress concentrations in the membrane near its contact area with the o-ring which limits the air pressure to 1.5 psi to ensure it does not undergo plastic deformation which would be undesirable from a process repeatability standpoint.

While thicker catalysts can withstand higher operational pressures during Mac-Imprint, its thickness cannot exceed half the pore size of the membrane as it will clog them and no

longer be able to support solution diffusion. Thus, to evaluate its mass transport, a two-electrode electrochemical set-up for anodizing a silicon wafer was created and the gold-coated membrane with variable catalyst thickness placed as a 'separator' between the counter electrode (i.e., Pt coil) and the working electrode (i.e., Silicon wafer) creating a top and bottom reservoir (Figure 38, F and G). A baseline current density was measured when the membrane was replaced with a copper foil (a fully blocking separator) (Figure 38H, green) and a fixed voltage applied between counter and working electrodes. The current density observed in this case is attributed to Cu foil acting as a bipolar electrode which supports redox reactions in it's extremities *(122)* and thus allows for the charge transfer between top and bottom reservoirs of the cell without actual mass-transport. At the same applied voltage, the current density for the membrane with the highest catalyst thickness of 3000 nm was approximately equal to the of the baseline (Figure 38H, blue) suggesting lack of mass-transport through the membrane which is in agreement with completely clogged pores confirmed by SEM (Figure 48C). With the decrease of the catalyst thickness the amplitude of the current density increases which indicates ionic exchange between top and bottom reservoirs of the cell. The positive slope of the current density trends be explained by the decrease of the overall system resistivity which could be attributed to the increase of the etching media conductivity upon Si substrate dissolution.

It should be noted that upon the inflation the porous membrane will be strained which will induce radial distortions of the designed patterns that will be subsequently transferred onto the imprinted Si surface thus affecting it's designed performance. According to the measurements of the pattern period of imprinted Si surface, the strain level is highest at the

center of the contact interface and slowly decreases in the radial direction (Figure 38M). Moreover, the increase of the applied air pressure also leads to the higher strain levels. Both of the observations are in good agreement with the model predictions which paves it's future application for the reverse engineering of the membrane's patterns during it's manufacturing in order to obtain spatially uniform Mac-Imprinted patterns.

4.2.3 Conformal Mac-Imprint of Plano-Convex Si Lens

Similarly to the classical nanoimprint lithography with flexible stamps, conformal Mac-Imprint can applied to non-planar surfaces (Figure 39A) which was exploited for the first time to fabricate a positive sharklet pattern on the surface of plano-convex Si lens (Figure 39B) with the radius of curvature of 36.4 mm. The photograph of the lens demonstrates a uniform patterning of it's central portion with the area coverage of ~ 40% and a strong light diffraction (rainbow coloration along the reflected light beams) indicating high fidelity of sharklet pattern transfer as any pattern irregularity would have significantly reduced the diffraction. The pattern area coverage was not complete due to the unoptimized air pressure during conformal Mac-Imprint which lead to the incomplete contact between composite porous stamps and Si lens. This can be avoided in the future by implementing the developed mechanical model to predict maximum contact area as a function of applied pressure and lens curvature. The large-area optical profilometry of the imprinted Si lens highlighted it's curvilinear surface (Figure 39C). The high-resolution optical profilometry was able to resolve individual Sharklet pattern uniformly imprinted with >2 μm depth (Figure 39D) thus confirming high pattern transfer fidelity of the process even on a non-planar surfaces. The Raman analysis of the imprinted pattern did not reveal large deviations of the peak

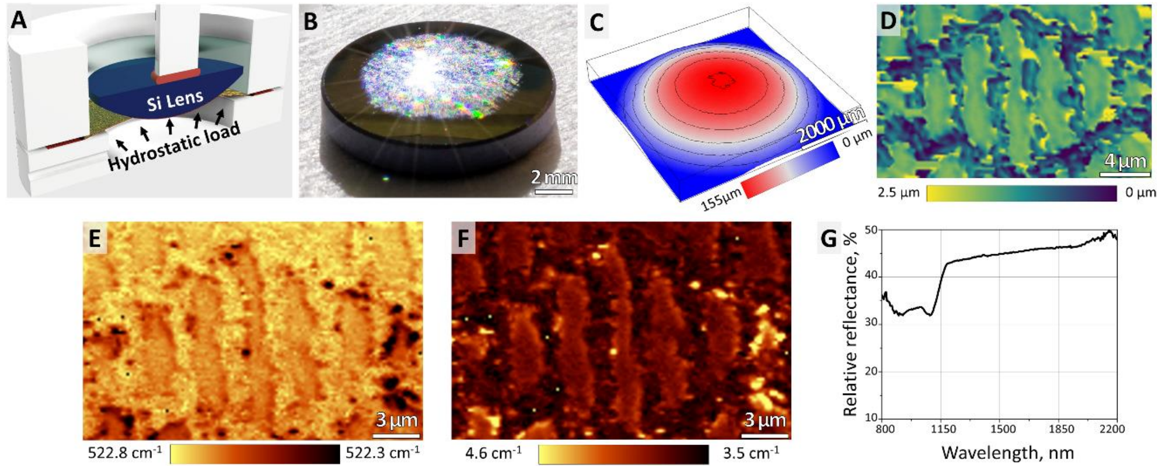

Figure 39. Conformal Mac-Imprint onto plano-convex Si lens. A – Schematics of the conformal contact to the curvilinear object. B – Photograph of the Mac-Imprinted lens. C and D – Optical profilometry of the imprinted lens. E and F – Raman peak position and full width at half-maximum, respectively. G – Hemispherical reflectance of imprinted Si lens relative to bare Si.

position (Figure 39E) or broadening of the full-width at half-maximum (Figure 39F) highlighting the limited levels of porous Si defects formation. Albeit sharklet pattern fabricated on the plane Si chip has demonstrated a 35% reduction of the hemispherical reflectance comparing to bare Si chip (Figure 36G) it could not approach the same values on the lens (Figure 39G). Such difference is explained by the IR light reflection from the back of the Si lens which has mirror finishing contrary to the bare Si chip where only imprinted surface was polished. This observation suggests that for the efficient reflection suppression both front and back sides of the Si lens have to be patterned as has been demonstrated by Kamizuka et al. *(118)*.

4.3 Conclusion

In this study a new generation of Mac-Imprint stamps was developed and implemented for the large-area conformal direct micromachining of flat and curvilinear Si

substrates without the need for it's pre-patterning. This was achieved by using water filtration PVDF membranes due to their (i) highly porous nature capable of storing and transporting etching solution and (ii) flexibility and stretchability capable of uniform contact to non-planar surfaces upon air pressure actuation. The latter was realized by designing and developing a completely new conformal Mac-Imprint system. It was demonstrated that commercially available porous PVDF membranes can be used as a stamp material for conformal Mac-Imprint of random hierarchical Si nano- and microtip surfaces which demonstrated reflectance reduction in the infrared range as well as hydrophobicity comparing to bare Si wafer. In the same time their limited flatness, macroscale variations of the pore sizes and limited patternability did not allow for the Mac-Imprint of arbitrary 3D patterns. With this goal, PVDF membranes made by TIPS casting were used to uniformly Mac-Imprint flat Si wafers with corrugated sharklet patterns with feature sizes spanning more than 2 orders of magnitude and individual details as small as sub-200 nm. To understand and predict biaxial stress and strain distribution upon the inflation of composite stamps and their contact with the substrate, a mechanical model was developed and successfully validated using experimental data with high degree of accuracy. The mechanical behavior of the thin catalyst films of the stamps was experimentally tested and the range of Mac-Imprint conditions upon which the system remains stable were established. Permeability of the porous PVDF membranes was tested as a function of the catalyst layer thickness and a range of catalyst thicknesses for un-restricted mass-transport was found. All these findings allowed for the first time for direct micromachining of plano-convex Si lenses with shraklet patterns with high pattern transfer fidelity and paved a way

towards advanced infrared lenses with bio-inspired antireflective and anti-fouling properties.

4.4. Methods

4.4.1 Substrate Preparation

Mac-Imprint of plane substrates was performed onto boron-doped Si wafers with 1-10 Ω·cm resistivity and (100) crystal orientation. Si wafers were prime grade purchased from UniversityWafer. Mac-Imprint of curvilinear substrate was performed on undoped plano-convex Si lens with radius of curvature of 36.4 mm. Si lens were purchased from ThorLabs. Prior Mac-Imprint substrates were thoroughly rinsed with acetone, isopropyl alcohol and deionized (DI) water followed by RCA-1 cleaning and another DI water rinsing before Mac-Imprint.

4.4.2 Stamp Preparation

Main requirement for the stamp's porous material was it's chemical inertness to concentrated HF acid, thus narrowing the search to the fluoropolymers due to their superior chemical stability. For the particular application in the Mac-Imprint porous PVDF stand out among other the fluoropolymers, because it's fabrication as well as micro- and nanopatterning are well studied. Thus, porous PVDF membranes (both commercial flat and TIPS patterned) with average pore size of 1 μm were used to fabricate Mac-Imprint stamps. The details of TIPS patterning protocol are described elsewhere *(113)*.

For the plate-to-plate Mac-Imprint PVDF membranes were firstly thoroughly rinsed with isopropyl alcohol and DI water followed by drying with compressed clean dry

air. After drying membranes were placed inside NSC-3000 magnetron sputter chamber at 20 cm distance from the Cr and Au targets and subsequently coated with 20 nm Cr adhesion and 80 nm Au catalytic layers. Then Au-coated PVDF membranes were cut into square pieces and attached to the equally sized Si chips using double-sided Kapton tape. The photographs of the stamps are demonstrated on Figure 37A and E.

For the conformal Mac-Imprint the membrane cleaning and drying was the same. After drying membranes were placed inside NSC-3000 magnetron sputter chamber at 20 cm distance from the Cr and Au targets and subsequently coated with 20 nm Cr adhesion and 80 nm Au catalytic layers through the circular shadow mask with 15 mm diameter opening. This step was done in order to minimize the catalyst surface area and prevent substrate porosification. Then Au-coated PVDF membranes were cut into circular pieces and laminated onto polyimide (PI) film to fit into Mac-Imprint Teflon cell. The photograph of the PVDF membrane with shadow-sputtered central area is presented on Figure 38A.

4.4.3 Mac-Imprint Conditions and Setup

The plate-to-plate Mac-Imprint setup is composed of an electrochemical cell holding Si substrate and etching solution, a PTFE rod holding Mac-Imprint stamp, a motorized linear stage bringing stamp in parallel contact with Si and a load cell measuring the forces developed upon contact. The detailed description of the Mac-Imprint set-up, protocol and critical steps (i.e. alignment between stamp and substrate) were discussed in the previous chapters of this dissertation. The contact forces were maintained below 6 lbf. The contact duration was varied from 5 to 30 minutes. Influence of the etching time on the reflectance suppression is presented on Figure 49 of APPENDIX B.

The conformal Mac-Imprint set-up is composed of an electrochemical cell holding flexible Mac-Imprint stamp and etching solution, a PTFE rod holding Si substrate, a motorized linear stage bringing Si substrate in close proximity with the stamp, an electronic pressure regulator applying air pressure to the back of the stamps to achieve conformal contact with Si substrate and a load cell measuring the forces developed upon contact (Figure 40).

The schematics of electrochemical cell for conformal Mac-Imprint is presented on Figure 40A. It consists of stainless steel base and PTFE top parts. Flexible Mac-Imprint stamp is clamped between the base and the upper part of the electrochemical cell using stainless steel washer and bolts. The chemically stable Aflas o-ring was used to prevent etching solution leakage outside the cell. The PI film of the flexible stamp was used to prevent etching solution leakage through the porous PVDF into the base of the cell. The base has a chamber, connected to the electronic pressure regulator through PVC hose.

The demonstration of conformal Mac-Imprint is presented on Figure 40B. Here, Si substrate is connected to the PTFE rod, which is backed by a load cell and attached to a vertical stepper motor stage. By setting constant displacements onto the stepper motor substrate is brought into to the close proximity with the stamp (gap ≈ 200 μm). Required air pressure is applied immediately after substrate reaches imprinting position. At the end of the imprinting process air pressure is reduced to 0 psi and substrate is brought away from the stamp into the home position. The contact forces were maintained below 1.5 lbf. The contact duration was varied from 5 to 30 minutes. Note that the electrochemical cell on Figure 40B is missing PTFE top part which was intentionally removed to capture the

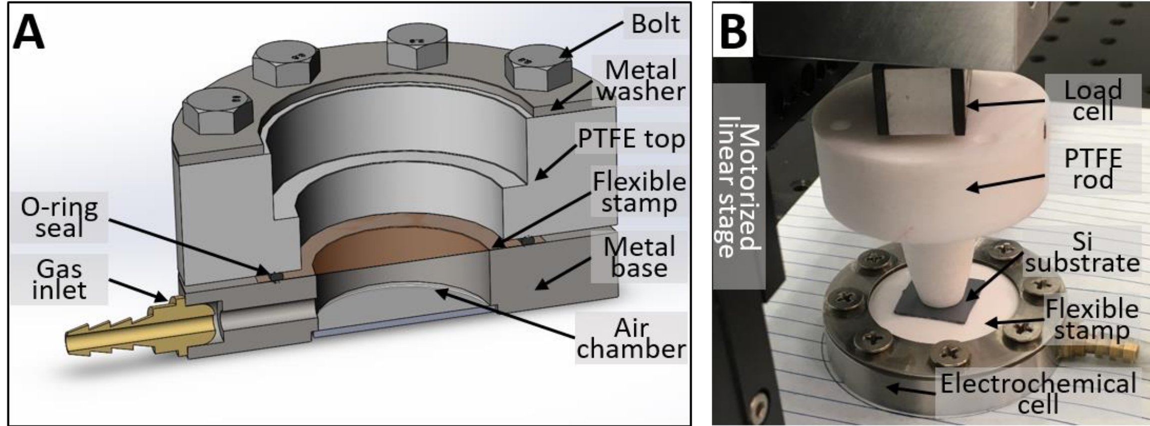

Figure 40. Conformal Mac-Imprint set-up. A – Schematics of the electrochemical cell for conformal Mac-Imprint. B – Demonstration of conformal Mac-Imprint process in dry conditions.

conformal contact between flexible stamp and Si substrate upon Mac-Imprint in dry conditions.

The etching solution with ρ equal to 95 % is prepared by mixing HF (48 % by vol.) and H_2O_2 (30 % by vol.) in the 6.5:1 ratio ($HF:H_2O_2$; by vol.). Moreover, pure ethanol is added to the etching solution (11 % of the etching solution volume) in order to improve solution's wettability. A fresh etching solution was mixed prior every Mac-Imprint operation. All chemicals were ACS grade, purchased from Sigma Aldrich.

4.4.4 Numerical Modeling

Finite element method (FEM) was employed to model the mechanical behavior of the conformal Mac-Imprint setup using static structural in commercial ANSYS software. Due to it's axisymmetric nature, a half symmetric two-dimensional geometry system was modelled (Figure 41) which composes of PTFE top part, rubber o-ring, two-layered composite stamp (PVDF and PI) and metal base. Figure 41 captures the final step of the

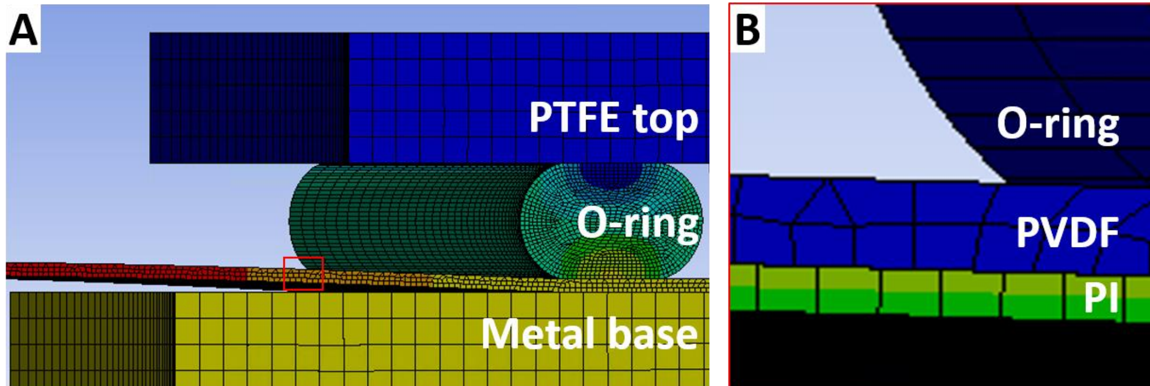

Figure 41. Screenshot of the half symmetric two-dimensional simulation geometry. A – Full-view of the simulation geometry capturing PTFE top part, compressed o-ring, composite stamp (not marked) and metal base. B – Zoom in into the composite stamp highlighting it's two-layer structure composed of PVDF (top) and PI (bottom).

simulation with compressed o-ring and inflated composite stamp. The geometries of the system components were designed in SolidWorks and then imported and assembled in 2021 ANSYS design modeler via STP files where additional adjustments were made to prepare the model for analysis. The mechanical properties of both PI and porous PVDF were extracted via uniaxial tensile testing. For the general materials such as stainless steel, silicon and PTFE, elastic constants were obtained from literature and material data sheet.

4.4.5 Morphological, Structural and Functional Characterization

Morphological properties of the Mac-Imprint stamps and imprinted waveguides were characterized by scanning electron microscopy (SEM) using Philips XL-30 FEG SEM and Zeiss Auriga FIB-SEM. Surface topology of Mac-Imprint stamps and Si was characterized by optical profilometry using the Witec Alpha 300 RA+ system. The nanoscale defects of the imprinted waveguides and surroundings were characterized by confocal Raman microscopy using the same Witec system. The Raman signal was excited

by 532 nm laser with the 0.1 mW output power. Raman signal was acquired using 1800 g/mm grating yielding 1 cm-1 spectral resolution with the accumulation time of 0.2 sec. The total hemispherical reflectance of the samples was acquired using Perkin Lambda 950 spectrophotometer with spectral resolution of 5 nm/pixel.

CHAPTER 5

DISSERTATION CONCLUSION AND FUTURE DIRECTIONS

This dissertation explores fundamental mechanisms in Mac-Imprint of monocrystalline Si with porous catalytic stamps and provides new insights into it's resolution and mass-transport limitations. Based on these findings it becomes possible to implement Mac-Imprint for the fabrication of functional optoelectronic devices. Moreover, by developing advanced Mac-Imprint stamps with etching solution storage capabilities this dissertation demonstrates significant step toward scalable fabrication of 3D metasurfaces on planar and curvilinear semiconductor substrates.

At first, this dissertation reported successful fabrication of SOI waveguides using Mac-Imprint. The mass-transport during the process was investigated and it was established that use of the porous catalysts enables etching solution diffusion in the direction perpendicular to the waveguide's propagation. This approach improved etch depth uniformity and increased EEPD to approximately 700 µm. Observed variations of the etch depth along the waveguide were attributed to the imperfections of the stamp fabrication procedure, specifically demolding issues during soft nanoimprint lithography. The porous catalyst-induced surface roughness was reduced down to 10 nm, which is in par with plasma etching, by minimizing pore size of the catalyst to within the order of magnitude of the resolution limit of Mac-Imprint. The latter, based on the data mining of existing literature, was hypothesized to be proportional to the Debye length. At these length scales, grain boundaries of the porous catalyst (i.e.,~5 nm) were transferred onto Si surface. This observation both validated the Debye length hypothesis and highlighted the necessity

for developing atomically-smooth catalysts. The Si porosification, induced by the increasing surface area of the catalyst, was mitigated by using etching solution with low H_2O_2 concentration. All of these findings allowed for the fabrication of single mode SOI rib waveguides with limited levels of sidewall scattering as was confirmed by the IR imaging.

Second, this dissertation reported the development of fully porous flexible polymer stamps designed to simultaneously store and transport etching solution for large-area conformal Mac-Imprint of flat and curvilinear substrates. The concept was firstly validated in plate-to-plate configuration with the porous PVDF (commercial and lab-made), both of which successfully imprinted it's morphologies onto the bare Si chips. The advantage of the lab-made PVDF, specifically it's patternability and flatness, was highlighted by demonstrating free-form Mac-Imprint with improved uniformity. The flexibility of porous polymers was exploited to develop a new, conformal format of Mac-Imprint. It's range of operational conditions within elastic limits was established by investigating flexible stamp's behavior during bi-axial stretching using both experimental data and mechanical modeling. These findings lead to the first demonstration of direct micromachining of hierarchical 3D patterns on the surface of plano-convex Si lens.

Future development of Mac-Imprint requires (i) minimization of the imprinted surface roughness and (ii) integration with the industrial processes for parallel micromachining. At first, both pore sizes of the stamps and it's flatness should further approach resolution limit of Mac-Imprint. In the nanoporous catalyst films it can be achieved by (i) using electrochemical dealloying in cold conditions or (ii) altering the

precursor alloy composition to either beyond binary or replacing gold with other high melting temperature metals. In porous polymer membrane stamps pores sizes can be reduced by controlling phase separation conditions, which should result in the formation of hierarchical porosity with micro-scale pores inside the body of the membrane and nano-scale on the surface. Ultimately, these two approaches should combine resulting in the fabrication of advanced stamps for large-area conformal 3D patterning of planar and non-planar substrates with unprecedented resolution in all three directions. The second direction involves process and equipment development for easy integration with commercial mask aligners and nanoimprinting technologies presently used for polymer patterning. This can be achieved by (i) modification of existing commercial equipment to handle liquids, (ii) using less hazardous chemicals to simplify equipment design and (iii) investigating demolding strategies particularly for high-aspect ratio patterns.

REFERENCES

1. N. Yu, Q. J. Wang, M. A. Kats, J. A. Fan, S. P. Khanna, L. Li, A. G. Davies, E. H. Linfield, F. Capasso, Designer spoof surface plasmon structures collimate terahertz laser beams. *Nat. Mater.* **9**, 730–735 (2010).

2. E. Arbabi, A. Arbabi, S. M. Kamali, Y. Horie, A. Faraon, Multiwavelength polarization-insensitive lenses based on dielectric metasurfaces with meta-molecules. *Optica* **3**, 628 (2016).

3. L. H. Gabrielli, D. Liu, S. G. Johnson, M. Lipson, On-chip transformation optics for multimode waveguide bends. *Nat. Commun.* **3**, 1217 (2012).

4. A. Xie, L. Zhou, J. Chen, X. Li, Efficient silicon polarization rotator based on mode-hybridization in a double-stair waveguide. *Opt. Express* **23**, 3960 (2015).

5. D. H. Ko, J. R. Tumbleston, K. J. Henderson, L. E. Euliss, J. M. Desimone, R. Lopez, E. T. Samulski, Biomimetic microlens array with antireflective "moth-eye" surface. *Soft Matter* **7**, 6404–6407 (2011).

6. P. Wang, N. Mohammad, R. Menon, Chromatic-aberration-corrected diffractive lenses for ultra- broadband focusing. *Sci. Rep.* **6**, 1–7 (2016).

7. Y. Hu, X. Luo, Y. Chen, Q. Liu, X. Li, Y. Wang, N. Liu, H. Duan, 3D-Integrated metasurfaces for full-colour holography. *Light Sci. Appl.* **8**, 86 (2019).

8. K. Keskinbora, C. Grévent, M. Hirscher, M. Weigand, G. Schütz, Single-Step 3D Nanofabrication of Kinoform Optics via Gray-Scale Focused Ion Beam Lithography for Efficient X-Ray Focusing. *Adv. Opt. Mater.* **3**, 792–800 (2015).

9. N. Mojarad, M. Hojeij, L. Wang, J. Gobrecht, Y. Ekinci, Single-digit-resolution nanopatterning with extreme ultraviolet light for the 2.5 nm technology node and beyond. *Nanoscale* **7**, 4031–4037 (2015).

10. R. A. Gottscho, Microscopic uniformity in plasma etching. *J. Vac. Sci. Technol. B Microelectron. Nanom. Struct.* **10**, 2133 (1992).

11. J. Yeom, Y. Wu, J. C. Selby, M. A. Shannon, Maximum achievable aspect ratio in deep reactive ion etching of silicon due to aspect ratio dependent transport and the microloading effect. *J. Vac. Sci. Technol. B Microelectron. Nanom. Struct.* **23**, 2319

(2005).

12. W. X. Su, C. Y. Wu, Y. C. Lee, Anti-reflection nano-structures fabricated on curved surface of glass lens based on metal contact printing lithography. *Microelectron. Eng.* **214**, 15–20 (2019).

13. T. Kamizuka, T. Miyata, S. Sako, H. Imada, T. Nakamura, K. Asano, M. Uchiyama, K. Okada, T. Wada, T. Nakagawa, T. Onaka, I. Sakon, Development of high-throughput silicon lens and grism with moth-eye antireflection structure for mid-infrared astronomy. *Mod. Technol. Space- Ground-based Telesc. Instrum. II* **8450**, 845051 (2012).

14. K. S. Chen, A. A. Ayón, X. Zhang, S. M. Spearing, Effect of process parameters on the surface morphology and mechanical performance of silicon structures after deep reactive ion etching (DRIE). *J. Microelectromechanical Syst.* **11**, 264–275 (2002).

15. R. Abdolvand, F. Ayazi, An advanced reactive ion etching process for very high aspect-ratio sub-micron wide trenches in silicon. *Sensors Actuators, A Phys.* **144**, 109–116 (2008).

16. K. K. Lee, D. R. Lim, H. C. Luan, A. Agarwal, J. Foresi, L. C. Kimerling, Effect of size and roughness on light transmission in a waveguide: Experiments and model. *Appl. Phys. Lett.* **77**, 1617–1619 (2000).

17. K. K. Lee, D. R. Lim, L. C. Kimerling, J. Shin, F. Cerrina, Fabrication of ultralow-loss Si/SiO_2 waveguides by roughness reduction. *Opt. Lett.* **26**, 1888 (2001).

18. S. Y. Chou, P. R. Krauss, W. Zhang, L. Guo, L. Zhuang, Sub-10 nm imprint lithography and applications. *Annu. Device Res. Conf. Dig.* **2897**, 90–91 (1997).

19. M. R. Belegratis, V. Schmidt, D. Nees, B. Stadlober, P. Hartmann, Diatom-inspired templates for 3D replication: Natural diatoms versus laser written artificial diatoms. *Bioinspiration and Biomimetics* **9**, 016004 (2014).

20. B. P. Azeredo, Y. Lin, A. Avagyan, M. Sivaguru, K. Hsu, Direct Imprinting of Porous Silicon via Metal-Assisted Chemical Etching. *Adv. Funct. Mater.* **26**, 2929–2939 (2016).

21. J. Zhang, L. Zhang, L. Han, Z. W. Tian, Z. Q. Tian, D. Zhan, Electrochemical nanoimprint lithography: When nanoimprint lithography meets metal assisted chemical etching. *Nanoscale* **9**, 7476–7482 (2017).

22. X. Li, P. W. Bohn, Metal-assisted chemical etching in HF / H2O2 produces porous silicon. *Appl. Phys. Lett.* **77**, 2572–2574 (2000).

23. S. Bastide, E. Torralba, M. Halbwax, S. Le Gall, E. Mpogui, C. Cachet-Vivier, V. Magnin, J. Harari, D. Yarekha, J.-P. Vilcot, 3D Patterning of Si by Contact Etching With Nanoporous Metals. *Front. Chem.* **7**, 256 (2019).

24. A. Sharstniou, S. Niauzorau, P. M. Ferreira, B. P. Azeredo, Electrochemical nanoimprinting of silicon. *PNAS* **116**, 10264–10269 (2019).

25. A. Sharstniou, S. Niauzorau, A. L. Hardison, M. Puckett, J. D. Ryckman, B. P. Azeredo, Roughness suppression in electrochemical nanoimprinting of Si for applications in silicon photonics. *Adv. Mater.* , 2206608 (2022).

26. E. Torralba, M. Halbwax, T. El, M. Fouchier, V. Magnin, J. Harari, J. Vilcot, S. Le, R. Lachaume, C. Cachet-vivier, S. Bastide, 3D patterning of silicon by contact etching with anodically biased nanoporous gold electrodes. *Electrochem. commun.* **76**, 79–82 (2017).

27. J. H. Shin, H. J. Choi, G. T. Kim, J. H. Choi, H. Lee, Fabrication of nanosized antireflection patterns on surface of aspheric lens substrate by nanoimprint lithography. *Appl. Phys. Express* **6**, 3–6 (2013).

28. T. Sugita, C. L. Lee, S. Ikeda, M. Matsumura, Formation of through-holes in Si wafers by using anodically polarized needle electrodes in HF solution. *ACS Appl. Mater. Interfaces* **3**, 2417–2424 (2011).

29. G. Liu, K. L. Young, X. Liao, M. L. Personick, C. A. Mirkin, Anisotropic nanoparticles as shape-directing catalysts for the chemical etching of silicon. *J. Am. Chem. Soc.* **135**, 12196–12199 (2013).

30. D. Dimova-Malinovska, M. Sendova-Vassileva, N. Tzenov, M. Kamenova, Preparation of thin porous silicon layers by stain etching. *Thin Solid Films* **297**, 9–12 (1997).

31. C. Chartier, S. Bastide, C. Lévy-Clément, Metal-assisted chemical etching of silicon in HF-H2O2. *Electrochim. Acta* **53**, 5509–5516 (2008).

32. K. W. Kolasinski, The mechanism of galvanic/metal-assisted etching of silicon. *Nanoscale Res. Lett.* **9**, 1–8 (2014).

33. Z. Huang, N. Geyer, P. Werner, J. De Boor, U. Gösele, Metal-assisted chemical etching of silicon: A review. *Adv. Mater.* **23**, 285–308 (2011).

34. N. Geyer, B. Fuhrmann, Z. Huang, J. De Boor, H. S. Leipner, P. Werner, Model for the mass transport during metal-assisted chemical etching with contiguous metal films as catalysts. *J. Phys. Chem. C* **116**, 13446–13451 (2012).

35. L. Li, Y. Liu, X. Zhao, Z. Lin, C. Wong, Uniform Vertical Trench Etching on Silicon with High Aspect Ratio by Metal-Assisted Chemical Etching Using Nanoporous Catalysts. *ACS Appl. Mater. Interfaces* **6**, 575–584 (2014).

36. L. Li, X. Zhao, C. P. Wong, Deep etching of single- and polycrystalline silicon with high speed, high aspect ratio, high uniformity, and 3D complexity by electric bias-attenuated metal-assisted chemical etching (EMaCE). *ACS Appl. Mater. Interfaces* **6**, 16782–16791 (2014).

37. L. Li, C. C. Tuan, C. Zhang, Y. Chen, G. Lian, C. P. Wong, Uniform Metal-Assisted Chemical Etching for Ultra-High-Aspect-Ratio Microstructures on Silicon. *J. Microelectromechanical Syst.* **28**, 143–153 (2019).

38. K. Peng, Y. Wu, H. Fang, X. Zhong, Y. Xu, J. Zhu, Uniform, Axial-Orientation Alignment of One-Dimensional Single-Crystal Silicon Nanostructure Arrays. *Angew. Chemie* **117**, 2797–2802 (2005).

39. K. Peng, J. Hu, Y. Yan, Y. Wu, H. Fang, Y. Xu, S. Lee, J. Zhu, Fabrication of single-crystalline silicon nanowires by scratching a silicon surface with catalytic metal particles. *Adv. Funct. Mater.* **16**, 387–394 (2006).

40. P. Werner, C. C. Büttner, L. Schubert, G. Gerth, N. D. Zakarov, U. Gösele, Gold-enhanced oxidation of silicon nanowires. *Zeitschrift fuer Met. Res. Adv. Tech.* **98**, 1066–1070 (2007).

41. O. J. Hildreth, W. Lin, C. P. Wong, Effect of catalyst shape and etchant composition on etching direction in metal-assisted chemical etching of silicon to fabricate 3D nanostructures. *ACS Nano* **3**, 4033–4042 (2009).

42. Y. Chen, C. Zhang, L. Li, C. C. Tuan, F. Wu, X. Chen, J. Gao, Y. Ding, C. P. Wong, Fabricating and Controlling Silicon Zigzag Nanowires by Diffusion-Controlled Metal-Assisted Chemical Etching Method. *Nano Lett.* **17**, 4304–4310 (2017).

43. T. K. Kim, J. H. Bae, J. Kim, Y. C. Kim, S. Jin, D. W. Chun, Bulk

micromachining of Si by annealing-driven magnetically guided metal-assisted chemical etching. *ACS Appl. Electron. Mater.* **2**, 260–267 (2020).

44. O. J. Hildreth, D. Brown, C. P. Wong, 3D out-of-plane rotational etching with pinned catalysts in metal-assisted chemical etching of silicon. *Adv. Funct. Mater.* **21**, 3119–3128 (2011).

45. K. Rykaczewski, O. J. Hildreth, C. P. Wong, A. G. Fedorov, J. H. J. Scott, Guided three-dimensional catalyst folding during metal-assisted chemical etching of silicon. *Nano Lett.* **11**, 2369–2374 (2011).

46. C. Q. Lai, H. Cheng, W. K. Choi, C. V. Thompson, Mechanics of catalyst motion during metal assisted chemical etching of silicon. *J. Phys. Chem. C* **117**, 20802–20809 (2013).

47. C. Chang, A. Sakdinawat, Ultra-high aspect ratio high-resolution nanofabrication for hard X-ray diffractive optics. *Nat. Commun.* **5**, 1–7 (2014).

48. L. Romano, M. Kagias, J. Vila-Comamala, K. Jefimovs, L. T. Tseng, V. A. Guzenko, M. Stampanoni, Metal assisted chemical etching of silicon in the gas phase: A nanofabrication platform for X-ray optics. *Nanoscale Horizons* **5**, 869–879 (2020).

49. T. Fukushima, A. Ohnaka, M. Takahashi, H. Kobayashi, Fabrication of low reflectivity poly-crystalline Si surfaces by structure transfer method. *Electrochem. Solid-State Lett.* **14**, 98–101 (2011).

50. M. Takahashi, T. Fukushima, Y. Seino, W.-B. Kim, K. Imamura, H. Kobayashi, Surface Structure Chemical Transfer Method for Formation of Ultralow Reflectivity Si Surfaces. *J. Electrochem. Soc.* **160**, H443–H445 (2013).

51. L. Zhang, J. Zhang, D. Yuan, L. Han, J. Z. Zhou, Z. W. Tian, Z. Q. Tian, D. Zhan, Electrochemical nanoimprint lithography directly on n-type crystalline silicon (111) wafer. *Electrochem. commun.* **75**, 1–4 (2017).

52. H. Li, J. Niu, G. Wang, E. Wang, C. Xie, Direct Production of Silicon Nanostructures with Electrochemical Nanoimprinting. *ACS Appl. Electron. Mater.* **1**, 1070–1075 (2019).

53. Q. Meng, L. Han, H. Xu, X. Lin, J. Zhang, Y. Peng, J. Su, Large-area homogeneous corrosion process for electrochemical nanoimprint lithography on GaAs wafer by modulating contact pressure. *J. Electroanal. Chem.* **908**, 116097 (2022).

54. H. Xu, L. Han, J. J. Su, Z. Q. Tian, D. Zhan, Spatially-separated and photo-enhanced semiconductor corrosion processes for high-efficient and contamination-free electrochemical nanoimprint lithography. *Sci. China Chem.* **65**, 810–820 (2022).

55. L. Chrostowski, M. Hochberg, *Silicon Photonics Design: From Device to System* (Cambridge University Press, 2015).

56. W. Bogaerts, R. Baets, P. Dumon, V. Wiaux, S. Beckx, D. Taillaert, B. Luyssaert, J. Van Campenhout, P. Bienstman, D. Van Thourhout, Nanophotonic waveguides in silicon-on-insulator fabricated with CMOS technology. *J. Light. Technol.* **23**, 401–412 (2005).

57. D. Taillaert, F. Van Laere, M. Ayre, W. Bogaerts, D. Van Thourhout, P. Bienstman, R. Baets, Grating couplers for coupling between optical fibers and nanophotonic waveguides. *Japanese J. Appl. Physics, Part 1 Regul. Pap. Short Notes Rev. Pap.* **45**, 6071–6077 (2006).

58. Y. Tang, Z. Wang, L. Wosinski, U. Westergren, S. He, Highly efficient nonuniform grating coupler for silicon-on-insulator nanophotonic circuits. *Opt. Lett.* **35**, 1290 (2010).

59. D. Benedikovic, C. Alonso-Ramos, P. Cheben, J. H. Schmid, S. Wang, D.-X. Xu, J. Lapointe, S. Janz, R. Halir, A. Ortega-Moñux, J. G. Wangüemert-Pérez, I. Molina-Fernández, J.-M. Fédéli, L. Vivien, M. Dado, High-directionality fiber-chip grating coupler with interleaved trenches and subwavelength index-matching structure. *Opt. Lett.* **40**, 4190 (2015).

60. C. Li, H. Zhang, M. Yu, G. Q. Lo, CMOS-compatible high efficiency double-etched apodized waveguide grating coupler. *Opt. Express* **21**, 7868 (2013).

61. R. Takei, M. Suzuki, E. Omoda, S. Manako, T. Kamei, M. Mori, Y. Sakakibara, Silicon knife-edge taper waveguide for ultralow-loss spot-size converter fabricated by photolithography. *Appl. Phys. Lett.* **102**, 101108 (2013).

62. J. Garnett, J. Valentine, Maxwell fisheye lens as a waveguide crossing for integrated photonics. *CLEO Appl. Technol.* , JW4A.88 (2012).

63. N. Sakib, J. D. Ryckman, Design of ultra-small mode area all-dielectric waveguides exploiting the vectorial nature of light. *Opt. Lett.* **45**, 4730 (2020).

64. F. Bin Tarik, J. D. Ryckman, Fabrication tolerant coupling between silicon strip

and subdiffraction V-groove waveguides. *Opt. Contin.* **1**, 453 (2022).

65. F. Bin Tarik, A. Famili, Y. Lao, J. D. Ryckman, Robust optical physical unclonable function using disordered photonic integrated circuits. *Nanophotonics* **9**, 2817–2828 (2020).

66. S. Y. Chou, C. Keimel, J. Gu, Ultrafast and direct imprint of nanostructures in silicon. *Nature* **417**, 835–837 (2002).

67. J. D. Ryckman, M. Liscidini, J. E. Sipe, S. M. Weiss, Direct imprinting of porous substrates. *Nano Lett.* **11**, 1857–1862 (2011).

68. S. Niauzorau, A. Sharstniou, V. K. Sampath, N. Kublik, H. Bandarenka, B. Azeredo, Electroless Dealloying of Thin-Film Nanocrystalline Au–Ag Alloys: Mechanisms of Ligament Nucleation and Sources of Its Synthesis Variability. *ACS Appl. Mater. Interfaces* **14**, 17927–17939 (2022).

69. N. Van Toan, N. Inomata, M. Toda, T. Ono, Ion transport by gating voltage to nanopores produced via metal-assisted chemical etching method. *Nanotechnology* **29**, 195301 (2018).

70. H. L. Weissberg, Effective Diffusion Coefficient in Porous Media. *J. Appl. Phys.* **34**, 2636–2639 (1963).

71. M. Liang, C. Fu, B. Xiao, L. Luo, Z. Wang, A fractal study for the effective electrolyte diffusion through charged porous media. *Int. J. Heat Mass Transf.* **137**, 365–371 (2019).

72. K. Kim, B. Ki, K. Choi, S. Lee, J. Oh, Resist-Free Direct Stamp Imprinting of GaAs via Metal-Assisted Chemical Etching. *ACS Appl. Mater. Interfaces* **11**, 13574–13580 (2019).

73. W. Jiang, Y. Ding, H. Liu, B. Lu, Y. Shi, J. Shao, L. Yin, Two-Step curing method for demoulding in UV nanoimprint lithography. *Microelectron. Eng.* **85**, 458–464 (2008).

74. H. Schift, Nanoimprint lithography: An old story in modern times? A review. *J. Vac. Sci. Technol. B Microelectron. Nanom. Struct.* **26**, 458 (2008).

75. M. Li, Y. Chen, W. Luo, X. Cheng, Interfacial interactions during demolding

in nanoimprint lithography. *Micromachines* **12**, 349 (2021).

76. Y. Nakato, K. Ueda, H. Yano, H. Tsubomura, Effect of microscopic discontinuity of metal overlayers on the photovoltages in metal-coated semiconductor-liquid junction photoelectrochemical cells for efficient solar energy conversion. *J. Phys. Chem.* **92**, 2316–2324 (1988).

77. J. Chai, F. Huo, Z. Zheng, L. R. Giam, W. Shim, C. A. Mirkin, Scanning probe block copolymer lithography. *Proc. Natl. Acad. Sci. U. S. A.* **107**, 20202–20206 (2010).

78. L. H. Qian, M. W. Chen, Ultrafine nanoporous gold by low-temperature dealloying and kinetics of nanopore formation. *Appl. Phys. Lett.* **91**, 083105 (2007).

79. J. Snyder, P. Asanithi, A. B. Dalton, J. Erlebacher, Stabilized nanoporous metals by dealloying ternary alloy precursors. *Adv. Mater.* **20**, 4883–4886 (2008).

80. J. Snyder, K. Livi, J. Erlebacher, Dealloying Silver/Gold Alloys in Neutral Silver Nitrate Solution: Porosity Evolution, Surface Composition, and Surface Oxides. *J. Electrochem. Soc.* **155**, C464 (2008).

81. Q. Chen, K. Sieradzki, Spontaneous evolution of bicontinuous nanostructures in dealloyed Li-based systems. *Nat. Mater.* **12**, 1102–1106 (2013).

82. E. Torralba, S. Le Gall, R. Lachaume, V. Magnin, J. Harari, M. Halbwax, J. P. Vilcot, C. Cachet-Vivier, S. Bastide, Tunable Surface Structuration of Silicon by Metal Assisted Chemical Etching with Pt Nanoparticles under Electrochemical Bias. *ACS Appl. Mater. Interfaces* **8**, 31375–31384 (2016).

83. H. Shang, D. Sun, P. Yu, B. Wang, T. Yu, T. Li, H. Jiang, Scattering Loss of Silicon-on-Insulator Waveguides. *Coatings* **10**, 236 (2020).

84. E. Pinna, S. Le Gall, E. Torralba, G. Mula, C. Cachet-Vivier, S. Bastide, Mesopore Formation and Silicon Surface Nanostructuration by Metal-Assisted Chemical Etching With Silver Nanoparticles. *Front. Chem.* **8**, 658 (2020).

85. N. Geyer, B. Fuhrmann, H. S. Leipner, P. Werner, Ag-mediated charge transport during metal-assisted chemical etching of silicon nanowires. *ACS Appl. Mater. Interfaces* **5**, 4302–4308 (2013).

86. M. O. Williams, D. Hiller, T. Bergfeldt, M. Zacharias, How the Oxidation

Stability of Metal Catalysts Defines the Metal-Assisted Chemical Etching of Silicon. *J. Phys. Chem. C* **121**, 9296–9299 (2017).

87. E. Anastassakis, A. Pinczuk, E. Burstein, F. H. Pollak, M. Cardona, Effect of static uniaxial stress on the Raman spectrum of silicon. *Solid State Commun.* **88**, 1053–1058 (1993).

88. H. Münder, C. Andrzejak, M. G. Berger, U. Klemradt, H. Lüth, R. Herino, M. Ligeon, A detailed Raman study of porous silicon. *Thin Solid Films* **221**, 27–33 (1992).

89. J. E. Smith, M. H. Brodsky, B. L. Crowder, M. I. Nathan, A. Pinczuk, Raman spectra of amorphous Si and related tetrahedrally bonded semiconductors. *Phys. Rev. Lett.* **26**, 642–646 (1971).

90. T. Iida, T. Itoh, D. Noguchi, Y. Takanashi, Y. Takano, Y. Kanda, Residual lattice strain in thin silicon-on-insulator bonded wafers: Effects on electrical properties and raman shifts. *J. Appl. Phys.* **89**, 2109–2114 (2001).

91. M. A. Tran, D. Huang, T. Komljenovic, J. Peters, A. Malik, J. E. Bowers, Ultra-low-loss silicon waveguides for heterogeneously integrated silicon/III-V photonics. *Appl. Sci.* **8**, 1139 (2018).

92. A. Sharstniou, S. Niauzorau, A. Junghare, B. P. Azeredo, Metal-Assisted Electrochemical Nanoimprinting of Porous and Solid Silicon Wafers. *JoVE* , e61040 (2022).

93. D. Qin, Y. Xia, G. M. Whitesides, Soft lithography for micro- and nanoscale patterning. *Nat. Protoc.* **5**, 491–502 (2010).

94. J. Stuckner, K. Frei, I. McCue, M. J. Demkowicz, M. Murayama, AQUAMI: An open source Python package and GUI for the automatic quantitative analysis of morphologically complex multiphase materials. *Comput. Mater. Sci.* **139**, 320–329 (2017).

95. M. Haeri, M. Haeri, ImageJ Plugin for Analysis of Porous Scaffolds used in Tissue Engineering. *J. Open Res. Softw.* **3**, 2–5 (2015).

96. S. J. Wilson, M. C. Hutley, The Optical Properties of "Moth Eye" Antireflection Surfaces. *Opt. Acta Int. J. Opt.* **29**, 993–1009 (1982).

97. J. T. Decker, C. M. Magin, C. J. Long, J. A. Finlay, M. E. Callow, J. A. Callow,

A. B. Brennan, Engineered antifouling microtopographies: An energetic model that predicts cell attachment. *Langmuir* **29**, 13023–13030 (2013).

98. D. Wu, J. N. Wang, L. G. Niu, X. L. Zhang, S. Z. Wu, Q. D. Chen, L. P. Lee, H. B. Sun, Bioinspired fabrication of high-quality 3D artificial compound eyes by voxel-modulation femtosecond laser writing for distortion-free wide-field-of-view imaging. *Adv. Opt. Mater.* **2**, 751–758 (2014).

99. M. Kowalczyk, J. Haberko, P. Wasylczyk, Microstructured gradient-index antireflective coating fabricated on a fiber tip with direct laser writing. *Opt. Express* **22**, 12545 (2014).

100. Y. Suzuki, K. Suzuki, M. Michihata, K. Takamasu, S. Takahashi, One-shot stereolithography for biomimetic micro hemisphere covered with relief structure. *Precis. Eng.* **54**, 353–360 (2018).

101. K. H. Jeong, J. Kim, L. P. Lee, Biologically inspired artificial compound eyes. *Science (80-.).* **312**, 557–561 (2006).

102. Y. W. Kwon, J. Park, T. Kim, S. H. Kang, H. Kim, J. Shin, S. Jeon, S. W. Hong, Flexible Near-Field Nanopatterning with Ultrathin, Conformal Phase Masks on Nonplanar Substrates for Biomimetic Hierarchical Photonic Structures. *ACS Nano* **10**, 4609–4617 (2016).

103. H. K. Raut, V. A. Ganesh, A. S. Nair, S. Ramakrishna, Anti-reflective coatings: A critical, in-depth review. *Energy Environ. Sci.* **4**, 3779–3804 (2011).

104. X. Wang, W. Wang, H. Shao, S. Chao, H. Zhang, C. Tang, X. Li, Y. Zhu, J. Zhang, X. Zhang, Y. Lu, Lunar Dust-Mitigation Behavior of Aluminum Surfaces with Multiscale Roughness Prepared by a Composite Etching Method. *ACS Appl. Mater. Interfaces* **14**, 34020–34028 (2022).

105. J. Yeom, M. A. Shannon, Detachment lithography of photosensitive polymers: A route to fabricating three-Dimensional structures. *Adv. Funct. Mater.* **20**, 289–295 (2010).

106. W. R. Childs, R. G. Nuzzo, Patterning of thin-film microstructures on non-planar substrate surfaces using decal transfer lithography. *Adv. Mater.* **16**, 1323–1327 (2004).

107. C. M. Waits, B. Morgan, M. Kastantin, R. Ghodssi, Microfabrication of 3D

silicon MEMS structures using gray-scale lithography and deep reactive ion etching. *Sensors Actuators A Phys.* **119**, 245–253 (2005).

108. F. Liu, N. A. Hashim, Y. Liu, M. R. M. Abed, K. Li, Progress in the production and modification of PVDF membranes. *J. Memb. Sci.* **375**, 1–27 (2011).

109. A. Marmur, The lotus effect: Superhydrophobicity and metastability. *Langmuir* **20**, 3517–3519 (2004).

110. K.-C. Park, H. J. Choi, C.-H. Chang, R. E. Cohen, G. H. McKinley, G. Barbastathis, Nanotextured Silica Surfaces with Robust Superhydrophobicity and Omnidirectional Broadband Supertransmissivity. *ACS Nano* **6**, 3789–3799 (2012).

111. C. H. Sun, P. Jiang, B. Jiang, Broadband moth-eye antireflection coatings on silicon. *Appl. Phys. Lett.* **92**, 1–4 (2008).

112. Y. Ding, S. Maruf, M. Aghajani, A. R. Greenberg, Surface patterning of polymeric membranes and its effect on antifouling characteristics. *Sep. Sci. Technol.* **52**, 240–257 (2017).

113. S. Fan, M. Aghajani, M. Wang, J. Martinez, Y. Ding, Patterning flat-sheet Poly(vinylidene fluoride) membrane using templated thermally induced phase separation. *J. Memb. Sci.* **616**, 118627 (2020).

114. Y. Nishijima, R. Komatsu, S. Ota, G. Seniutinas, A. Balčytis, S. Juodkazis, Anti-reflective surfaces : Cascading nano / microstructuring. *Apl Photonics* **1**, 076104 (2016).

115. N. Shanmugam, R. Pugazhendhi, R. M. Elavarasan, P. Kasiviswanathan, N. Das, Anti-reflective coating materials: A holistic review from PV perspective. *Energies* **13**, 2631 (2020).

116. B. P. Azeredo, J. Sadhu, J. Ma, K. Jacobs, J. Kim, K. Lee, J. H. Eraker, X. Li, S. Sinha, N. Fang, P. Ferreira, K. Hsu, Silicon nanowires with controlled sidewall profile and roughness fabricated by thin-film dewetting and metal-assisted chemical etching. *Nanotechnology* **24**, 225305–225312 (2013).

117. Y. F. Huang, S. Chattopadhyay, Y. J. Jen, C. Y. Peng, T. A. Liu, Y. K. Hsu, C. L. Pan, H. C. Lo, C. H. Hsu, Y. H. Chang, C. S. Lee, K. H. Chen, L. C. Chen, Improved broadband and quasi-omnidirectional anti-reflection properties with biomimetic silicon nanostructures. *Nat. Nanotechnol.* **2**, 770–774 (2007).

118. T. Kamizuka, T. Miyata, S. Sako, H. Imada, R. Ohsawa, K. Asano, M. Uchiyama, K. Okada, M. Uchiyama, T. Wada, T. Nakagawa, T. Nakamura, I. Sakon, T. Onaka, Development of high-throughput silicon lens and grism with moth-eye anti-reflection structure. *Adv. Opt. Mech. Technol. Telesc. Instrum.* **9151**, 1850–1857 (2014).

119. J. A. Rogers, T. Someya, Y. Huang, Materials and Mechanics for Stretchable Electronics. **327**, 1603–1608 (2010).

120. R. Ji, M. Hornung, M. A. Verschuuren, R. van de Laar, J. van Eekelen, U. Plachetka, M. Moeller, C. Moormann, UV enhanced substrate conformal imprint lithography (UV-SCIL) technique for photonic crystals patterning in LED manufacturing. *Microelectron. Eng.* **87**, 963–967 (2010).

121. J. Chen, C. Gu, H. Lin, S.-C. Chen, Soft mold-based hot embossing process for precision imprinting of optical components on non-planar surfaces. *Opt. Express* **23**, 20977 (2015).

122. S. E. Fosdick, K. N. Knust, K. Scida, R. M. Crooks, Bipolar electrochemistry. *Angew. Chemie - Int. Ed.* **52**, 10438–10456 (2013).

123. D. G. Stavenga, S. Foletti, G. Palasantzas, K. Arikawa, Light on the moth-eye corneal nipple array of butterflies. *Proc. R. Soc. B Biol. Sci.* **273**, 661–667 (2006).

124. L. Wen, J. C. Weaver, G. V. Lauder, Biomimetic shark skin: Design, fabrication and hydrodynamic function. *J. Exp. Biol.* **217**, 1656–1666 (2014).

APPENDIX A

ROUGHNESS REDUCTION IN ELECTROCHEMICAL NANOIMPRINTING OF SI WITH NANOPOROUS CATALYSTS

Debye length (Electrical Double Layer thickness) calculation

Debye length (κ^{-1}) of the ES is calculated according to the formula 1:

$$\kappa^{-1} = \sqrt{\frac{\varepsilon_0 \varepsilon_r k_b T}{2 \cdot 10^3 N_A e^2 I}} \quad (1)$$

Where ε_0 – free dielectric constant (8.8541878128*10^{-12}, F*m^{-1}), ε_r - dielectric constant (84, relative to free dielectric constant), k_b – Boltzmann constant (1.380649*10^{-23}, J*K^{-1}), T – temperature (300, K), N_A – Avogadro number (6.02214076*10^{23}, mol^{-1}), e – charge of electron (1.602176634*10^{-19}, C) and I – ionic strength of the ES. I is calculated according to the formula 2:

$$I = \frac{1}{2}\sum_{i=1}^{n} c_i z_i^2 \quad (2)$$

Where c_i – concentration of i ions and z_i – charge of i ions. Additionally, c_i is calculated according to the formula 3:

$$c_i = \sqrt{[i] \cdot K_{D_i}} \quad (3)$$

Where $[i]$ – molar concentration of component i and K_{D_i} – dissociation constant of component i

The ES solution was composed of 2.06 ml of 48% HF acid, 0.03 ml of 30% H_2O_2 and 0.2 ml of 99.99% C_2H_6O. Thus, the molar concentrations of HF and H_2O_2 were calculated to be 25.33759523 and 0.127096347 mol/L, respectively. Molar concentrations of H_2O and C_2H_6O were not calculated because at room temperature $K_{D_{H_2O}}$ and $K_{D_{C_2H_6O}}$

are 10^{-14} and 10^{-16} respectively and thus will not significantly affect the ionic strength of the solution.

Next, HF acid dissociates onto $[H^{+}]$ and $[F^{-}]$ with $K_{D_{HF}} = 7.2 \cdot 10^{-4}$. Similarly, H_2O_2 dissociates onto $[H^{+}]$ and $[O_2H^{-}]$ with $K_{D_{H_2O_2}} = 2 \cdot 10^{-12}$. The molar concentrations of these ions were calculated according to formula (3) and summarized in the Table 1.

Table 1. Calculated ionic concentrations of the major ionic species

Ionic species	$[H^{+}]$	$[F^{-}]$	$[H^{+}]$	$[O_2H^{-}]$
Molar concentration, present paper	0.135066904	0.135066904	5.04175E-07	5.04175E-07
Molar concentration, Liu et al.*(29)*	0.135780291	0.135780291	1.32814E-06	1.32814E-06

Based on the values from Table 1, ionic strength of the ES was calculated for both present paper and Liu et al.*(29)* using the formula (2) and was equal to $I_{pres} = 0.1350674$ and $I_{[1]} = 0.1357816$, respectively.

Finally, the Debye length of the ES was calculated using the formula (1) and was equal to $\kappa_{pres}^{-1} = 8.58895^{-10}\ m$ and $\kappa_{[1]}^{-1} = 8.56633^{-10}\ m$

The analysis of Si overetching from Liu et al.*(29)*

Table 2. Summary of the data reported in Liu et al.*(29)* and calculated overetching

Au, nm	4	5	7.2	9.5	13.6	14.9	19.6	21.5	25.5
Si, nm	5	5.7	7.4	9.6	14.4	17.9	22.6	23.8	25.6
φ, nm	1	0.7	0.2	0.1	0.8	3	3	2.3	0.1

The average overetching, $\bar{\varphi}$ was equal to 1.24 nm. The standard deviation σ was calculated according to the formula: $\sigma = \sqrt{\frac{\sum(\varphi-\bar{\varphi})^2}{(n-1)}}$ and was equal to 1.20 nm.

AFM analysis of stamp and imprinted Si

In order to support the hypothesis that the irregular etch depth profile presented on Figure 20B is caused by the imperfections of the stamp originated from it's fabrication procedure, an additional experiment was performed and AFM scans of the stamp and imprinted Si were acquired in the complementary locations upon Mac-Imprint (Figure 42A and B). Additionally, eight line scans of the top surface of the stamp and bottom surface of the imprinted Si were extracted from the complementary locations of the AFM scan (Figure 42C, blue and red lines, respectively). Prior analysis, the scans were leveled with respect to flat surfaces (bottom of the stamp and top of the Si, respectively). It was observed that both unique features of the stamp such as protrusions and pits (marked with black dashed lines on Figure 42C) and the overall slope of the stamp surface are accurately replicated onto Si. Additionally, three-point moving average profiles (Figure 42C, red lines) of both stamp and imprinted Si demonstrate the similar features across the length of the scan. Note that the AFM tip used for the scan acquisition has large front and back angles (25 ± 2.5° and 15 ± 2.5°) which did not allow for accurate capture of high aspect ratio features of the stamp such as inverted waveguide geometry and point defects (i.e., pits).

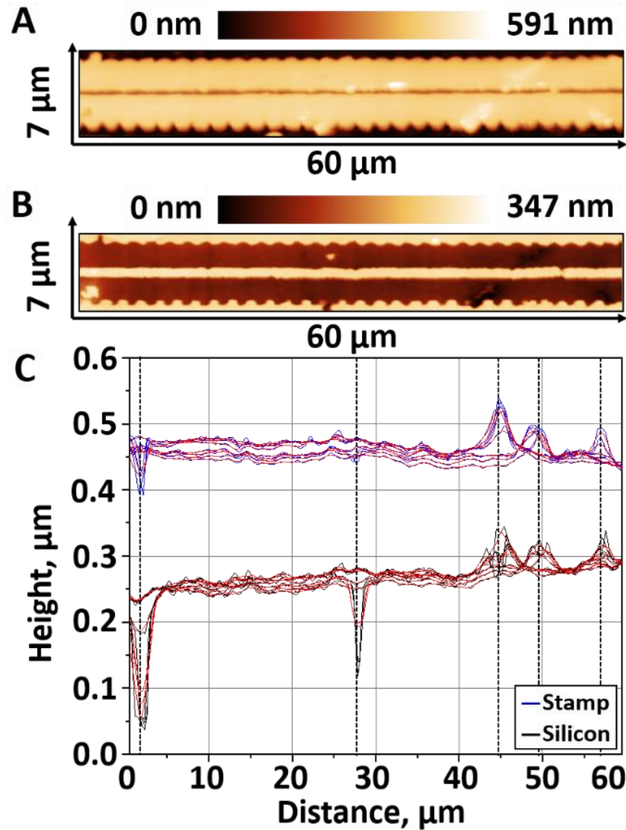

Figure 42. AFM profiles of Mac-Imprint stamp (A) and imprinted silicon (B) taken in complementary locations. C – line profiles of stamp heights (blue) and silicon etch depth (black). Red lines represent three-point moving average. Vertical black dashed lines highlight distinguishable features appearing on both stamp and imprinted Si.

The relationship between LER and MLWR

The minimum line width resolution (MLWR) of Mac-Imprint process depends on the line edge roughness (LER) of the imprinted pattern expressed by root mean square (RMS). In particular, the MLWR must be more than six times the RMS, otherwise the imprinted pattern will lose the continuity due to the partial overlap between upper and lower line edge profiles (solid black lines on Figure 43). By analogy, the separation of two neighboring patterns by more than six times the RMS will safely assume no overlap between them.

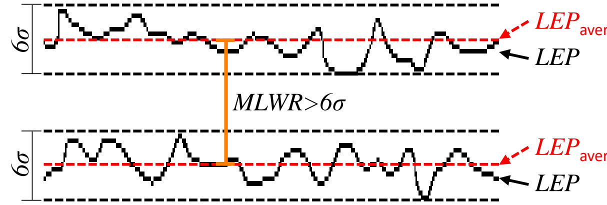

Figure 43. Relation between minimum line width resolution and line edge roughness. Solid black lines represent the edge of imprinted line (LEP). Dotted red lines represent the average line edge profile (LEP_{aver}). Dotted black lines represent 6 sigma interwal for the LEP deviation from LEP_{aver}

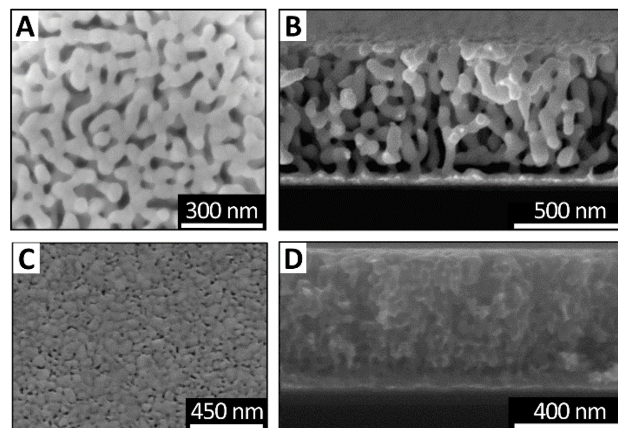

Figure 44. Top-down (A, C) and cross-sectional (B, D) SEM images of the catalyst films with average pore diameters of 42 (A, B) and 10 (C, D) nm.

SOI wafer pre-patterning and Etching solution storage

Upon the contact between centimeter-scale impervious stamp and monocrystalline substrate only small amount of etching solution is immobilized between former and latter. This etching solution is rapidly depleted in the very beginning of Mac-Imprint causing dissolution reaction to stop, which leads to the shallower etching in the center of the contact and deeper on the periphery, where the etching solution supply is abundant. In partially porous stamps (where porous catalyst is attached to the impervious stamp) only periphery

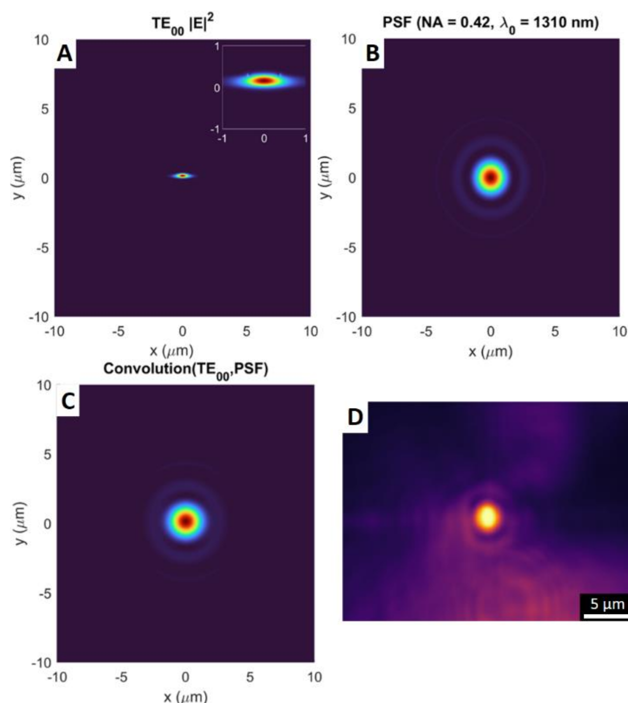

Figure 45. A – Simulated waveguide mode with w = 750 nm, h = 43 nm. B – Point spread function (PSF) for a NA = 0.42 objective operating at 1310 nm. C – Convolution between A and B indicating the expected IR image. D – measured IR image as averaged over 1290 to 1330 nm.

of the stamp provides access to the bulk of the etching solution, and diffusion from there is limited by the thickness and porosity of porous catalyst layer as well as geometry of the pattern (i.e., embedded channels). To overcome this limitation, previous works of the authors have used pre-patterning of the substrates with pillars.*(20, 24)* This creates additional etching solution storage, uniformly distributed throughout macroscopic stamp/substrate contact area and the same approach was implemented in this work.

The design of the pillar size, heights and pitch should be performed according to the following procedure and assumptions. At first, the HF acid is confined in the embedded gaps upon the contact between stamp and substrate. The total volume of Si that can be

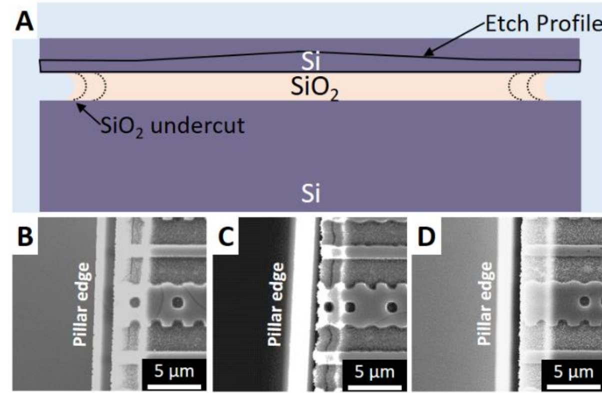

Figure 46. Buried oxide layer undercut during Mac-Imprint. A – Schematic of the undercut. B-D – Top down SEM images of the edge of the pillars, processed within 65, 70 and 75 sec, respectively

etched upon complete depletion of the HF (assuming 100% conversion efficiency and infinite reaction time) can be found according to the following formula:

$$V_{HF} = 6 \cdot \frac{M_{HF} \cdot \rho_{Si}}{\rho_{HF} \cdot M_{Si}} \cdot V_{Si} \approx 8.66 \cdot V_{Si} \quad (1)$$

Where M_{HF} – molar mass of HF (20.01, g/mol), M_{Si} – molar mass of Si (28.0855, g/mol), ρ_{HF} – density of HF (1.15, g/cm^3) and ρ_{Si} – density of HF (2.329, g/cm^3).

Thus, the increase of the pillar heights will result in the deeper etching, as has been experimentally confirmed in the previous work of the authors.*(20)*

The total volume of HF should be calculated based on the volume of Si to be removed which is determined by the target application, in particular the footprint of the device and it's depth. Based on that the width and length of the pillar can be estimated assuming that it does not exceed twice the EEPD of the np-Au on blank Si which was found to be ~ 700 µm. In the particular examples in this paper, this formula was not used since the etching time was only ~ 10 s (to minimize undercut of the BOX layer of the SOI wafer)

and, thus, the reactants were not completely depleted and its depth was limited by the rather short etch times.

APPENDIX B

MANAGEMENT OF THE ETCHING SOLUTION STORAGE REQUIREMENT IN THE LARGE-AREA MAC-IMPRINT USING POROUS POLYMER STAMPS

Estimation of the total etching solution storage capacity

The volume of the etching solution stored in the unit cell of the pre-patterned Si wafer (Figure 47A) can be calculated according to the formula:

$$V_{etch} = D \cdot (P^2 - W^2)$$

where D, P and W are depth and period of the unit cell and width of the Si pillar, respectively and are denoted on Figure 47A. Based on the unit cell dimensions reported in *(20, 24)* the V_{etch} varies between 0.00325 and **0.08125** µl.

The volume of the etching solution stored inside the porous polymer (Figure 47B) can be estimated according to the formula:

$$V_{etch} = D \cdot \phi \cdot W^2$$

where D, ϕ and W and are depth and porosity of the porous polymer and width of the Si substrate, respectively and are denoted on Figure 47B.

Thus, the commercially available porous PVDF membrane can store V_{etch} up to 0.015 µl which is comparable with the Si wafer pre-patterning with 25 µm tall pillars *(20)*. Based on the parameters of the TIPS PVDF membrane reported elsewhere *(113)* the V_{etch} varies between 0.0432 and **0.0864** µl which is comparable with the Si wafer pre-patterning with 125 µm tall pillars *(20)*. These calculations provide foundation for the use of porous PVDF membranes as stamps for Mac-Imprint of Si substrates without the need for their pre-patterning. It should be noted that the calculations of theoretical capacity of porous polymer membranes are based on the assumption that the total volume of membrane's voids is occupied with the etching solution.

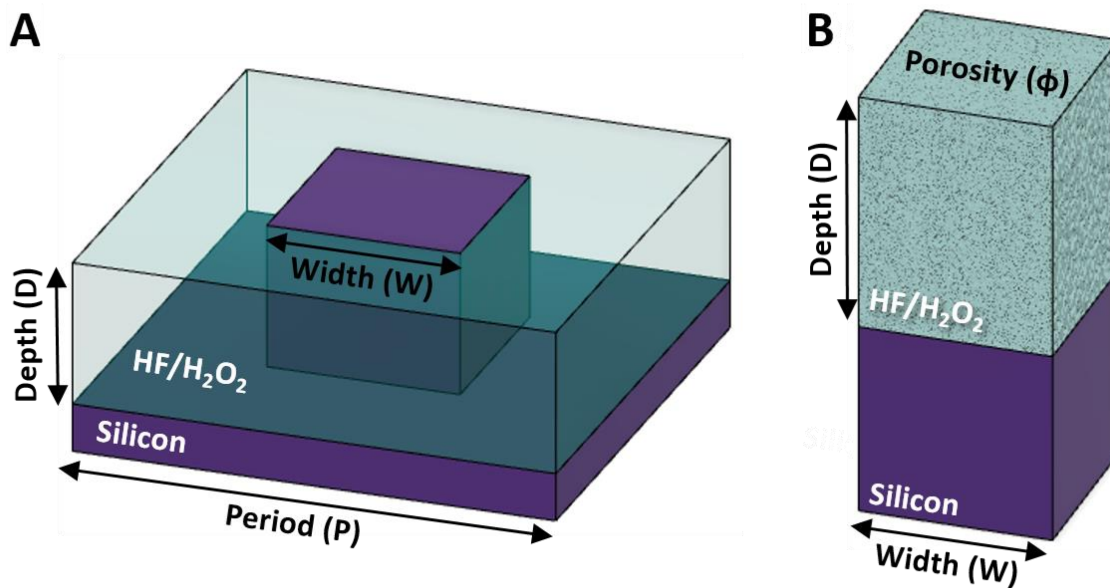

Figure 47. Estimated etching solution storage. A – Inside the unit cell of the pre-patterned Si wafer. B – Inside the porous polymer.

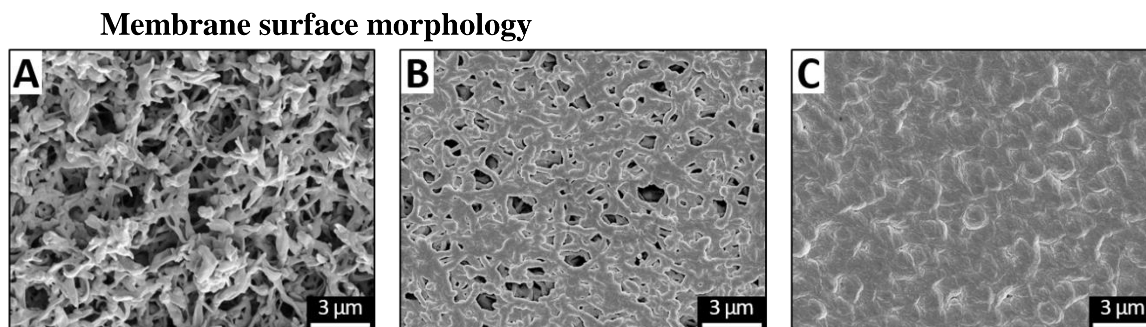

Figure 48. Top-down SEM images of commercial PVDF membranes coated with the different thickness catalyst. A – 80 nm. B – 320 nm, C – 3000 nm.

Influence of the Mac-Imprint duration on the reflectance

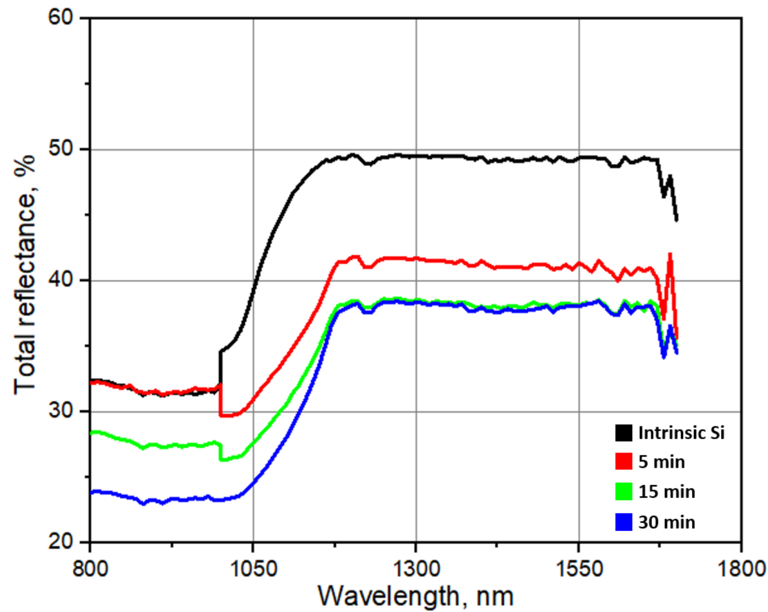

Figure 49. Total hemispherical reflectance of Si chips, Mac-Imprinted with commercial PVDF membranes.

Analysis of the pattern distortions during conformal Mac-Imprint

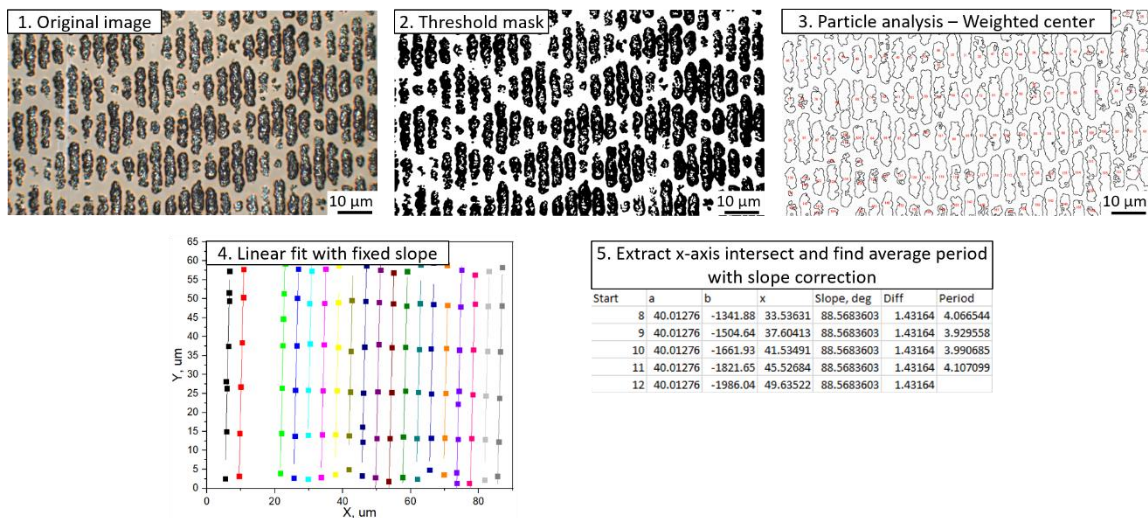

Start	a	b	x	Slope, deg	Diff	Period
8	40.01276	-1341.88	33.53631	88.5683603	1.43164	4.066544
9	40.01276	-1504.64	37.60413	88.5683603	1.43164	3.929558
10	40.01276	-1661.93	41.53491	88.5683603	1.43164	3.990685
11	40.01276	-1821.65	45.52684	88.5683603	1.43164	4.107099
12	40.01276	-1986.04	49.63522	88.5683603	1.43164	

Figure 50. Analysis of the pattern distortions during conformal Mac-Imprint

APPENDIX C

OBTAINED RIGHTS AND PERMISSIONS

Date	Article Title	Publication	Type Of Use	Price	Status	Expiration Date	Order Number
10-Nov-2022	Roughness Suppression in Electrochemical Nanoimprinting of Si for Applications in Silicon Photonics	Advanced Materials	Dissertation/Thesis	0.00 $	Completed		5425451429679
10-Nov-2022	Spatially-separated and photo-enhanced semiconductor corrosion processes for high-efficient and contamination-free electrochemical nanoimprint lithography	Science China Chemistry	Thesis/Dissertation	0.00 $	Completed		5425451313207
10-Nov-2022	Large-area homogeneous corrosion process for electrochemical nanoimprint lithography on GaAs wafer by modulating contact pressure	Journal of Electroanalytical Chemistry	reuse in a thesis/dissertation	0.00 $	Completed		5425451174373
10-Nov-2022	3D patterning of silicon by contact etching with anodically biased nanoporous gold electrodes	Electrochemistry Communications	reuse in a thesis/dissertation	0.00 $	Completed		5425450379869
10-Nov-2022	Electrochemical nanoimprint lithography directly on n-type crystalline silicon (111) wafer	Electrochemistry Communications	reuse in a thesis/dissertation	0.00 $	Completed		5425450133402
10-Nov-2022	Direct Imprinting of Porous Silicon via Metal-Assisted Chemical Etching	Advanced Functional Materials	Dissertation/Thesis	0.00 $	Completed		5425441474976
10-Nov-2022	Ultra-high aspect ratio high-resolution nanofabrication for hard X-ray diffractive optics	Nature Communications	Thesis/Dissertation	0.00 $	Completed		5425440360903
10-Nov-2022	3D Out-of-Plane Rotational Etching with Pinned Catalysts in Metal-Assisted Chemical Etching of Silicon	Advanced Functional Materials	Dissertation/Thesis	0.00 $	Completed		5425431279181
10-Nov-2022	Metal-assisted chemical etching of silicon in HF–H2O2	Electrochimica Acta	reuse in a thesis/dissertation	0.00 $	Completed		5425430727797
9-Nov-2022	On-chip transformation optics for multimode waveguide bends	Nature Communications	Thesis/Dissertation	0.00 $	Completed		5425051395159
9-Nov-2022	Designer spoof surface plasmon structures collimate terahertz laser beams	Nature Materials	Thesis/Dissertation	0.00 $	Completed		5425051065108

1. Soft matter

0.00 USD

Article: Biomimetic microlens array with antireflective "moth-eye" surface

Order License ID	Pending	Publisher	ROYAL SOCIETY OF CHEMISTRY
ISSN	1744-6848		
Type of Use	Republish in a thesis/dissertation	Portion	Image/photo/illustration

LICENSED CONTENT

//marketplace.copyright.com/rs-ui-web/mp/checkout/confirmation-details/837be1f4-db10-4c66-9fc3-34d67ece233d

!2, 5:40 PM https://marketplace.copyright.com/rs-ui-web/mp/checkout/confirmation-details/837be1f4-db10-4c66-9fc3-34d67ece233d

Publication Title	Soft matter	Rightsholder	Royal Society of Chemistry
Article Title	Biomimetic microlens array with antireflective "moth-eye" surface	Publication Type	e-Journal
		Start Page	6404
Author/Editor	Royal Society of Chemistry (Great Britain)	Issue	14
		Volume	7
Date	06/01/2005	URL	http://www.rsc.org/Publishing/Journals/sm/index.asp
Language	English		
Country	United Kingdom of Great Britain and Northern Ireland		

REQUEST DETAILS

Portion Type	Image/photo/illustration	Distribution	Worldwide
Number of Images / Photos / Illustrations	2	Translation	Original language of publication
Format (select all that apply)	Electronic	Copies for the Disabled?	No
		Minor Editing Privileges?	No
Who Will Republish the Content?	Academic institution	Incidental Promotional Use?	No
Duration of Use	Life of current edition		
Lifetime Unit Quantity	Up to 499	Currency	USD
Rights Requested	Main product		

NEW WORK DETAILS

Title	Metal-Assisted Electrochemical Nanoimprinting: Delivering Resolution and Throughput via Engineered Stamps	Institution Name	Arizona State University
		Expected Presentation Date	2022-11-14
Instructor Name	Bruno Azeredo		

SPRINGER NATURE

Chromatic-aberration-corrected diffractive lenses for ultra-broadband focusing

Author: Peng Wang et al

Publication: Scientific Reports

Publisher: Springer Nature

Date: Feb 12, 2016

Copyright © 2016, The Author(s)

Creative Commons

This is an open access article distributed under the terms of the Creative Commons CC BY license, which permits unrestricted use, distribution, and reproduction in any medium, provided the original work is properly cited.

You are not required to obtain permission to reuse this article.

To request permission for a type of use not listed, please contact Springer Nature

Model for the Mass Transport during Metal-Assisted Chemical Etching with Contiguous Metal Films As Catalysts

Author: Nadine Geyer, Bodo Fuhrmann, Zhipeng Huang, et al

Publication: The Journal of Physical Chemistry C

Publisher: American Chemical Society

Date: Jun 1, 2012

Copyright © 2012, American Chemical Society

PERMISSION/LICENSE IS GRANTED FOR YOUR ORDER AT NO CHARGE

This type of permission/license, instead of the standard Terms and Conditions, is sent to you because no fee is being charged for your order. Please note the following:

- Permission is granted for your request in both print and electronic formats, and translations.
- If figures and/or tables were requested, they may be adapted or used in part.
- Please print this page for your records and send a copy of it to your publisher/graduate school.
- Appropriate credit for the requested material should be given as follows: "Reprinted (adapted) with permission from {COMPLETE REFERENCE CITATION}. Copyright {YEAR} American Chemical Society." Insert appropriate information in place of the capitalized words.
- One-time permission is granted only for the use specified in your RightsLink request. No additional uses are granted (such as derivative works or other editions). For any uses, please submit a new request.

If credit is given to another source for the material you requested from RightsLink, permission must be obtained from that source.

Uniform Vertical Trench Etching on Silicon with High Aspect Ratio by Metal-Assisted Chemical Etching Using Nanoporous Catalysts

Author: Liyi Li, Yan Liu, Xueying Zhao, et al

Publication: Applied Materials

Publisher: American Chemical Society

Date: Jan 1, 2014

Copyright © 2014, American Chemical Society

PERMISSION/LICENSE IS GRANTED FOR YOUR ORDER AT NO CHARGE

This type of permission/license, instead of the standard Terms and Conditions, is sent to you because no fee is being charged for your order. Please note the following:

- Permission is granted for your request in both print and electronic formats, and translations.
- If figures and/or tables were requested, they may be adapted or used in part.
- Please print this page for your records and send a copy of it to your publisher/graduate school.
- Appropriate credit for the requested material should be given as follows: "Reprinted (adapted) with permission from {COMPLETE REFERENCE CITATION}. Copyright {YEAR} American Chemical Society." Insert appropriate information in place of the capitalized words.
- One-time permission is granted only for the use specified in your RightsLink request. No additional uses are granted (such as derivative works or other editions). For any uses, please submit a new request.

If credit is given to another source for the material you requested from RightsLink, permission must be obtained from that source.

Guided Three-Dimensional Catalyst Folding during Metal-Assisted Chemical Etching of Silicon

Author: Konrad Rykaczewski, Owen J. Hildreth, Ching P. Wong, et al

Publication: Nano Letters

Publisher: American Chemical Society

Date: Jun 1, 2011

Copyright © 2011, American Chemical Society

PERMISSION/LICENSE IS GRANTED FOR YOUR ORDER AT NO CHARGE

This type of permission/license, instead of the standard Terms and Conditions, is sent to you because no fee is being charged for your order. Please note the following:

- Permission is granted for your request in both print and electronic formats, and translations.
- If figures and/or tables were requested, they may be adapted or used in part.
- Please print this page for your records and send a copy of it to your publisher/graduate school.
- Appropriate credit for the requested material should be given as follows: "Reprinted (adapted) with permission from {COMPLETE REFERENCE CITATION}. Copyright {YEAR} American Chemical Society." Insert appropriate information in place of the capitalized words.
- One-time permission is granted only for the use specified in your RightsLink request. No additional uses are granted (such as derivative works or other editions). For any uses, please submit a new request.

If credit is given to another source for the material you requested from RightsLink, permission must be obtained from that source.

Mechanics of Catalyst Motion during Metal Assisted Chemical Etching of Silicon

Author: Chang Quan Lai, He Cheng, W. K. Choi, et al
Publication: The Journal of Physical Chemistry C
Publisher: American Chemical Society
Date: Oct 1, 2013

Copyright © 2013, American Chemical Society

PERMISSION/LICENSE IS GRANTED FOR YOUR ORDER AT NO CHARGE

This type of permission/license, instead of the standard Terms and Conditions, is sent to you because no fee is being charged for your order. Please note the following:

- Permission is granted for your request in both print and electronic formats, and translations.
- If figures and/or tables were requested, they may be adapted or used in part.
- Please print this page for your records and send a copy of it to your publisher/graduate school.
- Appropriate credit for the requested material should be given as follows: "Reprinted (adapted) with permission from {COMPLETE REFERENCE CITATION}. Copyright {YEAR} American Chemical Society." Insert appropriate information in place of the capitalized words.
- One-time permission is granted only for the use specified in your RightsLink request. No additional uses are granted (such as derivative works or other editions). For any uses, please submit a new request.

If credit is given to another source for the material you requested from RightsLink, permission must be obtained from that source.

Metal assisted chemical etching of silicon in the gas phase: a nanofabrication platform for X-ray optics

L. Romano, M. Kagias, J. Vila-Comamala, K. Jefimovs, L. Tseng, V. A. Guzenko and M. Stampanoni, *Nanoscale Horiz.*, 2020, **5**, 869 **DOI:** 10.1039/C9NH00709A

This article is licensed under a Creative Commons Attribution-NonCommercial 3.0 Unported Licence. **You can use material from this article in other publications, without requesting further permission** from the RSC, provided that the correct acknowledgement is given and it is not used for commercial purposes.

Publication Title	Electrochemical and solid-state letters	Country	United States of America
Author/Editor	Electrochemical Society, Institute of Electrical and Electronics Engineers.	Rightsholder	IOP Publishing, Ltd
Date	01/01/1998	Publication Type	e-Journal
Language	English	URL	http://ojps.aip.org/ESL

REQUEST DETAILS

Portion Type	Image/photo/illustration	Distribution	Worldwide
Number of Images / Photos / Illustrations	1	Translation	Original language of publication
Format (select all that apply)	Electronic	Copies for the Disabled?	No
Who Will Republish the Content?	Academic institution	Minor Editing Privileges?	No
Duration of Use	Life of current and all future editions	Incidental Promotional Use?	No
Lifetime Unit Quantity	Up to 499	Currency	USD
Rights Requested	Main product		

NEW WORK DETAILS

Title	Metal-Assisted Electrochemical Nanoimprinting: Delivering Resolution and Throughput via Engineered Stamps	Institution Name	Arizona State University
Instructor Name	Bruno Azeredo	Expected Presentation Date	2022-11-14

ADDITIONAL DETAILS

Order Reference Number	13	The Requesting Person/Organization to Appear on the License	Aliaksandr Sharstniou

REUSE CONTENT DETAILS

Title, Description or Numeric Reference of the Portion(s)	Figure 5	Title of the Article/Chapter the Portion Is From	Fabrication of Low Reflectivity Poly-Crystalline Si Surfaces by Structure Transfer Method
Editor of Portion(s)	N/A	Author of Portion(s)	Electrochemical Society; Institute of Electrical and Electronics Engineers.
Volume of Serial or Monograph	N/A	Issue, if Republishing an Article From a Serial	N/A
Page or Page Range of Portion	B14		

Publication Title	Journal of the Electrochemical Society	Country	United States of America
Author/Editor	Electrochemical Society.	Rightsholder	IOP Publishing, Ltd
Date	01/01/1948	Publication Type	e-Journal
Language	English	URL	http://www.scitation.org/JES

REQUEST DETAILS

Portion Type	Image/photo/illustration	Distribution	Worldwide
Number of Images / Photos / Illustrations	1	Translation	Original language of publication
Format (select all that apply)	Electronic	Copies for the Disabled?	No
Who Will Republish the Content?	Academic institution	Minor Editing Privileges?	No
Duration of Use	Life of current and all future editions	Incidental Promotional Use?	No
Lifetime Unit Quantity	Up to 499	Currency	USD
Rights Requested	Main product		

NEW WORK DETAILS

Title	Metal-Assisted Electrochemical Nanoimprinting: Delivering Resolution and Throughput via Engineered Stamps	Institution Name	Arizona State University
Instructor Name	Bruno Azeredo	Expected Presentation Date	2022-11-14

ADDITIONAL DETAILS

Order Reference Number	14	The Requesting Person/Organization to Appear on the License	Aliaksandr Sharstniou

REUSE CONTENT DETAILS

Title, Description or Numeric Reference of the Portion(s)	Figure 2	Title of the Article/Chapter the Portion Is From	Surface Structure Chemical Transfer Method for Formation of Ultralow Reflectivity Si Surfaces
Editor of Portion(s)	N/A	Author of Portion(s)	Electrochemical Society.
Volume of Serial or Monograph	N/A	Issue, if Republishing an Article From a Serial	N/A
Page or Page Range of Portion	H444	Publication Date of Portion	1947-12-31

RIGHTSHOLDER TERMS AND CONDITIONS

Direct Production of Silicon Nanostructures with Electrochemical Nanoimprinting

Author: Hailiang Li, Jiebin Niu, Guanya Wang, et al

Publication: ACS Applied Electronic Materials

Publisher: American Chemical Society

Date: Jul 1, 2019

Copyright © 2019, American Chemical Society

PERMISSION/LICENSE IS GRANTED FOR YOUR ORDER AT NO CHARGE

This type of permission/license, instead of the standard Terms and Conditions, is sent to you because no fee is being charged for your order. Please note the following:

- Permission is granted for your request in both print and electronic formats, and translations.
- If figures and/or tables were requested, they may be adapted or used in part.
- Please print this page for your records and send a copy of it to your publisher/graduate school.
- Appropriate credit for the requested material should be given as follows: "Reprinted (adapted) with permission from {COMPLETE REFERENCE CITATION}. Copyright {YEAR} American Chemical Society." Insert appropriate information in place of the capitalized words.
- One-time permission is granted only for the use specified in your RightsLink request. No additional uses are granted (such as derivative works or other editions). For any uses, please submit a new request.

If credit is given to another source for the material you requested from RightsLink, permission must be obtained from that source.

Citation: Bastide S, Torralba E, Halbwax M, Le Gall S, Mpogui E, Cachet-Vivier C, Magnin V, Harari J, Yarekha D and Vilcot J-P (2019) 3D Patterning of Si by Contact Etching With Nanoporous Metals. *Front. Chem.* 7:256. doi: 10.3389/fchem.2019.00256

Received: 03 December 2018; **Accepted:** 01 April 2019;
Published: 25 April 2019.

Edited by:
Thierry Djenizian (https://loop.frontiersin.org/people/534703/overview), École des Mines de Saint-Étienne-Campus Georges Charpak Provence, France

Reviewed by:
Bruno Azeredo (https://loop.frontiersin.org/people/656161/overview), Arizona State University, United States
Thomas Defforge (https://loop.frontiersin.org/people/683033/overview), UMR7347 Matériaux, Microélectronique, Acoustique, Nanotechnologies (GREMAN), France

Copyright © 2019 Bastide, Torralba, Halbwax, Le Gall, Mpogui, Cachet-Vivier, Magnin, Harari, Yarekha and Vilcot. This is an open-access article distributed under the terms of the Creative Commons Attribution License (CC BY) (http://creativecommons.org/licenses/by/4.0/). The use, distribution or reproduction in other forums is permitted, provided the original author(s) and the copyright owner(s) are credited and that the original publication in this journal is cited, in accordance with accepted academic practice. No use, distribution or reproduction is permitted which does not comply with these terms.

***Correspondence:** Stéphane Bastide, bastide@icmpe.cnrs.fr (mailto:bastide@icmpe.cnrs.fr)

Electrochemical nanoimprinti

Aliaksandr Sharstniou, Stanislau Niauzorau, Placid M. Ferreira, and Bruno P. Azer

Edited by Joseph M. DeSimone, University of North Carolina at Chapel Hill, Chapel Hill, NC, and

May 8, 2019 | 116 (21) 10264-10269 | https://doi.org/10.1073/pnas.1820420116

6,290 | 12

Significance

The indirect nature of existing parallel micromac
templates with top-down processes to etch 3D n
produces poor out-of-plane patterning fidelity. H
is measured for microscale curvilinear 3D object
over features as wide as 10 µm. These results ar
diffusion, which increase the kinetics of the anoc
of nanotextured silicon lenses are deterministica

Published in

PROCEEDINGS OF THE NATIONAL ACADEMY OF SCIENCES

Vol. 116 | No. 21
May 21, 2019

PubMed: 31068475

PDF
Help

Classifications

PHYSICAL SCIENCES | ENGINEERING

Copyright

Copyright © 2019 the Author(s). Published by PNAS. This open access article is distributed under Creative Commons Attribution License 4.0 (CC BY).

Creative Commons License De

Attribution 4.0 International (CC BY 4.0)

This is a human-readable summary of (and not a substitute for) the license.

You are free to:

Share — copy and redistribute the material in any medium or format

Adapt — remix, transform, and build upon the material

for any purpose, even commercially.

The licensor cannot revoke these freedoms as long as you follow the license terms.

Under the following terms:

Attribution — You must give appropriate credit, provide a link to the license, and indicate if changes were made. You may do so in any reasonable manner, but not in any way that suggests the licensor endorses you or your use.

No additional restrictions — You may not apply legal terms or technological measures that legally restrict others from doing anything the license permits.

Notices:

You do not have to comply with the license for elements of the material in the public domain or where your use is permitted by an applicable exception or limitation.

No warranties are given. The license may not give you all of the permissions necessary for your intended use. For example, other rights such as publicity, privacy, or moral rights may limit how you use the material.

Formation of Through-Holes in Si Wafers by Using Anodically Polarized Needle Electrodes in HF Solution

Author: Tomohiko Sugita, Chia-Lung Lee, Shigeru Ikeda, et al

Publication: Applied Materials

Publisher: American Chemical Society

Date: Jul 1, 2011

Copyright © 2011, American Chemical Society

PERMISSION/LICENSE IS GRANTED FOR YOUR ORDER AT NO CHARGE

This type of permission/license, instead of the standard Terms and Conditions, is sent to you because no fee is being charged for your order. Please note the following:

- Permission is granted for your request in both print and electronic formats, and translations.
- If figures and/or tables were requested, they may be adapted or used in part.
- Please print this page for your records and send a copy of it to your publisher/graduate school.
- Appropriate credit for the requested material should be given as follows: "Reprinted (adapted) with permission from {COMPLETE REFERENCE CITATION}. Copyright {YEAR} American Chemical Society." Insert appropriate information in place of the capitalized words.
- One-time permission is granted only for the use specified in your RightsLink request. No additional uses are granted (such as derivative works or other editions). For any uses, please submit a new request.

If credit is given to another source for the material you requested from RightsLink, permission must be obtained from that source.

Anisotropic Nanoparticles as Shape-Directing Catalysts for the Chemical Etching of Silicon

Author: Guoliang Liu, Kaylie L. Young, Xing Liao, et al

Publication: Journal of the American Chemical Society

Publisher: American Chemical Society

Date: Aug 1, 2013

Copyright © 2013, American Chemical Society

PERMISSION/LICENSE IS GRANTED FOR YOUR ORDER AT NO CHARGE

This type of permission/license, instead of the standard Terms and Conditions, is sent to you because no fee is being charged for your order. Please note the following:

- Permission is granted for your request in both print and electronic formats, and translations.
- If figures and/or tables were requested, they may be adapted or used in part.
- Please print this page for your records and send a copy of it to your publisher/graduate school.
- Appropriate credit for the requested material should be given as follows: "Reprinted (adapted) with permission from {COMPLETE REFERENCE CITATION}. Copyright {YEAR} American Chemical Society." Insert appropriate information in place of the capitalized words.
- One-time permission is granted only for the use specified in your RightsLink request. No additional uses are granted (such as derivative works or other editions). For any uses, please submit a new request.

If credit is given to another source for the material you requested from RightsLink, permission must be obtained from that source.

Publication Title	Proceedings of the Royal Society of London. Series B: Biological Sciences. Biological sciences	Country	United Kingdom of Great Britain and Northern Ireland
Author/Editor	Royal Society (Great Britain)	Rightsholder	The Royal Society (U.K.)
Date	01/01/1997	Publication Type	e-Journal
Language	English	URL	https://royalsociety.org/journals/

REQUEST DETAILS

Portion Type	Image/photo/illustration	Distribution	Worldwide
Number of Images / Photos / Illustrations	1	Translation	Original language of publication
Format (select all that apply)	Electronic	Copies for the Disabled?	No
Who Will Republish the Content?	Academic institution	Minor Editing Privileges?	No
Duration of Use	Life of current and all future editions	Incidental Promotional Use?	No
Lifetime Unit Quantity	Up to 499	Currency	USD
Rights Requested	Main product		

NEW WORK DETAILS

Title	Metal-Assisted Electrochemical Nanoimprinting: Delivering Resolution and Throughput via Engineered Stamps	Institution Name	Arizona State University
Instructor Name	Bruno Azeredo	Expected Presentation Date	2022-11-14

ADDITIONAL DETAILS

Order Reference Number	26	The Requesting Person/Organization to Appear on the License	Aliaksandr Sharstniou

REUSE CONTENT DETAILS

Title, Description or Numeric Reference of the Portion(s)	Figure 1	Title of the Article/Chapter the Portion Is From	Light on the moth-eye corneal nipple array of butterflie
Editor of Portion(s)	N/A	Author of Portion(s)	Royal Society (Great Britain)
Volume of Serial or Monograph	N/A	Issue, if Republishing an Article From a Serial	N/A
Page or Page Range of Portion	662	Publication Date of Portion	1996-12-31

Publication Title	The journal of experimental biology	Rightsholder	The Company of Biologists Ltd.
Article Title	Biomimetic shark skin: design, fabrication and hydrodynamic function.	Publication Type	Journal
Author/Editor	COMPANY OF BIOLOGISTS., SOCIETY FOR EXPERIMENTAL BIOLOGY (GREAT BRITAIN)	Start Page	1656
Date	01/01/1923	End Page	1666
Language	English	Issue	Pt 10
Country	United Kingdom of Great Britain and Northern Ireland	Volume	217

REQUEST DETAILS

Portion Type	Image/photo/illustration	Distribution	Worldwide
Number of Images / Photos / Illustrations	1	Translation	Original language of publication
Format (select all that apply)	Electronic	Copies for the Disabled?	No
Who Will Republish the Content?	Academic institution	Minor Editing Privileges?	No
Duration of Use	Life of current and all future editions	Incidental Promotional Use?	No
Lifetime Unit Quantity	Up to 499	Currency	USD
Rights Requested	Main product		

NEW WORK DETAILS

Title	Metal-Assisted Electrochemical Nanoimprinting: Delivering Resolution and Throughput via Engineered Stamps	Institution Name	Arizona State University
Instructor Name	Bruno Azeredo	Expected Presentation Date	2022-11-14

ADDITIONAL DETAILS

Order Reference Number	27	The Requesting Person/Organization to Appear on the License	Aliaksandr Sharstniou

REUSE CONTENT DETAILS

Title, Description or Numeric Reference of the Portion(s)	Figure 1	Title of the Article/Chapter the Portion Is From	Biomimetic shark skin: design, fabrication and hydrodynamic function.

APPENDIX D

ORIGINAL VERSION OF PREVIOUSLY PUBLISHED ARTICLE ENTITLED "ROUGHNESS SUPPRESSION IN ELECTROCHEMICAL NANOIMPRINTING OF SI FOR APPLICATIONS IN SILICON PHOTONICS"

Roughness suppression in electrochemical nanoimprinting of Si for applications in silicon photonics

Aliaksandr Sharstniou, Stanislau Niauzorau, Anna L. Hardison, Matthew Puckett, Neil Krueger, Judson D. Ryckman, and Bruno Azeredo*

A. S., S. N., Prof. B. A.

Arizona State University – 6075 S. Innovation Way West, Mesa, AZ 85212, USA

E-mail: Bruno.Azeredo@asu.edu

A. L. H., J. D. R.

Clemson University – 91 Technology Drive, Anderson, SC 29625, USA

M. P.

Honeywell International – 21111 N. 19th Avenue, Phoenix, AZ 85027, USA

N. K.

Honeywell International – 12001 State Highway 55, Plymouth, MN 55441, USA

Keywords: electrochemical nanoimprinting, silicon photonics, rib waveguides, 3D nanophotonics, optical metasurfaces, metal-assisted chemical etching

Metal-assisted electrochemical nanoimprinting (Mac-Imprint) scales the fabrication of micro- and nanoscale 3D freeform geometries in silicon and holds the promise to enable novel chip-scale optics operating at the near-infrared spectrum. However, Mac-Imprint of silicon concomitantly generates mesoscale roughness (e.g., protrusion size ~ 45 nm) creating prohibitive levels of light scattering. This arises from the requirement to coat stamps with nanoporous gold catalyst that, while sustaining etchant diffusion, imprints its pores (e.g., dave ~ 42 nm) onto silicon. In this paper, roughness is reduced to sub-10 nm levels, which is in par with plasma etching, by decreasing pore size of the catalyst via dealloying in far-from equilibrium conditions. At this level, single-digit nanometric details such as grain boundary grooves of the catalyst are imprinted and attributed to the resolution limit of Mac-Imprint which is argued to be twice the Debye length (i.e., 1.7 nm) – a finding that broadly applies to metal-assisted chemical etching. Lastly, Mac-Imprint is employed to produce single-mode rib-waveguides on pre-patterned silicon-on-insulator wafers with root-mean-square RMS line edge roughness less than 10 nm while providing depth uniformity (i.e., 42.9 ± 5.5 nm), and limited levels of silicon defect formation (e.g., Raman peak shift <0.1 cm-1) and sidewall scattering.

1. Introduction

Silicon photonics utilizes a variety of micro- and nanostructured waveguide and metamaterial-based components to enable applications such as optical interconnects within a chip, from chip-to-fiber and chip-to-chip.(1) However, the efficiency, performance,

minimum feature size, and scalable manufacturing of chip-scale silicon photonic devices is presently constrained to 2D designs compatible with modern deep ultraviolet (DUV) or immersion lithography combined with reactive ion etching (RIE).(2, 3) Introduction of 3D designs with grayscale or multi-level etch depths has been proposed to increase the performance and/or compactness of grating couplers,(4–6) edge couplers,(7) multi-mode waveguide bends,(8) waveguide crossings,(9) polarization convertors,(10) small-mode area waveguides,(11, 12) and more. It also allows for the fabrication of advanced 3D photonic devices such as spoof surface plasmon structures,(13) chromatic-aberration corrected lenses,(14) and quasicrystal interferometers with physical unclonable functions.(15) However, such 3D structures are sensitive to depth and shape inaccuracy of plasma etching and have so far remained challenging to realize while maintaining the scalability requirements of the semiconductor industry.

Recent demonstrations of 3D or multi-level silicon photonic components have utilized multiple lithography and RIE steps to achieve multi-level etch depths,(4–6) or grayscale electron beam lithography (EBL) to achieve analog profiles.(8, 9) The former multi-step photolithography-based process inherently prohibits the independent and arbitrary control of lateral feature size and depth, while the latter EBL-based process is a direct writing technique and is not a scalable manufacturing solution. Both processes also require precise control over RIE selectivity, etching rate, and time to achieve the precisely desired silicon micro- or nanostructure dimensions. This challenging task is further complicated by loading effects and aspect-ratio dependent etch rates.(16, 17) Alternatively, the independent control of feature size and depth can be attained using direct parallel

nanofabrication methods such as nanoimprint lithography of inorganic materials, which can either (i) mechanically pattern molten or porosified substrates,(18, 19) or (ii) electrochemically carve it via metal-assisted electrochemical nanoimprinting (Mac-Imprint).(20–22) The former two approaches are unable to pattern SOI wafers and retain its solid and single-crystalline SOI characteristics. Mac-Imprint by-passes this issue by catalyzing the corrosion of silicon at the contact points between itself and a noble-metal coated stamp in the presence of hydrofluoric acid and an oxidizer (Figure 1A)(22, 23) whose detailed mechanism has been explained in existing literature on metal-assisted chemical etching (MACE) that is focused on thin-film catalysts directly deposited onto silicon.(24–26) Unlike MACE, in which the noble metal catalyst is not reusable and it's motion governed by the crystallography orientation of Si and etching conditions,(27, 28) Mac-Imprint by-passes these issues as the noble-metal catalyst is mechanically attached to the stamp and is retrieved upon each imprint cycle. At the same time, it introduces demolding issues such as delamination particularly prominent in high-aspect ratio structures (>1).

High pattern transfer fidelity during Mac-Imprint of monocrystalline Si (Figure 1B and C) requires mass-transport of reactants through a nanoporous gold (np-Au) catalyst,(23, 29) because solid catalysts cannot provide sufficient diffusion on length scales larger than 0.5 µm if Si is to be etched without concomitant porosification.(30) At the same time, the catalyst pore size (e.g., dave ~ 42 nm in Sharstniou et al.)(23) is accurately transferred onto the bottom and sidewalls of the imprinted surface which increases bottom and line edge roughness (LER) of imprinted structures (i.e., ~ 49 nm)(23) and induces

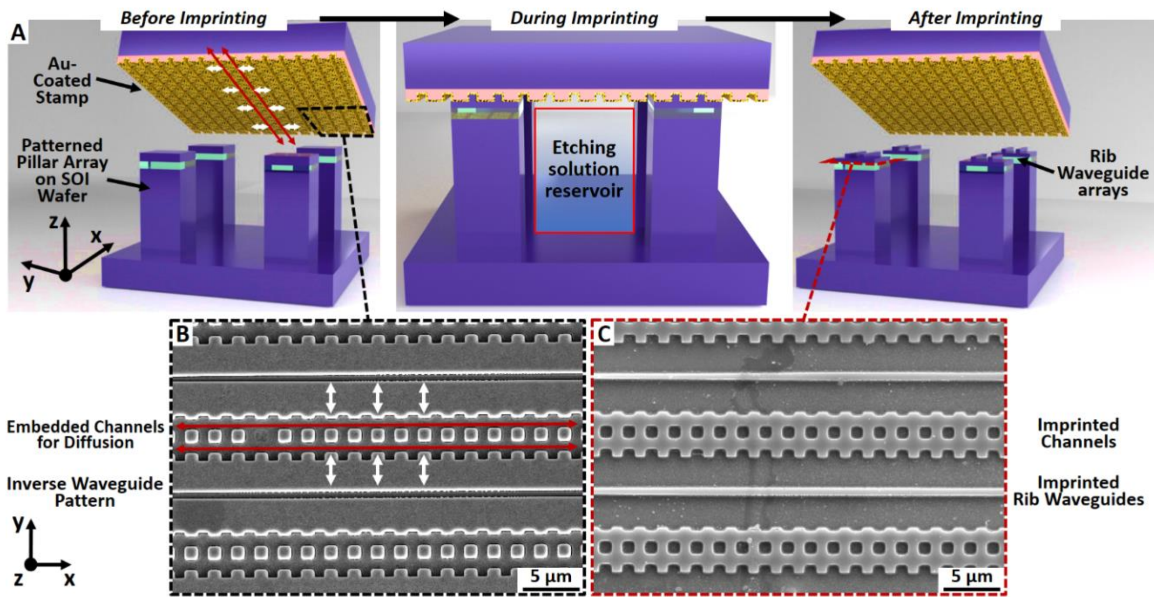

Figure 1. A – Schematics of the catalytic stamp and patterned SOI wafer interaction during Mac-Imprint; B and C – Top-down SEM images of catalytic stamp and Si rib waveguide patterns respectively. The coordinate systems indicate the parallel (x), perpendicular (y) and vertical (z) directions relative to the principal axis of the waveguide. Arrows highlight the solution diffusion pathways: red - through the embedded channels towards the center of the SOI pillar, and light blue – through the catalyst in-between embedded channels and waveguide patterns.

prohibitive levels of scattering losses in waveguides.(31) Conventional RIE machined waveguides have an as-machined roughness of 10 nm that can be smoothened in post-processing down to 2 nm.(32)

With the goal of prototyping functional silicon rib waveguides using Mac-Imprint of SOI wafers, this paper elucidates the mechanism by which roughness is generated and suppresses it by reducing the pore size of the catalyst to sub-10 nm levels. The latter is attained via the synthesis of np-Au in far-from-equilibrium conditions using established process-structure relationships for dealloying.(33) Bottom roughness surrounding the

waveguide and its LER are reduced to less than 10 nm which represents a 75 % improvement relative to prior work.(23) At the lowest roughness levels, the grain boundary grooves of the np-Au are discernable on the surface of the imprinted Si and is a major contributor to it. This observation is discussed in the context of the resolution limit of Mac-Imprint and MACE which was first hypothesized by Sugita et al. to be proportional to the Debye length present at the metal-solution interface.(34) Albeit never experimentally confirmed, a new analysis of previous work on MACE with ultra-fine gold nanoparticles reported by Liu et al.(35) along with experimental data presented in this work strongly support Sugita's hypothesis to be true. This finding directly applies to both Mac-Imprint and MACE as they share the same fundamental mechanisms. Additionally, the influence of the solution diffusion supported by the porous catalyst on Mac-Imprint's patterning fidelity is presented in comparison to its solid counterpart. The reduced pore sizes of the catalyst increase the cathodic reaction rate,(23) which is compensated by increasing the Chartier-Bastide parameter (known as 'ρ' in literature)(25) to 99.5% yielding Si waveguides with limited levels of defect formation as characterized by Raman spectroscopy. Finally, the optical characterization of nanoimprinted rib waveguides (i) confirms the single mode light propagation which matches electromagnetic simulations, and (ii) IR imaging reveals no significant levels of light scattering from its walls.

2. Results and Discussion

Mac-Imprint of Si waveguides onto the SOI pillars requires diffusion of reactants and byproducts over a large (e.g., >75 µm) and a heterogeneous pathway. This path extends from the edge of the pillar where reactants are stored in the solution reservoir confined around the pillar and towards its center (Figure 1A and B) and consists of embedded channels in the stamp parallel (i.e., x-direction) to the waveguide's principal axis (red arrows on Figure 1A and B) that are formed in the gaps between stamp and substrate upon their contact. Additionally, the solution must diffuse in the perpendicular direction (i.e., y-direction) between the waveguide and the embedded channels through the catalytic film (white arrows on Figure 1A and B) for a total distance of 3 µm. Note that the scenario in which diffusion takes place through a porosified silicon layer is detrimental to the waveguide's performance as it can create refractive index spatial variations.(23) When both pathways support enough etching solution diffusion, the pattern from the stamp is accurately transferred onto Si without porous defects (Figure 1C).

2.1. Limiting diffusional pathways

In order to evidence the role of the catalyst film's porosity on supporting diffusion of the etching solution, pre-patterned SOI chips were Mac-Imprinted with stamps coated with thin-films of solid Au (Figure 2A and B) and porous Au (Figure 2C and D). Pillars imprinted with solid Au stamps yielded waveguide patterns near its edges with distinguishable profile and depth (Figure 2B). However, the pattern becomes shallower and loses contrast in the SEM images as it approaches the center of the pillar. The average

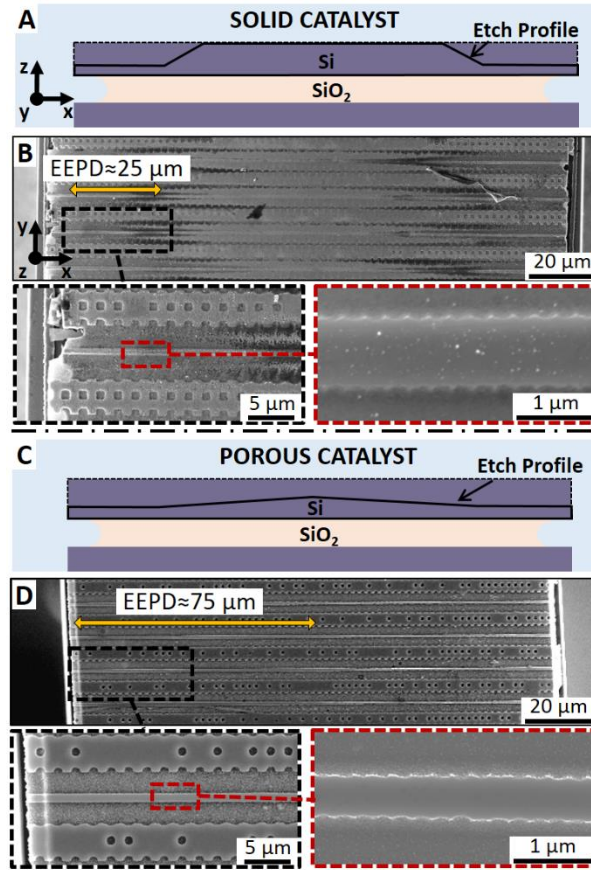

Figure 2. A and B – Schematic cross-section and top-down SEM images respectively of waveguide arrays imrinting with solid Au catalyst. Inset in B highlights the beginning of porous silicon formation region. C and D – Schematic cross-section and top-down SEM images respectively of the waveguide arrays imprinting with porous Au catalyst. Solid yellow arrows indicate the length of the region with distinguishable waveguide pattern (EEPD).

distance from the edge of the pillar to the end of the distinguishable waveguide pattern is indicated by solid yellow arrows in Figure 2B and D and termed as the effective etching penetration distance (EEPD). At the end of the EEPD, not only patterns become indistinguishable, but SEM images reveal the formation of porous silicon defects (dark areas in Figure 2B). Note, that periodic grating with the period of 273 ± 8 nm and heights of 82 ± 10 nm could be observed on high magnification SEM image (Figure 2B) along the

edge of the waveguide. The geometry of this grating mimics the one of original Si master mold highlighting the resolution capability of Mac-Imprint.

In contrast, pillars imprinted with porous Au stamps (Figure 2D) yielded an EEPD value that is maximum, and, thus, the entire half-width of the SOI pillar was successfully imprinted with the waveguide's pattern without any observable defect (e.g., porous silicon) formation. In a separate experiment, the largest EEPD that the porous catalyst and embedded channels can support was found to be ≈700 μm by imprinting a Si substrate with wider pillars and a blank Si wafer (see Figure S1 and Figure S2 in Supporting Information), suggesting the porous catalyst cannot support diffusion beyond that length scale. Note, the periodic grating with the period of 255 ± 2 nm and heights of 64 ± 7 nm is also observed in the case of Mac-Imprint with np-Au (Figure 2D).

In contrast to the imprint results with the solid catalyst (Figure 2A-B), the addition of the thin porous catalyst represents a small increase in the cross-sectional area available for free-solution diffusion in the parallel direction (x-direction) and, thus, the effective diffusion constant is expected to be marginally altered. However, the effective diffusion constant along the perpendicular direction (y-direction) has been increased by orders of magnitude in comparison to the case of the solid catalyst. That is because the diffusion in the solid catalyst is supported through the grain boundaries which support a diffusional regime known as molecular sieving with an effective diffusion constant that is orders of magnitude lower than the diffusion in free solution.(23) Meanwhile, the porous catalyst has pore sizes ranging from 10-42 nm which are much larger than the electric double layer thickness which is approximately 8.6 Å (for detailed calculations, see Supporting

Information), and can support free solution diffusion,(36) with simple corrections for tortuosity.(37, 38) Note that the thickness of the precursor film was selected to be much larger (e.g. 9 times) than the catalyst's pore size (i.e., 42 nm) to sustain diffusion through a well-developed 3D pore network without any optimization in its selection. A 'digital twin' model that captures both reaction rate and diffusional transport for Mac-Imprint with thinner catalysts is likely needed in the future to address such design questions. Instead, in this paper, the catalyst's high-surface area and its increased cathodic reaction rate is compensated by increasing the Chartier-Bastide parameter (known as 'ρ' in literature)(25) to 99.5% until porous silicon formation is suppressed as characterized by Raman spectroscopy. Alternatively, the use of a counter electrode in solution biased against the gold catalyst as in prior works of Torralba et al.(21) and Kim et al.(39) is recommended as it does not require hydrogen peroxide and the reaction rate can be externally controlled via biasing.

In addition to the role of diffusion mechanisms, the results for the solid catalyst case such as the short EEPD, the non-uniform etch depth and the porous silicon formation (Figure 2A-B) cannot be fully understood unless one considers the kinetics of the etching reaction during metal-assisted chemical etching (MACE). At first, oxidant is reduced on the surface of a noble metal (cathodic reaction), which results in the generation of positive charge carriers (holes) in Si.(25) Then, the holes are injected into Si through noble metal/Si Schottky junction and subsequently consumed during Si dissolution (anodic reaction).(25) Thus, whenever the diffusion of reactants towards the catalyst/Si contact interface is not sufficient, instead of confined etching under the catalyst, the porosification of silicon takes

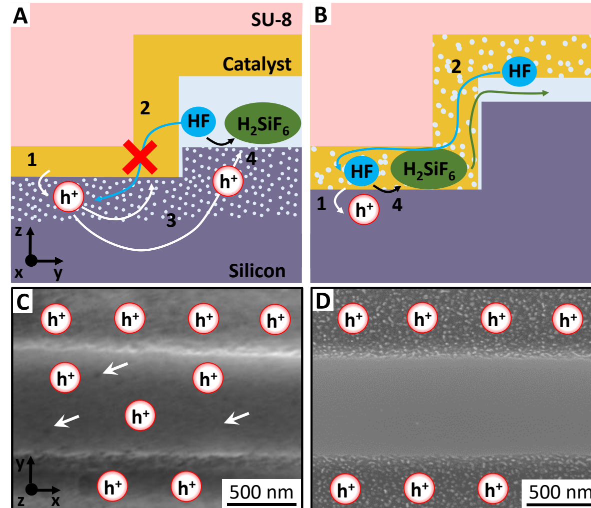

Figure 3. A and B – Schematics of charge- and mass-transport processes. C and D – High-magnification top-down images of the individual waveguides. Holes are added to illustrate the charge carrier distribution around catalyst/Si interface. White arrows point to the visible pores. A, C and B, D correspond to Mac-Imprint with solid and porous catalysts, respectively.

place around the catalyst/Si/etching solution triple junction in both conventional MACE as well as in Mac-Imprint.(22, 23, 30) This is expected to take place in the case of Mac-Imprint with solid catalyst since the mass-transport for the etching solution in the perpendicular direction (i.e., labeled as “2” in Figure 3A) is constricted. Thus, the holes injected into Si at its junction with the catalyst (i.e., step labeled as “1” in Figure 3A) can diffuse through the substrate to the interface between the etching solution and Si (i.e., step labeled as “3”). Once holes reach the etching solution/Si interface they induce its porosification (step labeled as “4”). Upon the growth of a porous silicon layer underneath the catalyst, the anisotropic etching of silicon can take place since etching solution can now reach the catalyst/Si interface. This mechanism can explain the concomitant observation of anisotropically etched features (i.e. waveguide geometry) near the edges of the Si pillar (Figure 2B) and the porosification of the silicon surface observed in Figure 3C. Note that

porous silicon is observed both in the regions surrounding the waveguide as well as in itself.

Ultimately, the uncontrollable porosification process is more pronounced on the edge of the pillar due to the abundant supply of reactants and is followed by its fast depletion in the embedded channel resulting in shallow etching depths in the center of the pillar which defines the EEPD distance. These findings highlight the fundamental limitation of solid catalyst since it cannot support the perpendicular diffusion for anisotropic imprinting of the designed 3 μm wide features, which is consistent with MACE literature on thin-film catalyst formats.(30, 40, 41) In recent literature of Si Mac-Imprint with solid catalysts, this issue was by-passed by designing stamps with an array of widely spaced patterns that simultaneously provided space for solution storage and were narrow enough (<520 nm) to sustain diffusion through the grain boundaries of catalyst or a porous layer underneath it.(42) Despite enabling diffusion, the nanoporous catalyst has higher specific surface area compared to its solid counterpart. This will inevitably increase the rate of H2O2 reduction and, as a result, lead to Si porosification.(23) Thus, this work implemented a reduction of the H2O2 concentration relative to the literature in MACE based on thin-films,(25) and increase in ρ value to 99.5% to minimize this effect and yield solid waveguides in Figure 3D. It should be noted that the cathodic reaction can be spatially-separated from the anodic reaction,(43) with a counter electrode placed in solution polarized against the gold catalyst with or without a salt bridge,(21) which guarantees that diffusion and solution storage limitations associated with H2O2 and its reaction products can be eliminated.(43)

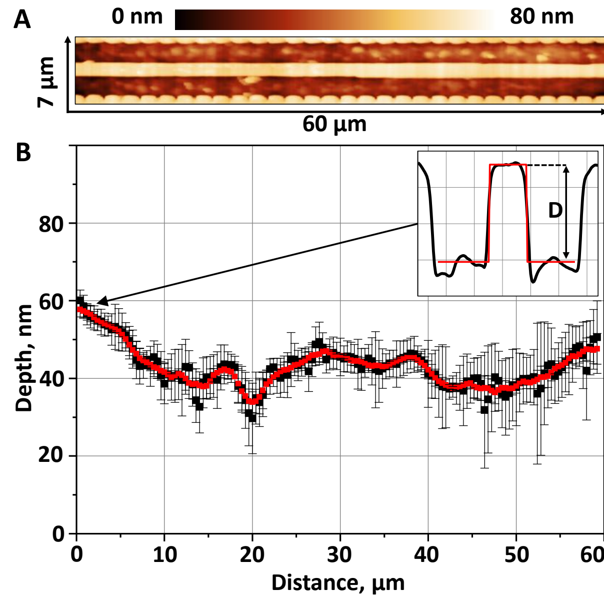

Figure 4. Depth analysis of imprinted waveguide with uniform depth showing (A) large area AFM scan of a single waveguide from the edge (left) to the center (right) of the SOI pillar, and (B) waveguide's depth profile (black squares) and 3 point moving average (red squares) with inset highlighting one of the waveguide's cross-section and depth measurement (label D). The bottom sub-20 nm roughness of the waveguide surroundings induced by the catalyst cannot be detected due to the low resolution of the large-area AFM scan shown in (A). Data represents depth extracted through fitting of step-height function with error bar representing fitting error.

In order to qualify the imprint results, the waveguide's cross-section depth profiles were extracted via AFM (Figure 4A) and analyzed. Its average depth was 42.9 ± 5.5 nm (Figure 4B) with a maximum of 60 nm at the edge and a minimum of 29.7 nm at approximately 20 µm from the edge. The maximum depth is closer to the edge of the pillar (Figure 4B) which could be explained by (a) the non-flatness of the stamp resulting from molding issues, (b) the proximity to the solution storage reservoir resulting in a faster etching, and (c) the bending of the stamp due to contact forces. A gradual reduction of the depth profile as a function of the distance from its edge (i.e., horizontal axis in Figure 4B)

is consistent with abovementioned scenarios “b” and “c”. However, given the random nature of the depth profile (Figure 4B), the stamp’s non-flatness (i.e., scenario “a”) is the most consistent explanation. In fact, stamps were prepared by UV NIL of spin-coated SU-8 resist with soft PDMS-based molds (as described in the Experimental Section) which is known to introduce pattern distortions during demolding operation such as rimming,(44–46) which is a protrusion of the pattern’s edges similar to the inverse of the silicon pattern observed in the inset of Figure 4B. Thus, the depth profile in Figure 4B is irregular since Mac-Imprint imprints the distorted geometry of the mold with high fidelity. This hypothesis was further confirmed in the additional experiment where AFM scans of imprinted SOI pillar and Mac-Imprint stamp were acquired at complimentary locations and are indeed mirror images of each other (See Figure S3 in the Supporting Information). Note that the large and low-resolution AFM scan in Figure 4A does not provide enough resolution (see details in the Experimental Section) to capture the porous gold morphology imprinted onto silicon.

2.2. Roughness reduction and its fundamental limits

Mac-Imprint introduces bottom and sidewall roughness which originates from its resolution limit (i.e., minimum discernible positive feature) being smaller than the pore diameter of the catalyst and results in the accurate transfer of the catalyst’s nanopores onto the imprinted surface.(23, 29) Thus, with the goal to address the roughness issue, it becomes necessary to find a theoretical basis to Mac-Imprint’s resolution limit. In 2011,

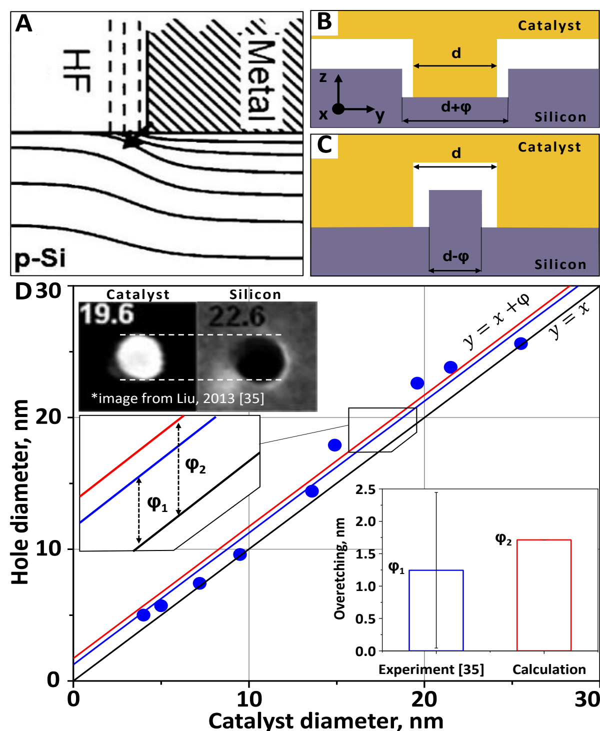

Figure 5. A – Theoretical model for band bending during anodic electrochemical machining of Si proposed by Sugita et al. Dashed lines at metal-solution interface represent isopotentials within the electrical double layer (Debye length) and solid lines represent isopotentials bending around the triple junction. Reprinted (adapted) with permission.[34] Copyright 2011 American Chemical Society. B and C – schematics of the overetching for the negative and positive Si features, respectively (not to scale). D – plot of silicon hole versus catalyst diameter using imported data from Liu et al.[35] Three lines with a unity slope are plotted with different offsets: zero (black - reference), best fit of experimental data (blue, ϕ_1) and two times the Debye length (red, ϕ_2). ϕ_1 on the bar plot is reported as average ± standard deviation based on 9 reported measurements. The upper inset contains top-down SEM images of the metal catalyst and the resulting hole in Silicon. The inset images and data are reprinted (adapted) with permission.[35] Copyright 2013 American Chemical Society.

Sugita et al.(34) first interpreted the band bending in silicon around the electrolyte-silicon-metal triple junction in the context of anodic electrochemical machining of silicon. Based

on the work of Nakato et al.(47), Sugita et al. proposed that the strong electric field developed in the electrical double layer at electrolyte-metal interface reduces the potential barrier in silicon near the electrolyte-silicon-metal junction (Figure 5A). This should lead to the migration of holes in silicon away from the triple junction to a distance proportional to the Debye length. If this theoretical basis is correct, it would result in silicon features being overetched by a lateral distance, φ, that is proportional to the Debye length (Figure 5B) which has not been experimentally verified in literature. While Sugita et al. worked with feature sizes ranging from 10-100 μm, recent experimental work on MACE by Liu et al. yielded sub-5nm features.(35) Using data from Liu et al.(35), it is possible to calculate the average overetched distance (i.e., φ1 in Figure 5D), which is the difference between catalyst diameter and silicon hole diameter and equals to 1.24 nm. This value closely matches two times the theoretical value of the Debye length (ϕ2 in Figure 5D) which is 1.71 nm (see calculations in Supporting Information). Note that the large standard deviation of φ1 (i.e., ±1.2 nm, details in the Supporting Table 2) could be attributed to (i) errors of the measurement technique associated with limited resolution or (ii) catalyst particle size distribution if catalyst and hole widths are not measured in complementary locations.(48)

Next, this work attempts to eliminate roughness by designing catalyst films whose pore sizes approach the Debye length to within at least an order of magnitude (Figure 5C). This was accomplished by using previously established process-structure relationship in the electroless dealloying of Au49Ag51 thin-films at far-from-equilibrium from literature

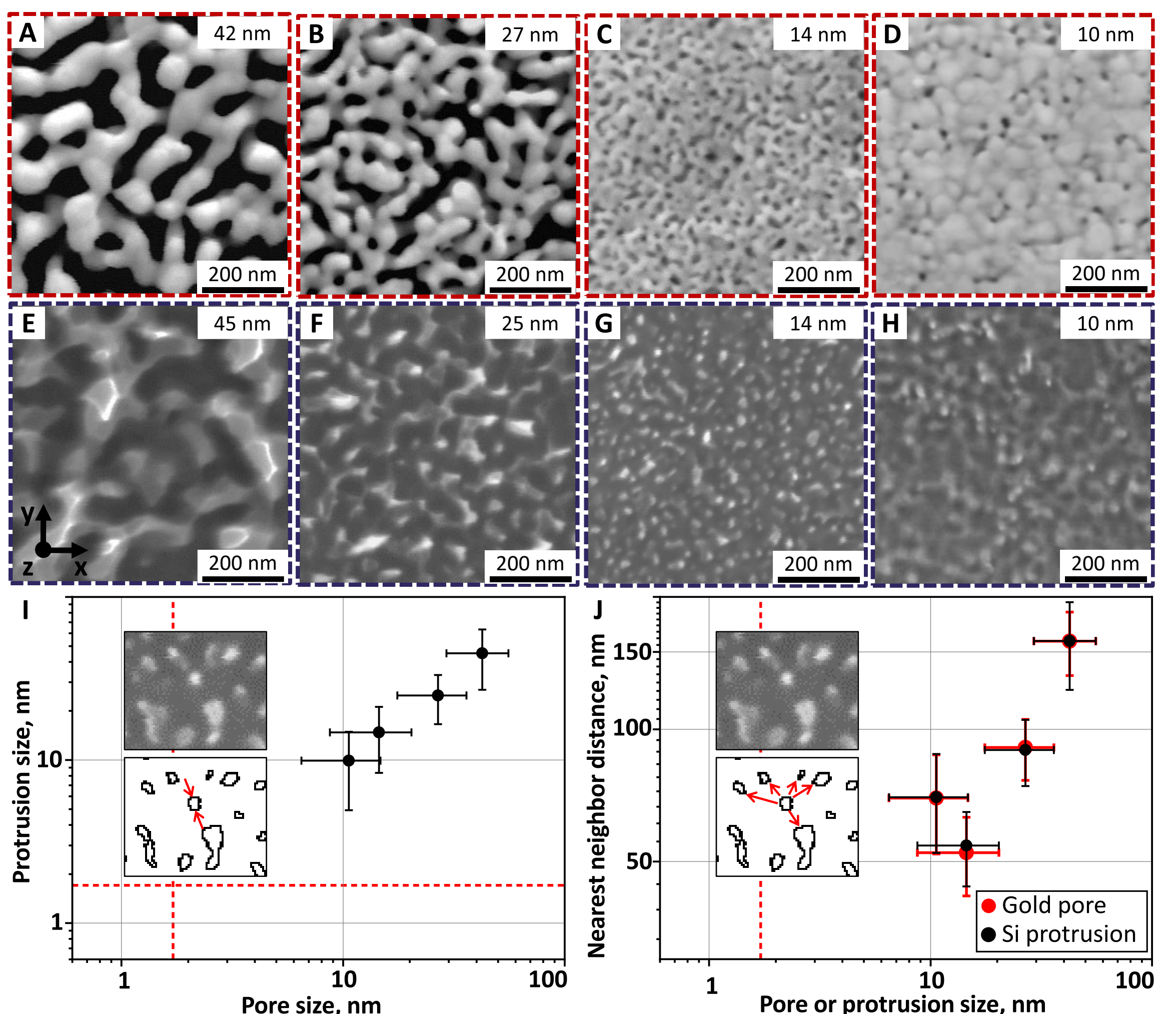

Figure 6. Top-down SEM images of the catalytic stamps with different average pore diameters (A-D) and imprinted waveguide surroundings (E-H). The boxes in the top right corner of the SEM images contain the average pore (A-D) and protrusion (E-H) diameters. Dependence of Si protrusion size on the catalyst pore size (I). Inset on I illustrate how the feature size (either pore or protrusion) was calculated. Dependence of nearest neighbor distance on the catalyst pore size and Si protrusion size (J, red and black, respectively). Inset on J illustrate how the nearest neighbor distance was calculated. Data is reported as average ± standard deviation. Red dashed lines on I and J indicate the resolution limit (i.e. double the Debye length).

which allows for ligament control between 25 and 64 nm.(33) By reproducing it and further reducing the dealloying time and temperature (for additional details, see Experimental

Section), catalyst films with average pore diameters of 42, 27, 14 and 10 nm were fabricated (Figure 6A-D) and used to Mac-Imprint arrays of linear rib waveguide structures (Figure 6E-H). Additionally, albeit pores on Figure 6C and D appear isolated, a developed porous network structure is still formed throughout the thickness of the catalytic films which was confirmed by high-magnification cross-sectional SEM images (Supporting Figure S4). The impact of the pore size of the catalyst on the surface roughening during Mac-Imprint was established through the SEM analysis of imprinted linear rib waveguide structures. Overall, the catalyst size downscaling to 10 nm reduced the Si protrusion size linearly (Figure 6I) from 45 nm (Figure 6E) to 10 nm (Figure 6H). In the latter case, it was observed that the grain boundary grooves of the catalyst are also transferred onto silicon which limits further reductions in its roughness.

In context to existing literature, Bastide et al.(29) and Sharstniou et al.(23) each attempted to reduce the catalyst pore size and roughness, but, at least in qualitative terms, their work did not reduce either the silicon protrusion size or roughness due to stamp defects (e.g., cracks, delaminated catalyst) transferred during imprinting and concomitant substrate porosification. In their works, the smallest distinguishable average Si protrusion size without indication of porosification was approximately 27 nm and 31 nm.(23, 29) Finally, according to the nearest neighbor analysis (for details, see Experimental Section) the average distance between nearest neighbor pores in the catalyst matches that of the Si protrusions (Figure 6J, red and black dots, respectively). Note that there is an increase of the nearest neighbor distance in the case of the smallest catalyst pore size (i.e., 10 nm)

which is attributed to incomplete Ag removal during dealloying which is known to produce lower pore surface area coverage and, thus, increases the interpore distances.(33)

Since the smallest pore size attained via electroless dealloying in this paper is still 5-6 times larger than the theoretical value for twice the Debye length, further reduction in the Si protrusion size is theoretically possible albeit the synthesis of catalysts with sub-10 nm average pore size becomes the limiting factor. In the literature of nanoporous gold synthesis through dealloying, the electroless and electrochemical dealloying methods have demonstrated the smallest pore size of approximately 5 nm by either reducing its temperature (e.g., -20 °C)(49) or inhibiting gold adatom surface diffusion.(50, 51) It was also shown that during dealloying ligament and pore size are inversely proportional to the melting temperature of host metal,(52) suggesting that higher melting temperature metal or alloys catalysts suitable for MACE, such as platinum, could be potential candidates to further reduce pore size into the sub-5 nm domain.(41, 53, 54) It should also be noted that, to promote smoothening of the nanoimprinted surfaces, the Debye layer thickness can be increased to approach the catalyst's pore size by (i) heating the etching solution and (ii) decreasing its ionic strength. The first approach would increase Debye layer thickness by ~1 Å given the low boiling point of the solution. The second approach can be achieved by reducing its concentration or by using solutes with a weaker dissociation constant both of which would reduce etch rates dramatically. These strategies should motivate future work to either eliminate the roughness or to improve the resolution limit of Mac-Imprint or MACE.

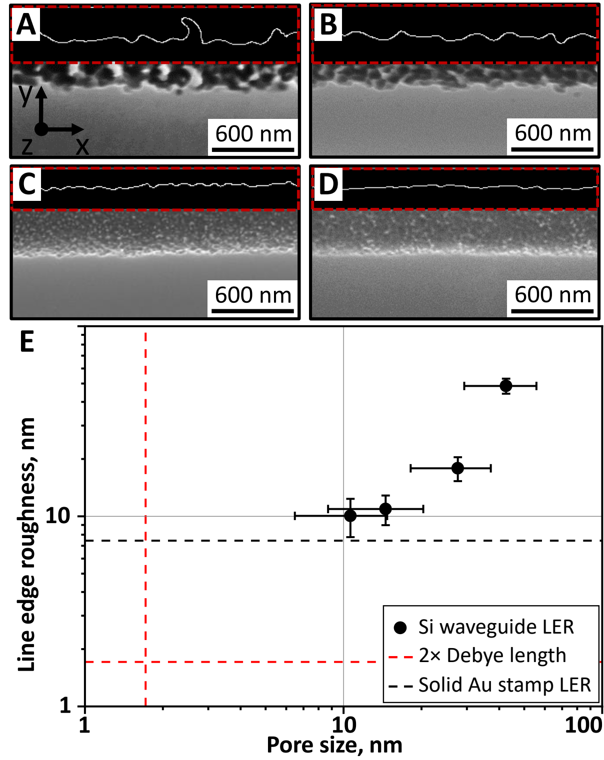

Figure 7. A-D – Top-down SEM images and edge profiles (framed with red dashed lines) of the waveguides, imprinted with porous catalysts with avarage pore sizes 42-10 nm respectively. E – Wavguide line edge roughness as a function of catalyst pores size. Data is reported as average ± standard deviation. Dashed lines indicate twice the Debye length (red) and solid Au stamp sidewall RMS (yellow).

Although the bottom roughness of the waveguide surroundings may interfere with the guided electromagnetic wave, most of the propagation losses occur due to light scattering on the sidewall roughness of the waveguide. In Mac-Imprint, it is generated by the tangential movement of the np-Au surface parallel to the vertical direction of the Si sidewalls as the etching progresses, leaving ‘scratch’ marks along it. Thus, in theory, the flatter and less rough the porous Au surface is, the smoother the sidewalls should become. To verify this hypothesis, the LER of the imprinted waveguides was measured at its top as a function of the pore size of the catalyst according to the procedure described in the

Experimental Section. Figure 7E shows that, with the reduction of the pore size of the catalyst from 42 nm to 10 nm, the LER non-linearly decreases from 48 nm (Figure 7A) to 10 nm (Figure 7D), which is comparable with values reported for plasma-based micromachined silicon waveguides without post-processing strategies for smoothening.(32, 55) The smallest LER in silicon features achievable by Mac-Imprint would be inherently limited by the LER of the stamp's pattern coated with solid gold which was measured to be ~7.5 nm (Figure 7E, yellow dashed line) and is attributed to the roughness of gold thin-film and imperfections from soft-lithography steps used to fabricate the stamp. Thus, the improvements in sidewall roughness tend to saturate for pore sizes approaching 7.5-10 nm (Figure 7E) limiting further improvements. It is worth noting that, at the magnification and the pixel size of the analyzed SEM images which are 30kx and 6.7 nm respectively, it might also limit measurement of further improvements at sub-10 nm pore sizes and require the use of alternate metrology techniques.

The minimization of LER to sub-10 nm is expected to have a positive impact on the minimum line-width resolution (MLWR) of Mac-Imprint. Albeit never experimentally determined, a reasonable criteria to estimate the minimum line-width resolution (MLWR) of a process is to use a 6-sigma approach based on sidewall LER (see Supporting Figure S5). According to this assumption, the reduction of the LER achieved with np-Au's pore size of 10 nm would translate to MLWR values of approximately 60 nm which is a significant improvement comparing to the state-of-the-art whose largest pore size of np-Au used was 42 nm.(23)

2.3. Nanoscopic Defect Analysis

It is important to mention that the reduction of the catalyst pore size through the far-from-equilibrium dealloying leads to the incomplete removal of silver that can negatively affect Mac-Imprint process. In particular, in contrast to gold, silver (i) induces changes to the energy band bending in silicon near catalyst/Si interface due its lower work function, which affects hole injection and transport in Si and induces its porosification,(53, 56) and (ii) is prone to dissolution and subsequent re-deposition.(57, 58) Despite catalysts with the smallest pore size being made with the shortest dealloying time, the large residual silver content of up to 42 at.% did not appear to induce porosification as evidenced by the SEM or optical microscopy. However, the porosification of Si could be happening in nanoscale form that would be challenging to detect using these techniques.

The analysis of the such defects during Mac-Imprint was accomplished by Raman spectroscopy, which has been extensively used in literature to characterize defects in silicon such as lattice strains,(59) microporosity (i.e., sub-2 nm) and mesoporosity (i.e., 2-50 nm),(60) and amorphous regions.(61) The imprinted waveguide, presented on Figure 8A and B, exhibited average peak position and full width at half-maximum (FWHM) of ~521.38 ± 0.07 cm-1 and ~4.20 ± 0.06 cm-1 respectively (Figure 8C and D) throughout the center section of the waveguide excluding 6 μm away from each edge. At each of the edges, a 0.09 cm-1 and 0.44 cm-1 shift to lower frequencies, and a 0.16 cm-1 and 0.08 cm-1 broadening of the Raman signal was observed (see locations i and xi in Figure 8E-F). These edge effects are attributed to the release of the residual stresses and strains in the Si device layer by the undercut (Figure 2A) of the buried oxide layer during Mac-Imprint, as

seen on Figure 8A and B near the edges of the SOI pillar. In fact, SOI processing is well known to introduce strains in the Si device layer which causes Raman peak to shift by ± 0.4 cm-1 from its mean position.(62) In our case, the blank SOI wafer had a peak position and FWHM of 521.47 ± 0.02 cm-1 and 4.15 ± 0.04 cm-1, respectively. With regards to it, the average peak position at the center of the waveguide shifts and broadens by approximately 0.2 cm-1 and 0.1 cm-1, respectively which is smaller than the expected values for microporous silicon (i.e., both approximately 1 cm-1 for crystallite sizes of < 5 nm)(60). Note that, in locations viii and xi in Figure 8 on the waveguide's narrowest section, there are geometrical defects originated from molding defects in the stamp that cannot be well understood. Overall, the center section has a constant peak position and width relative to the Raman signal from the original SOI wafer which adds further confirmation of the crystallinity quality of the imprinted waveguides. In future applications, these edge effects can be by-passed if necessary to avoid unnecessary scattering by patterning away from the edge or protecting the buried oxide layer during Mac-Imprint.

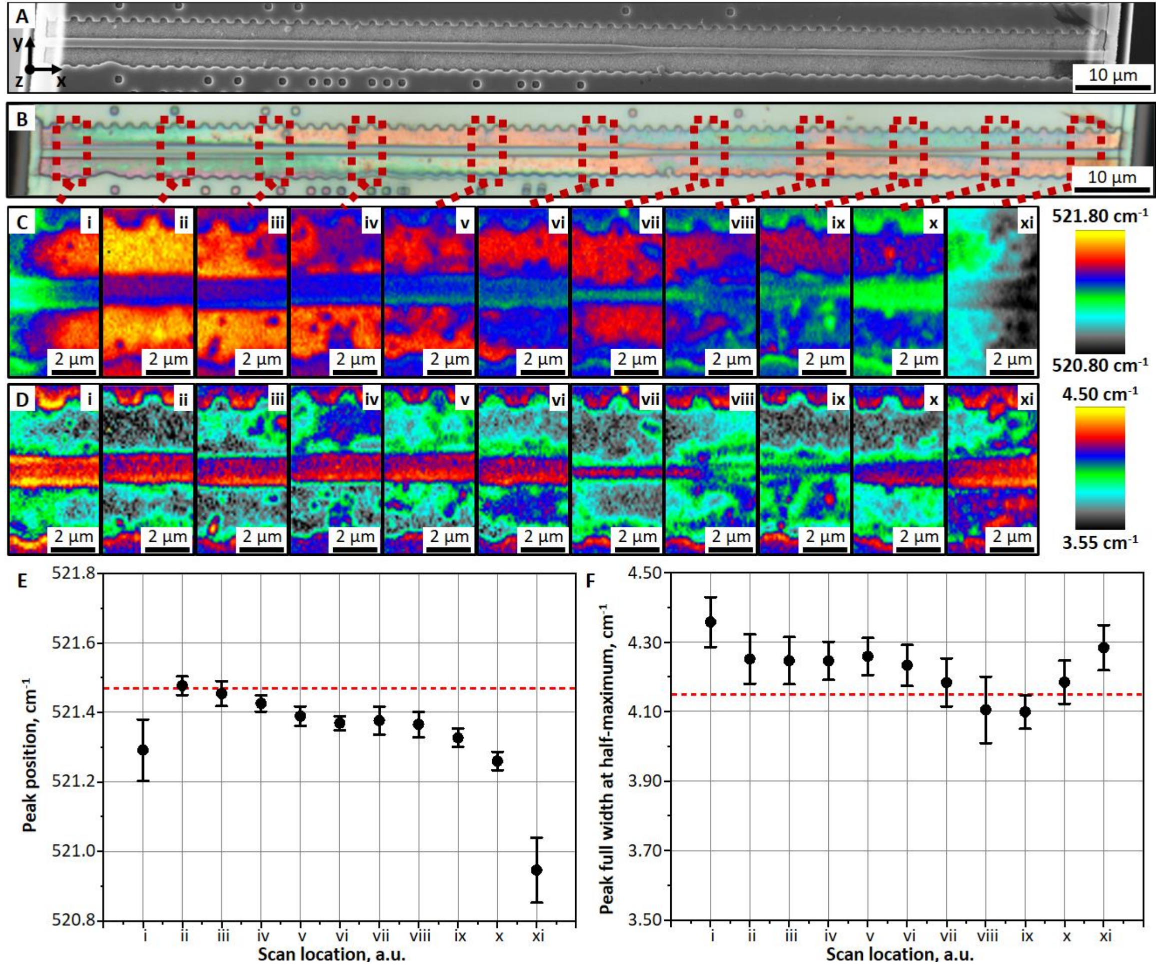

Figure 8. A and B – Top-down SEM and optical images of a single imprinted waveguide respectively. C and D – Maps of Raman signal peak position and full width at half-maximum respectively, taken at locations marked on B. E and F – Average values for Raman peak position and full width at half-maximum, respectively, of the waveguide at location marked on B. Data is reported as average ± standard deviation. Red dashed lines on E and F highlight the Raman peak position and full width at half maximum of the blank SOI wafer.

Lastly, optical waveguiding is demonstrated in a Mac-Imprinted silicon rib waveguide (Figure 9A). The top view IR imaging (Figure 9B) did not reveal a detectable scattering of the signal from the waveguide's walls, which suggests low scattering loss. The waveguide unfortunately was too short (L = 0.015 cm) to precisely measure its loss.

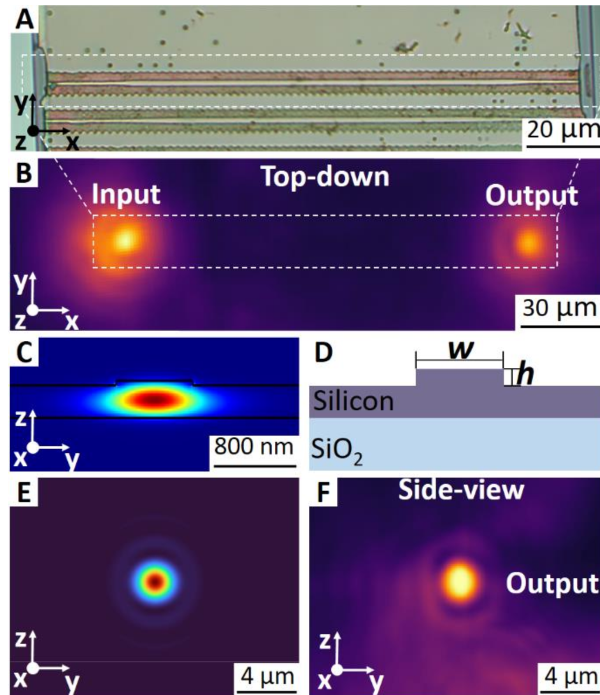

Figure 9. A – top-down optical image of the individual SOI pillar prior to waveguide testing. B – top-down infrared image of the individual SOI pillar during waveguide testing. Dashed lines on A and B highlight the tested waveguide. C – side-view of waveguide mode simulation. D – cross-sectional schematics of the waveguide, used for the simulation. E – side-view of simulated waveguide mode, corrected by PSF of 0.42NA objective. F – side-view infrared image of the output waveguide facet.

The waveguide mode simulation of the rib waveguide with nominal width, w = 750 nm, and imprint depth, h = 43 nm, (Figure 9D) is presented on Figure 9C and demonstrates the single mode and quasi-transverse-electric (TE) polarized nature of the waveguide. The convolution of the simulation with the point-spread-function (PSF) of the 0.42NA imaging objective is presented on Figure 9E and closely matches the output side-view image of the waveguide facet (Figure 9F). For more details on the convolution between simulated waveguide mode and PSF of the objective refer to the Supporting Figure S6. It has previously been shown that that single mode rib waveguides with similar dimensions can

exhibit favorable loss characteristics when compared to fully etched strip waveguides, owing to limited interaction between the waveguide mode and the waveguide surface.(63) Hence, optical propagation losses are expected to be a function of both the waveguide design and the surface roughness. The optical characterization demonstrated here importantly confirms that the Mac-Imprint process can be utilized to fabricate functional silicon photonic waveguides.

3. Conclusion

This paper reported the first extension of Mac-Imprint to SOI substrates and to geometries specific to requirements of silicon rib waveguides. It was established that the mass-transport of the reactants in the perpendicular direction of the waveguide's longitudinal axis is the limiting factor for attaining imprinting of uniform patterns without porosity. This mass transport could not be supported by solid catalysts. In contrast, a nanoporous catalyst provided necessary diffusional pathways which allowed for fabrication of Si waveguides with an average depth of 42.9 nm ± 5.5 nm. This depth variation was attributed to the stamp distortions during demolding of the stamp during its fabrication which can be improved using commercial nanoimprinting tooling. The bottom and sidewall roughness induced by Mac-Imprint was controlled by reducing the pore sizes to within an order of magnitude of the Debye Length (i.e., the resolution limit of the Mac-Imprint). In particular, 10 nm pore size catalyst resulted in a 10 nm bottom and sidewall roughness of the Si rib waveguide which is comparable to similar structures which are

made by conventional plasma etching methods. The limited levels of Si defect formation during Mac-Imprint were achieved by the use of the etching solution with high ρ parameter of 99.5% and were confirmed by Raman analysis of the imprinted waveguide, which revealed a uniform peak position and FWHM thought the middle portion of the waveguide excluding edges. Fabricated waveguides support single-mode light propagation which was measured by the side-view IR imaging and closely matches electromagnetic simulations. Additionally, top-down IR imaging does not reveal detectable light scattering from the waveguide walls. Overall, this paper represents a significant step towards commercial implementation of the Mac-Imprint for the fabrication of functional 3D freeform optoelectronic devices, such as advanced waveguides,(8–12) surface plasmon structures,(13) and chromatic-aberration corrected lenses.(14) Moreover, Mac-Imprint's unique ability to tailor its nanoscale roughness could be advantageous in fabrication of quasicrystal interferometers with physical unclonable functions which are essential for hardware and information security.(15) In the future, improvements to the stamp design aimed at embedding the etching solution storage reservoir in it instead of in the substrate are necessary for scaling the technique to blank SOI wafers. The work on determining the maximum EEPD supported by the thin-film catalyst in this paper should inform the reasonable pitch that should exist between the embedded reservoirs in such proposed stamp designs. This approach will also allow for free optimization of Mac-Imprint parameters as the undercut of the BOX layer of the SOI pillar will be eliminated entirely. The authors also see potential scaling of Mac-Imprint in its integration with commercial mask aligners and nanoimprinting technologies presently used for polymer patterning by (i) adding liquid

handling capabilities, (ii) using less hazardous chemicals to simplify equipment design and (iii) investigating demolding strategies particularly for high-aspect ratio patterns.

4. Experimental Section

Substrate preparation: Mac-Imprint was performed on SOI wafers with 340 nm thick, p-type boron-doped device layer which has resistivity of 14 – 22 Ω·cm and (100) crystal orientation. Prior to Mac-Imprint, arrays of 270 µm tall and 150 µm wide pillars spaced by 900 µm were fabricated on the SOI wafers by photolithography and deep-reactive ion etching in order to provide etching solution storage volume. The articulation on the necessity of SOI wafer pre-patterning and guidelines for the design of pillar size can be found in Supporting Information. Pre-patterned SOI wafers were thoroughly rinsed with acetone, isopropyl alcohol and deionized (DI) water followed by RCA-1 cleaning and another DI water rinsing before Mac-Imprint.

Stamp preparation: The fabrication of Mac-Imprint stamps consisted of four steps which are described below and detailed protocol of those can be found elsewhere.(64)

4.1. PDMS replica molding: At first, waveguide pattern was created on a Si master mold using e-beam lithography followed by reactive ion etching. Next, the pattern of the Si master mold was replicated onto PDMS according to the standard replica molding procedure.(65)

4.2. Soft nanoimprint lithography: After that, PDMS replica mold was used to pattern photoresist by means of nanoimprint lithography. To do so, 2.5 x 2.5 cm2 Si chips were firstly cleaned by RCA-1 solution followed by DI water rinsing. Next, clean Si chips were spin coated with 20 µm thick HF-resistant SU-8 2015 photoresist layer. Immediately after spin coating, the PDMS replica mold was placed on top of the photoresist layer with pattern facing down and pressed with the UV transparent glass slab, yielding 15 g/cm2 of pressure. The UV curing was performed under 6 W UV bulb placed at 10 cm distance from the SU-8 surface for 2 hours.

4.3. Catalytic metal sputtering: Upon UV curing, Si chips with patterned SU-8 layer were placed inside NSC-3000 magnetron sputter chamber at 20 cm distance from the sputtering targets. For the Mac-Imprint with solid catalyst, two layers of metal were deposited onto the stamp in the following order: 20 nm Cr (adhesion) and 80 nm Au (catalyst). For the Mac-Imprint with porous catalyst, three layers of metal were deposited onto the stamp in the following order: 20 nm Cr (adhesion), 50 nm Au (intermediate) and 375 nm Ag/Au alloy (precursor for porous catalyst).

4.4. Porosification of catalyst: In order to create nanoporous catalysts, stamps with 375 nm Ag/Au alloy (51 at.% of Ag) were subjected to selective dissolution of Ag by means of dealloying in far from equilibrium conditions. The dealloying was performed in aqueous solution of nitric acid (H2O:HNO3 = 1:1 by vol.) at a constant stirring rate of 100 rotations per minute following the protocol established in the work of Niauzorau et al.(33) The pore size of the catalyst was controlled by varying dealloying time and solution temperature. In particular, the np-Au with average pore sizes of 10 and 14 nm was produced

at room temperature solution within 10 and 30 min, respectively, while the 27 nm average pore sizes were obtained at 65 °C temperature solution within 10 min. After the dealloying, a subset of porous catalytic stamps with average pore sizes of 27 nm was annealed in Ar environment at 250 °C for 1 hour in order to increase average pore size to 42 nm through thermal coarsening.

Mac-Imprint setup and conditions: The Mac-Imprint set-up is composed of an electrochemical cell, a Teflon rod acting as a stamp holder, a load cell, and a vertical stage (See Supporting Figure S7). The leveling between stamp and substrate is achieved during the assembly of the stamp to its holder. The stamp is placed on top of the substrate with its gold-coated side facing down and its back is attached to the stamp holder using a photocurable resin placed between them. The stamp and its holder are UV-cured using omnidirectional illumination (See Supporting Figure S7B) ensuring that the stamp and substrate are parallel and aligned after assembly. After curing, the stamp can be retracted by the automated stage without loss of alignment. The SOI substrate is placed inside the electrochemical cell, which is then filled with the etching solution. The vertical stage brings a stamp holder with mounted stamp in plate-to-plate contact with SOI substrate. The contact force of 22.24 N is developed within 0.1 sec and maintained within ±5% of the set-point for 10 ± 0.1 s. This allows Mac-Imprint of the waveguide patterns to be reproducible provided the stamp-to-substrate alignment remains unaltered. After the imprinting, the stamp is retracted into home position and etching solution is aspirated from electrochemical cell. Further, SOI substrate is immediately flushed with excess amount of isopropyl alcohol

to terminate the undercut of buried oxide layer. The total time of SOI substrate exposure to the etching solution is 70 sec. Detailed description of Mac-Imprint setup and protocol can be found elsewhere.(64) It should be noted that ±5 sec variation in the Mac-Imprint total processing time (i.e., ~ 70 s) does not significantly affect the buried layer undercut depth (See Supporting Figure S8).

The etching solution with ρ equal to 99.5 % is prepared by mixing HF (48 % by vol.) and H2O2 (30 % by vol.) in the 68:1 ratio (HF:H2O2; by vol.). Moreover, pure ethanol is added to the etching solution (4 % of the etching solution volume) in order to improve solution's wettability. A fresh etching solution was mixed prior every Mac-Imprint operation. All chemicals were ACS grade, purchased from Sigma Aldrich.

Morphological, structural, and functional characterization:Morphological properties of the Mac-Imprint stamps and imprinted waveguides were characterized by scanning electron microscopy (SEM) using Philips XL-30 FEG SEM. All SEM images were acquired at 10 kV accelerating voltage and 130 pA beam current.

Imprint depth profiles were characterized by atomic force microscopy (AFM) using the Witec Alpha 300 RA+ system. AFM scans were acquired in tapping mode using NHCV-A Bruker probes with tip radius of 8 nm, spring constant of 40 N/m and resonant frequency of 320 kHz. For AFM image acquired in Figure 4, the lateral resolution is determined by sampling distance which is set to be 234 nm and 39 nm in the x- and y-directions, respectively. The resolution of its height is set by the AFM instrumentation which, as per the vendor, it is 0.5 nm.

The nanoscale defects of the imprinted waveguides and surroundings were characterized by confocal Raman microscopy using the same Witec system. The Raman signal was excited by 532 nm laser with the 0.1 mW output power. Raman signal was acquired using 1800 g/mm grating yielding 1 cm-1 spectral resolution with the accumulation time of 0.2 sec. Individual Raman mapping was performed over 4 x 9 µm2 area with total amount of 40x90 data points.

The performance of the waveguide was characterized using near-IR (O-band) light from a tunable laser (Santec TSL-550), which was coupled onto the chip using through a polarization controller and tapered lensed fiber (OZ optics) and aligned using XYZ piezo controlled alignment stage (Thorlabs NanoMax). Fiber-to-chip alignment and successful waveguiding was verified by IR imaging both the top surface and output side-view of the chip with infrared cameras (Hamamatsu C2741). Waveguide mode simulation of the nanoimprinted silicon waveguide cross-section were performed at the wavelength 1310 nm using the finite difference eigenmode method (Ansys Lumerical MODE). The waveguide cross-sectional facet view IR imaging was modelled by convoluting the waveguide mode profile with the point spread function (PSF) of the NA = 0.42 imaging objective.

SEM image analysis: The quantification of (i) np-Au average pore size, (ii) bottom roughness and (iii) LER of the imprinted Si rib waveguides was performed through the analysis of the top-down SEM images using AQUAMI,(66) and ImageJ software (i.e., i and ii, more details in the Supporting Information, Figure S9 and Figure S10) as well as specifically written Python algorithm (i.e., iii, more details in the Supporting Figure S11).

Note that in this paper bottom roughness of the imprinted waveguides was quantified using average sizes of Si protrusions. The distance between closest particles (either pores or protrusions in np-Au and imprinted Si, respectively) was called "nearest neighbor distance" and its analysis was performed using ImageJ software according to the algorithm published elsewhere (more details in the Supporting Figure S12).(67)

Statistical Analysis: Analysis of AFM data was performed using Gwyddion software. Prior extracting imprint depth, the AFM data was leveled with respect to the non-imprinted top surface using "Mean Plane Subtraction" function. The individual imprint depth (Figure 4B, inset) was found from "Step-height" fitting function of "Critical dimension" module with error bar representing fitting error. The average imprint depth and it's standard deviation (SD) was calculated based on 148 measurements along the AFM scan.

In the analysis of work by Liu et al. the average overetched distance and it's SD was calculated based on 9 reported measurements.

The analysis of the average size of np-Au pores, Si protrusions and nearest neighbor distance was performed using AQUAMI and ImageJ software without any pre-processing of SEM images. The magnification was kept constant throughout the SEM images to maintain the same pixel size. Sample size for each measurement in this case was different and dependent on the amount of pores/protrusions present on the SEM image. Note that for a given sample the nearest neighbor distance for individual particle is found as an average distance to five nearest neighbors. The nearest neighbor distance of the sample is

then calculated as average of all individual nearest neighbor distances. Data was presented as average ± SD.

The analysis of the LER was performed by calculating the RMS of the waveguide's line edge profile obtained from high-magnification SEM images. The magnification was kept constant throughout the SEM images to maintain the same pixel size. Prior importing SEM images to the Python code, the bottom surface on the SEM images was thresholded and images were converted into .txt format using ImageJ. Waveguide line edge profiles were obtained on 2-µm long waveguide segments using Canny edge detection algorithm with Gaussian filter size sigma equal to 2.6. The LER of individual line edge profile was calculated as an RMS of the pixel values multiplied by pixel size. The LER of the sample is then calculated as average of 4 independent measurements of different waveguide segments. Data were presented as average ± standard deviation (SD).

The analysis of the Raman data was performed using Project FIVE software. Prior extracting Raman signal position and full width at half-maximum, the signal was fitted using Lorentz function. The average peak position, full width at half-maximum and it's SD was calculated using data from the waveguide region only (i.e., excluding waveguide surroundings).

Supporting Information

Supporting Information is available from the Wiley Online Library or from the author.

Acknowledgements

We acknowledge the help of PhD candidate Trumann Walker (Arizona State University) with writing Python algorithm for sidewall roughness analysis; the use of facilities within the Eyring Materials Center at Arizona State University; Honeywell International for providing master molds and financial support; the Science Foundation Arizona under the Bisgrove Scholars Award and the NSF CMMI Grants No. 1944750 and No. 1932899.

Author Contribution

N.K., J.D.R., M.P. and B.A. conceived research. A.S., M.P., N.K. and B.A. designed research. A.S., S.N. and B.A. performed research. A.L.H and J.D.R. tested optical waveguiding. A.S. and B.A. wrote the manuscript. All the authors discussed the results and commented on the manuscript.

Conflict of Interests

The authors declare no conflict of interests.

References

[1] L. Chrostowski, M. Hochberg, Silicon Photonics Design: From Device to System, Cambridge University Press, 2015.

[2] W. Bogaerts, R. Baets, P. Dumon, V. Wiaux, S. Beckx, D. Taillaert, B. Luyssaert, J. Van Campenhout, P. Bienstman, D. Van Thourhout, J. Light. Technol. 2005, 23, 401.

[3] D. Taillaert, F. Van Laere, M. Ayre, W. Bogaerts, D. Van Thourhout, P. Bienstman, R. Baets, Japanese J. Appl. Physics, Part 1 Regul. Pap. Short Notes Rev. Pap. 2006, 45, 6071.

[4] Y. Tang, Z. Wang, L. Wosinski, U. Westergren, S. He, Opt. Lett. 2010, 35, 1290.

[5] D. Benedikovic, C. Alonso-Ramos, P. Cheben, J. H. Schmid, S. Wang, D.-X. Xu, J. Lapointe, S. Janz, R. Halir, A. Ortega-Moñux, J. G. Wangüemert-Pérez, I. Molina-Fernández, J.-M. Fédéli, L. Vivien, M. Dado, Opt. Lett. 2015, 40, 4190.

[6] C. Li, H. Zhang, M. Yu, G. Q. Lo, Opt. Express 2013, 21, 7868.

[7] R. Takei, M. Suzuki, E. Omoda, S. Manako, T. Kamei, M. Mori, Y. Sakakibara, Appl. Phys. Lett. 2013, 102, DOI 10.1063/1.4795308.

[8] L. H. Gabrielli, D. Liu, S. G. Johnson, M. Lipson, Nat. Commun. 2012, 3, DOI 10.1038/ncomms2232.

[9] J. Garnett, J. Valentine, Opt. InfoBase Conf. Pap. 2012, 4.

[10] A. Xie, L. Zhou, J. Chen, X. Li, Opt. Express 2015, 23, 3960.

[11] N. Sakib, J. D. Ryckman, Opt. Lett. 2020, 45, 4730.

[12] F. Bin Tarik, J. D. Ryckman, Opt. Contin. 2022, 1, 453.

[13] N. Yu, Q. J. Wang, M. A. Kats, J. A. Fan, S. P. Khanna, L. Li, A. G. Davies, E. H. Linfield, F. Capasso, Nat. Mater. 2010, 9, 730.

[14] P. Wang, N. Mohammad, R. Menon, Sci. Rep. 2016, 6, 1.

[15] F. Bin Tarik, A. Famili, Y. Lao, J. D. Ryckman, Nanophotonics 2020, 9, 2817.

[16] R. A. Gottscho, J. Vac. Sci. Technol. B Microelectron. Nanom. Struct. 1992, 10, 2133.

[17] J. Yeom, Y. Wu, J. C. Selby, M. A. Shannon, J. Vac. Sci. Technol. B Microelectron. Nanom. Struct. 2005, 23, 2319.

[18] S. Y. Chou, C. Keimel, J. Gu, Nature 2002, 417, 835.

[19] J. D. Ryckman, M. Liscidini, J. E. Sipe, S. M. Weiss, Opt. InfoBase Conf. Pap. 2011, 1857.

[20] J. Zhang, L. Zhang, L. Han, Z. W. Tian, Z. Q. Tian, D. Zhan, Nanoscale 2017, 9, 7476.

[21] E. Torralba, M. Halbwax, T. El, M. Fouchier, V. Magnin, J. Harari, J. Vilcot, S. Le, R. Lachaume, C. Cachet-vivier, S. Bastide, Electrochem. commun. 2017, 76, 79.

[22] B. P. Azeredo, Y. Lin, A. Avagyan, M. Sivaguru, K. Hsu, Adv. Funct. Mater. 2016, 26, 2929.

[23] A. Sharstniou, S. Niauzorau, P. M. Ferreira, B. P. Azeredo, PNAS 2019, 116, 10264.

[24] X. Li, P. W. Bohn, Appl. Phys. Lett. 2000, 77, 2572.

[25] C. Chartier, S. Bastide, C. Lévy-Clément, Electrochim. Acta 2008, 53, 5509.

[26] Z. Huang, N. Geyer, P. Werner, J. De Boor, U. Gösele, Adv. Mater. 2011, 23, 285.

[27] O. J. Hildreth, W. Lin, C. P. Wong, ACS Nano 2009, 3, 4033.

[28] K. Rykaczewski, O. J. Hildreth, C. P. Wong, A. G. Fedorov, J. H. J. Scott, Nano Lett. 2011, 11, 2369.

[29] S. Bastide, E. Torralba, M. Halbwax, S. Le Gall, E. Mpogui, C. Cachet-Vivier, V. Magnin, J. Harari, D. Yarekha, J.-P. Vilcot, Front. Chem. 2019, 7, 1.

[30] N. Geyer, B. Fuhrmann, Z. Huang, J. De Boor, H. S. Leipner, P. Werner, J. Phys. Chem. C 2012, 116, 13446.

[31] K. K. Lee, D. R. Lim, H. C. Luan, A. Agarwal, J. Foresi, L. C. Kimerling, Appl. Phys. Lett. 2000, 77, 2258.

[32] K. K. Lee, D. R. Lim, L. C. Kimerling, J. Shin, F. Cerrina, Opt. Lett. 2001, 26, 1888.

[33] S. Niauzorau, A. Sharstniou, V. K. Sampath, N. Kublik, H. Bandarenka, B. Azeredo, 2022, 17927.

[34] T. Sugita, C. L. Lee, S. Ikeda, M. Matsumura, ACS Appl. Mater. Interfaces 2011, 3, 2417.

[35] G. Liu, K. L. Young, X. Liao, M. L. Personick, C. A. Mirkin, J. Am. Chem. Soc. 2013, 135, 12196.

[36] N. Van Toan, N. Inomata, M. Toda, T. Ono, Nanotechnology 2018, 29, DOI 10.1088/1361-6528/aab1d3.

[37] H. L. Weissberg, J. Appl. Phys. 1963, 34, 2636.

[38] M. Liang, C. Fu, B. Xiao, L. Luo, Z. Wang, Int. J. Heat Mass Transf. 2019, 137, 365.

[39] K. Kim, B. Ki, K. Choi, S. Lee, J. Oh, ACS Appl. Mater. Interfaces 2019, 11, 13574.

[40] L. Li, Y. Liu, X. Zhao, Z. Lin, C. Wong, ACS Appl. Mater. Interfaces 2014, 6, 575.

[41] L. Romano, M. Kagias, J. Vila-Comamala, K. Jefimovs, L. T. Tseng, V. A. Guzenko, M. Stampanoni, Nanoscale Horizons 2020, 5, 869.

[42] H. Li, J. Niu, G. Wang, E. Wang, C. Xie, ACS Appl. Electron. Mater. 2019, 1, 1070.

[43] H. Xu, L. Han, J. J. Su, Z. Q. Tian, D. Zhan, Sci. China Chem. 2022, 65, 810.

[44] W. Jiang, Y. Ding, H. Liu, B. Lu, Y. Shi, J. Shao, L. Yin, Microelectron. Eng. 2008, 85, 458.

[45] H. Schift, J. Vac. Sci. Technol. B Microelectron. Nanom. Struct. 2008, 26, 458.

[46] M. Li, Y. Chen, W. Luo, X. Cheng, Micromachines 2021, 12, DOI 10.3390/mi12040349.

[47] Y. Nakato, K. Ueda, H. Yano, H. Tsubomura, J. Phys. Chem. 1988, 92, 2316.

[48] J. Chai, F. Huo, Z. Zheng, L. R. Giam, W. Shim, C. A. Mirkin, Proc. Natl. Acad. Sci. U. S. A. 2010, 107, 20202.

[49] L. H. Qian, M. W. Chen, Appl. Phys. Lett. 2007, 91, DOI 10.1063/1.2773757.

[50] J. Snyder, P. Asanithi, A. B. Dalton, J. Erlebacher, Adv. Mater. 2008, 20, 4883.

[51] J. Snyder, K. Livi, J. Erlebacher, J. Electrochem. Soc. 2008, 155, C464.

[52] Q. Chen, K. Sieradzki, Nat. Mater. 2013, 12, 1102.

[53] K. W. Kolasinski, Nanoscale Res. Lett. 2014, 9, 1.

[54] E. Torralba, S. Le Gall, R. Lachaume, V. Magnin, J. Harari, M. Halbwax, J. P. Vilcot, C. Cachet-Vivier, S. Bastide, ACS Appl. Mater. Interfaces 2016, 8, 31375.

[55] H. Shang, D. Sun, P. Yu, B. Wang, T. Yu, T. Li, H. Jiang, Coatings 2020, 10, 236.

[56] E. Pinna, S. Le Gall, E. Torralba, G. Mula, C. Cachet-Vivier, S. Bastide, Front. Chem. 2020, 8, 1.

[57] N. Geyer, B. Fuhrmann, H. S. Leipner, P. Werner, ACS Appl. Mater. Interfaces 2013, 5, 4302.

[58] M. O. Williams, D. Hiller, T. Bergfeldt, M. Zacharias, J. Phys. Chem. C 2017, 121, 9296.

[59] E. Anastassakis, A. Pinczuk, E. Burstein, F. H. Pollak, M. Cardona, Solid State Commun. 1993, 88, 1053.

[60] H. Münder, C. Andrzejak, M. G. Berger, U. Klemradt, H. Lüth, R. Herino, M. Ligeon, Thin Solid Films 1992, 221, 27.

[61] J. E. Smith, M. H. Brodsky, B. L. Crowder, M. I. Nathan, A. Pinczuk, Phys. Rev. Lett. 1971, 26, 642.

[62] T. Iida, T. Itoh, D. Noguchi, Y. Takanashi, Y. Takano, Y. Kanda, J. Appl. Phys. 2001, 89, 2109.

[63] M. A. Tran, D. Huang, T. Komljenovic, J. Peters, A. Malik, J. E. Bowers, Appl. Sci. 2018, 8, DOI 10.3390/app8071139.

[64] A. Sharstniou, S. Niauzorau, A. Junghare, B. P. Azeredo, JoVE 2022, e61040.

[65] D. Qin, Y. Xia, G. M. Whitesides, Nat. Protoc. 2010, 5, 491.

[66] J. Stuckner, K. Frei, I. McCue, M. J. Demkowicz, M. Murayama, Comput. Mater. Sci. 2017, 139, 320.

[67] M. Haeri, M. Haeri, J. Open Res. Softw. 2015, 3, 2.

APPENDIX E

RIGHTS AND PERMISSIONS FOR PREVIOUSLY PUBLISHED ARTICLE ENTITLED "ROUGHNESS SUPPRESSION IN ELECTROCHEMICAL NANOIMPRINTING OF SI FOR APPLICATIONS IN SILICON PHOTONICS"

PERMISSION FROM PUBLISHER

11/10/22, 10:17 AM RightsLink Printable License

JOHN WILEY AND SONS LICENSE
TERMS AND CONDITIONS

Nov 10, 2022

This Agreement between Arizona State University ("You") and John Wiley and Sons ("John Wiley and Sons") consists of your license details and the terms and conditions provided by John Wiley and Sons and Copyright Clearance Center.

License Number	5425451429679
License date	Nov 10, 2022
Licensed Content Publisher	John Wiley and Sons
Licensed Content Publication	Advanced Materials
Licensed Content Title	Roughness Suppression in Electrochemical Nanoimprinting of Si for Applications in Silicon Photonics
Licensed Content Author	Aliaksandr Sharstniou, Stanislau Niauzorau, Anna L. Hardison, et al
Licensed Content Date	Sep 27, 2022
Licensed Content Volume	34
Licensed Content Issue	43
Licensed Content Pages	12

11/10/22, 10:17 AM RightsLink Printable License

Type of use	Dissertation/Thesis
Requestor type	Author of this Wiley article
Format	Electronic
Portion	Full article
Will you be translating?	No
Title	Metal-Assisted Electrochemical Nanoimprinting: Delivering Resolution and Throughput via Engineered Stamps
Institution name	Arizona State University
Expected presentation date	Nov 2022
Order reference number	23
Requestor Location	Arizona State University 6075 S. Innovation Way West MESA, AZ 85212 United States Attn: Arizona State University
Publisher Tax ID	EU826007151
Total	0.00 USD

Terms and Conditions

PERMISSIONS FROM CO-AUTHORS

Stanislau Niauzorau <sniauzor@asu.edu> Fri, Nov 18, 2022 at 9:45 AM
To: "Aliaksandr.Sharstniou@asu.edu" <Aliaksandr.Sharstniou@asu.edu>, Bruno Azeredo <Bruno.Azeredo@asu.edu>
Cc: Judson Douglas Ryckman <jryckma@clemson.edu>, "Neil A. Krueger" <nkruege2@gmail.com>, "Puckett, Matthew" <Matthew.Puckett@honeywell.com>, Anna Hardison <hardis3@g.clemson.edu>

Yes, you have my permission.

Anna Hardison <hardis3@g.clemson.edu> Fri, Nov 18, 2022 at 10:27 AM
To: Aliaksandr.Sharstniou@asu.edu
Cc: Bruno Azeredo <Bruno.Azeredo@asu.edu>, Stanislau Niauzorau <sniauzor@asu.edu>, Judson Douglas Ryckman <jryckma@clemson.edu>, "Neil A. Krueger" <nkruege2@gmail.com>, "Puckett, Matthew" <Matthew.Puckett@honeywell.com>

Hi Aliexsandr,
You have my permission. Congratulations on your dissertation!

Judson Douglas Ryckman <jryckma@clemson.edu> Fri, Nov 18, 2022 at 10:43 AM
To: Anna Hardison <hardis3@g.clemson.edu>, "Aliaksandr.Sharstniou@asu.edu" <Aliaksandr.Sharstniou@asu.edu>
Cc: Bruno Azeredo <Bruno.Azeredo@asu.edu>, Stanislau Niauzorau <sniauzor@asu.edu>, "Neil A. Krueger" <nkruege2@gmail.com>, "Puckett, Matthew" <Matthew.Puckett@honeywell.com>

Yes please do!

Neil Krueger <nkruege2@gmail.com> Fri, Nov 18, 2022 at 11:20 AM
To: Judson Douglas Ryckman <jryckma@clemson.edu>
Cc: Anna Hardison <hardis3@g.clemson.edu>, Aliaksandr.Sharstniou@asu.edu, Bruno Azeredo <Bruno.Azeredo@asu.edu>, Stanislau Niauzorau <sniauzor@asu.edu>, "Puckett, Matthew" <Matthew.Puckett@honeywell.com>

Absolutely, please use it!

Puckett, Matthew <Matthew.Puckett@honeywell.com> Fri, Nov 18, 2022 at 11:59 AM
To: Neil Krueger <nkruege2@gmail.com>, Judson Douglas Ryckman <jryckma@clemson.edu>
Cc: Anna Hardison <hardis3@g.clemson.edu>, "Aliaksandr.Sharstniou@asu.edu" <Aliaksandr.Sharstniou@asu.edu>, Bruno Azeredo <Bruno.Azeredo@asu.edu>, Stanislau Niauzorau <sniauzor@asu.edu>

You have my permission as well.

Bruno Azeredo <Bruno.Azeredo@asu.edu> Fri, Nov 18, 2022 at 12:58 PM
To: "Aliaksandr Sharstniou (Student)" <Aliaksandr.Sharstniou@asu.edu>

I approve